Constraints to UHE cosmic ray source scenarios with all the major observables of the Pierre Auger Observatory

Dissertation

zur Erlangung des Doktorgrades
der Naturwissenschaften (Dr. rer. nat.)

BERGISCHE UNIVERSITÄT WUPPERTAL

Fachbereich C - Mathematik und Naturwissenschaften
der Fachgruppe Physik vorgelegt von

Biswajit Sarkar
aus
Wuppertal

September 2015

Die Dissertation kann wie folgt zitiert werden:

urn:nbn:de:hbz:468-20160503-105034-2-2
[http://nbn-resolving.de/urn/resolver.pl?urn=urn%3Anbn%3Ade%3Ahbz%3A468-20160503-105034-2]

1. Gutachter
Prof. Dr Kar-Heinz Kampert
Bergische Universität Wuppertal

2. Gutachter
Prof. Dr. Günther Sigl
Universität Hamburg

Contents

1 Introduction

Unveiling the mystery of the sources of ultra high energetic cosmic rays (UHECR) that possess energies above 10^{18} eV is one of the most urgent questions in contemporary astroparticle physics. Up to now no final identification of the sources is achieved even after more than one century of research has passed since Victor Hess discovered cosmic rays in the year 1912 [1]. In this field of science which covers a vast energy range already first clues of sources can be made for low energies but at the highest energetic end the current status is not conclusive.

In this thesis predictions for UHECR observables are made and a comparison with the data mainly from the Pierre Auger Observatory is carried out to constrain the properties of source candidates in this energy range. A number of different observables that measure a variety of properties of cosmic rays as the energy spectrum, the mass composition, the direction and the existence of UHE photons and neutrinos are used to ensure a holistic view on UHECR. The theoretical predictions of these observables from astrophysical scenarios including assumptions on sources and on the properties of the intergalactic space are employed to explain the observed data and consequently lead to new insights of the sources itself and the properties of the universe. The predictions are executed with the sophisticated Monte Carlo code CRPropa 2.0 [2] that enable simulation of the UHECR propagation from putative sources to Earth by taking into account all relevant processes. With this procedure the discrimination of the mass composition, the energy spectrum and the maximum energy of the cosmic rays at the sources was possible. Additionally, also the distributions of the sources and the magnetic field are studied.

This thesis is structured as follows. The chapter 2 provides a summary of the physical foundation and methodologies necessary for this thesis. In this context the theoretical predictions for different cosmic ray acceleration models and the resulting source candidates are introduced. The physical principles of the intergalactic cosmic ray propagation and the properties of the intergalactic space as extragalactic and galactic magnetic fields are described. The chapter 3 introduces the Pierre Auger Observatory and gives an overview of the measurements used in this thesis to compare with the predictions from simulations. The chapter 4 introduces the simulation code CRPropa and gives an estimation of the accuracy of the implementation of the pion production interaction as used in this code. In chapter 5 the astrophysical parameter space is constraint by performing a combined fit of the energy spectrum and the mass composition for a spectrum of individual astrophysical scenarios. Chapter 6 makes a prediction of the still not measured ultra high energetic photon and neutrino fluxes for different realistic astrophysical scenarios. The possibility of additional constraints due to the non-observation of this fluxes are discussed and also the competitive of neutrino

and photon upper limits for this purpose is estimated. In chapter 7 predictions are made for the correlation of the cosmic ray arrival directions with the source positions under consideration of different extragalactic magnetic field models as well as a galactic magnetic field. The correlation found for event directions measured by the Pierre Auger Observatory with an AGN catalogue compared to the predictions puts further constrains on the astrophysical scenarios.

2 Physical Foundation

The review of the physical foundation given in this chapter starts with a historical overview of the measurements of cosmic ray in Sec. 2.1.1 followed by a summary of properties of the cosmic rays. Here, in Sec. 2.1.2 the energy spectrum, in Sec. 2.1.3 the mass composition and in Sec. 2.1.4 the distribution of arrival directions are described. Subsequently, possible acceleration mechanisms and source candidates for ultra high energetic cosmic rays are reviewed in Sec. 2.1.5. An explanation of the influences relevant during the propagation of cosmic rays from these possible sources to Earth is elementary for the understanding of the studies in this thesis. These influences includes in Sec. 2.3 the galactic and in Sec. 2.2 the extragalactic magnetic fields, in Sec. 2.4 the interactions with background photon fields and in Sec. 2.4.4 the influence of the expansion of the universe. The production and propagation of ultra high energetic photons and neutrinos are described in Sec. 2.4.2 and Sec. 2.4.3. The main properties of air showers are introduced in Sec. 2.5. In this context parametrisations used in this thesis to calculate important shower properties are discussed in Sec 2.6.

2.1 Cosmic rays

2.1.1 Historical Background

Cosmic rays were first discovered by Victor F. Hess in 1912 during balloon flights up to a hight of 5 km [1]. He measured an increase of ionizing radiation with altitude using electrometers [3] leading him to the conclusion that the origin of this radiation is outside the Earth's atmosphere. He has been awarded for the discovery of these so called cosmic rays with the Nobel prize in 1936. Later measurements of J. Clay [4] showed a dependence of the cosmic ray flux on the magnetic latitude which indicates that a large fraction of them consists of charged particles. A coincident measurement of cosmic rays in two detectors on the ground was shown in 1929 by W. Bothe and W. Kolhörster [5] and were later observed for larger distances of 75 m in the late 1930s independently by Kolhörster [6] and Pierre Auger [7]. This phenomenon was correctly interpreted as the measurement of secondary particles of one primary particle that interacts with the Earth's atmosphere. The cascade of secondary particles initiated by very high energetic cosmic rays are called extensive air showers. In the 1940s several high altitude balloon flights enabled the direct measurement of cosmic rays near the top of the atmosphere. These showed that cosmic rays are full ionized nuclei which travel with nearly the speed of light [8]. Mostly protons [9] but also all other elements up to $Z = 40$ were found in the radiation. From the mid of the 1940s, large detectors were constructed on the ground to measure high amounts of extensive air showers. These

experiments showed a cosmic ray flux decreases with increasing energy which can be described by a power law with fixed spectral index for a large energy range. In 1958 G. V. Kulikov and G. B. Khristiansen [10] discovered a kink at an energy of $\sim 10^{15}$ eV which is now known as the 'knee' of the cosmic ray spectrum. In 1962 the M.I.T. group at Volcano Ranch in New Mexico measured the first cosmic ray with energies above 10^{20} eV [11]. In the 1990s an increasing number of large area ground based detectors with different detection techniques were built, e.g. SUGAR [12], Haverah Park [13], Yakutsk [14], AGASA [15], and Fly's Eye [16]. These measurements established the 'ankle' of the cosmic ray spectrum at energies above 10^{18} eV.

In the first years cosmic rays were the only possibility to perform particle physics. Cosmic ray radiation enabled the discovery of for example the positron [17], muon [18] and pion [19].

2.1.2 Energy Spectrum

Cosmic rays are measured in an energy range that extends over twelve orders of magnitude from a few hundred MeV to ~ 300 EeV, in which the flux per energy decreases by nearly thirty-one orders of magnitude. Starting with more than 1000 particles per second and square meter for cosmic ray energies of a few GeV only less than one particle per km^2 and century are measured above 100 EeV [20]. Consequently, the necessary detection area to collect enough particles in a reasonable time period has to grow with cosmic ray particle energy. Up to 10^{14} eV direct measurements above the atmosphere are feasible. For higher energies only ground based experiments exist.

The energy spectrum follows approximately a power law in energy

$$dN/dE \propto E^{\alpha}$$

which shows a few structures. In Fig. 2.1 these special features in the energy spectrum are pronounced by multiplying the flux with $E^{2.5}$. Up to energies of $3 \cdot 10^{15}$ eV the spectral index is $\alpha \approx -2.7$. After this so called knee position, the spectrum becomes steeper with $\alpha \approx -3.1$. This is usually referred to the end of the galactic proton component. At $8 \cdot 10^{16}$ eV a second knee is reported by KASCADE-Grande [21] with a significance of $2\,\sigma$. Assuming a rigidity dependent maximum energy of sources as proposed by Peters [22] the second knee fits very well the prediction of a 'iron-knee'. Additionally, a flattening of the spectrum of the lightest components is seen by KASCADE-Grande at $10^{17.1}$ with a significance of $5.8\,\sigma$. This could be the transition from galactic to extragalactic light component. Another explanation would also be the set in of a second galactic proton component. Above $10^{18.5}$ eV the whole spectrum flattens again to a spectral index of $\alpha \approx -2.69$, the so called ankle of the energy spectrum. Finally, above $5 \cdot 10^{19}$ eV a steepening is observed which matches to a spectral index of $\alpha \approx -4.2$. This could be explained either by the predicted GZK-effect [23, 24] or the exhaustion of nearby sources. This question will be addressed in Sec. 5.2.4. More details on the current energy spectrum measured by the Pierre Auger Observatory that is used in this thesis is given in Sec. 3.3.1.

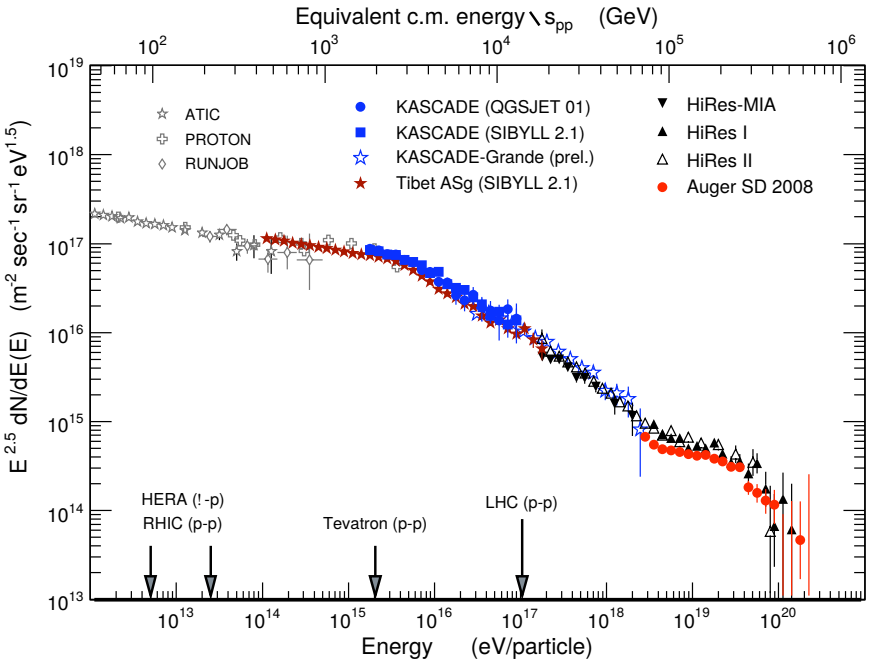

Figure 2.1: All-particle cosmic-ray energy spectrum multiplied by the energy $E^{2.5}$ measured from various experiment taken from [20].

Galactic to Extragalactic Transition Some agreement on the galactic origin of the low energy cosmic rays is established in astroparticle physics because of gamma ray observations of possible acceleration sites [25] within the Milky way. The highest energetic cosmic rays have to be of extragalactic origin due to the lacking capability of the galaxy or the galactic halo to confine these cosmic rays. For the transition from galactic to extragalactic cosmic rays three models are favoured.

In the classical 'ankle model' or 'late transition model' the transition ends well above the angle at energies $E > 10^{19}$ eV [26]. Here a heavy galactic component is replaced by a proton dominated extragalactic flux. Berezinsky et al. [27] suggested the transition already at energies between $10^{16.5}$–$10^{17.5}$ eV, where a sharp change from galactic iron to extragalactic protons takes place. In this 'pair production dip model' the ankle is explained by a pile on of protons from pair production on the CMB which have it's threshold energy at $\sim 10^{18}$ eV. In a third model a mixed extragalactic composition is assumed, which leads to the end of the galactic to extragalactic transition at the ankle as shown for example by [25].

2.1.3 Chemical Composition

All long lived elements of the periodic table are found in the cosmic ray flux. The relative abundances of the elements in cosmic rays directly measured by different experiments at an energy of 1 GeV/nucleon are shown in Fig. 2.2 in comparison to

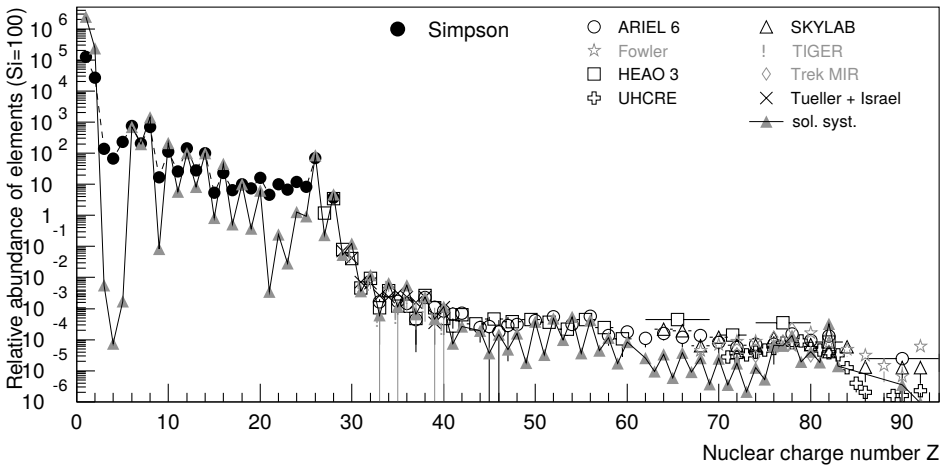

Figure 2.2: Abundances of of the individual elements in the cosmic radiation at 1 GeV/nucleon [20].

the relative abundances of elements in the solar system. In general there is a good agreement between these two distributions, apart from an excess of light elements like lithium, beryllium, boron as well as elements just below iron or lead. Assuming that the cosmic rays have at their origin the same composition like the elements in the solar system, the described overabundances could be the result of spallation processes of the CNO, iron and lead groups with interstellar dust and gas particles during their propagation through our galaxy.

Above 10^{15} eV only ground based observations are possible, which use air showers initiated by cosmic rays in the atmosphere to conclude on primary cosmic ray particles. The most used technique to obtain a mass sensitive observable is the electron to muon ratio. The sum of electrons and muon number is used to derive the primary energy of the cosmic ray. As muons are more penetrating than electrons a common approach is a combination of shielded and unshielded scintillation detectors as used for example by the KASCADE-Grande experiment [28]. The time profile of the shower particles can also be used to discriminate between muon and electron signals. Electrons experience stronger attenuation in atmosphere and therefore appear later in the time trace of the signal.

For energies above 10^{14} eV nearly all the cosmic ray shower energy is deposited in the atmosphere causing an excitation of the air molecules which emit fluorescence light in turn. The light yield is proportional to the energy deposit and is used to measure the longitudinal development of the shower. The depth of the shower maximum is measured in atmospheric slant depth X given in [g/cm^2], which represents the length in equidistant intercepts of traversed matter density. The maximum of the shower development, $X_{\max}$, is sensitive to the primary mass. Heavier nuclei reach their maximum higher in the atmosphere than lighter nuclei.

Besides these techniques the lateral distribution of the shower at ground is also sensitive to the mass of the primaries. Heavier cosmic rays have in general a flatter

distribution than lighter primaries. The energy is estimated from the signal hight at fixed distance from the shower core where the signal is nearly independent of the primary mass. This distance is different for each experiment and scales with the chosen grid size of the detector array. Also the slope of the lateral distribution of Cherenkov light within 120 m from the shower core depends on the hight of the shower maximum and therefore is used to interfere the primary mass.

The results of the $X_{\max}$ measurements from different experiments for the energy range $E \in [10^{15}, 10^{20}]$ eV are shown in Fig. 2.3. From the knee to the second knee a transition from light to heavy elements can be seen. Between the second knee and the ankle again a decreasing of the heaviness is observed. Above $10^{18.6}$ eV an increase of the average mass is seen by the Pierre Auger Collaboration. Regarding the fluctuation $\sigma(X_{\max})$ a narrowing is observed for energies up to 10^{20} eV. The results of the HiRES experiment [29] however indicate a remaining light composition up to the highest energies.

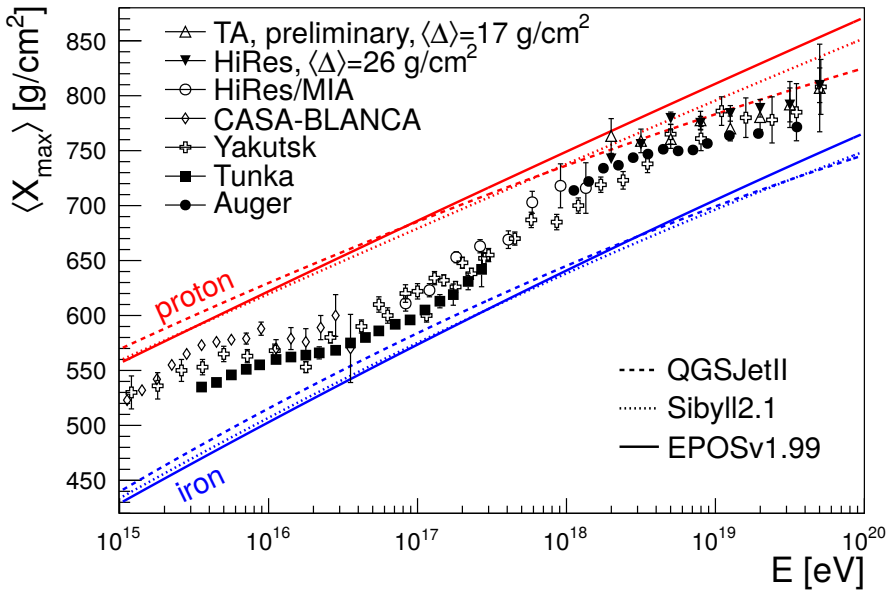

Figure 2.3: Average depth of the shower maximum $X_{\max}$ as a function of primary energy as measured by different experiments taken from [30].

A more detailed description of current $X_{\max}$ measurements of the Pierre Auger Observatory that will be used in this thesis is given in Sec. 3.3.2.

2.1.4 Search for an Anisotropy in the Arrival Directions of UHECR

Cosmic rays are expected to undergo significant deflections in the galactic and extra-galactic magnetic fields and hence a direct identification of sources is not possible.

This challenges different analysis aimed on the directional information of cosmic rays in different energy ranges.

The Lamor radius of cosmic rays below 10^{17} eV is at the same scale as the variation of the turbulent galactic magnetic field. Therefore, propagation of galactic cosmic rays can be described as a random walk and the diffusion-approximation can be used.

For this energy range the Tibet Air-Shower experiment [31] in the northern hemisphere reported a large scale anisotropy for energies from a few to a few hundred TeV and angular scales of 60° and above. This signal is also confirmed by Milagro [32] and IceTop [33, 34] in the southern hemisphere. The signal even remain for PeV energies although the structure of the anisotropy changes with energy. This could be a hint of individual distributions of sources and also individual energy spectra.

Ultra high energetic neutrons should survive significant distances in our galaxy before they decay. Following this motivation a stacking analysis is performed by the Pierre Auger Collaboration [35] with bright galactic gamma ray sources detected by the Fermi-Lat and the H.E.S.S. experiment. In both cases no significant excess is found.

For higher energies the deflection in galactic and extragalactic magnetic fields should decrease to the level of a few degree so that source identification should start to be possible. In Sec. 3.3.5 several analyses from the Pierre Auger Observatory aiming at the highest cosmic ray energies are presented.

2.1.5 Origin of Cosmic Rays

Since the discovery of cosmic rays different models were developed to explain possible acceleration mechanisms. Here, the prevailing theories are introduced and astronomical candidates for possible sources of UHECR are discussed. A more detailed review is given in [36].

Acceleration Mechanisms

Conceptually, one distinguishes between 'top-down' and 'bottom-up' models. In the top-down models cosmic rays are results of the decay of super-massive relic particles with masses $> 10^{20}$ eV. The most prominent models for the origin of relic particles are topological defects [37, 38], super heavy dark matter [39, 40] and the Z-Burst model [41, 42]. These models have the advantage of not demanding any acceleration process as the cosmic rays are directly produced with the desired energies by the decay of the massive particles. But these models are by now disfavoured as they would produce high UHE photon fluxes. Predictions for these photon fluxes are already excluded by the experimental photon flux limits [43, 44]. In the bottom-up models low energy charged particles are accelerated up to UHE ranges. In the following two types of mechanism are discussed.

One Shot Acceleration The 'one shot' mechanism directly accelerates charged particles by altering electric fields and was introduced by W.F. Swann in 1933 [45]. This

phenomena could for example take place on the surface of the sun or other stars. To reach ultra high energies the electric fields in pulsars or active galactic nuclei could be sufficient. This theory is not widely favoured, as the high energy density of the proposed acceleration regions should also causes high energy losses and the observed power law spectrum can not be reproduced easily by this mechanism. Also the needed electrical potential differences would vanish too quickly due to self-induced plasma motion.

Stochastic Acceleration A statistical acceleration generated by encounters of charged particles with a moving magnetized media like magnetic clouds is favoured as many suitable sites exists and a power law is yield as measured experimentally. In this paragraph the properties of this acceleration process are presented. A detailed derivation of this results can for example be found in [46].

In every encounter a test particle with energy E experience an energy gain of $\Delta E = \zeta E$. Starting with an energy E_0 after n encounters the resulting energy E_n is given by

$$E_n = E_0(1+\zeta)^n$$

which yields

$$n = \frac{\ln(E_n/E_0)}{\ln(1+\zeta)}.$$

Given the probability P_{esc} to escape the acceleration region after every encounter results in the number of cosmic rays remaining after n encounters of $(1-P_{\text{esc}})^n$. This yields the number of particles with energies above E_n to

$$N(>E_n) \propto \sum_{m=n}^{\infty}(1-P_{\text{esc}})^m = \frac{1}{P_{\text{esc}}}\left(\frac{E_n}{E_0}\right)^{-\gamma}$$

with

$$\gamma = \frac{\ln(1/(1-P_{\text{esc}}))}{\ln(1+\zeta)} \approx \frac{P_{\text{esc}}}{\zeta}.$$

Hence, a power law energy spectrum is obtained with a spectral index that depends on the details of the mechanism and the conditions of the acceleration site. In particular, stochastic acceleration at two astrophysical environments are discussed.

- **Second order Fermi acceleration** Already in 1949 Enrico Fermi [47] proposed acceleration of particles by encounters with moving magnetized clouds of plasma. After the particle enters the cloud it would undergo diffusive movements and thus the average particle movement aligns to the movement of the cloud. Depending of the relative direction of the incoming particle to the direction of the cloud, the particle gains or loses energy after the encounter. As head-on collisions appear more frequently than tail-on collisions the particle is accelerated on average. Detailed calculations including the Lorentz transformation between the laboratory frame and the rest frame of the cloud and averaging over all incident angle of the particle yields for the fractional energy change

$$\zeta = \frac{\Delta E}{E} \propto \beta^2.$$

This mechanism is named 'second order Fermi acceleration' because the energy gain per encounter is proportional to the second power of the velocity in units of the speed of light, β. Regarding a reasonable velocity of $\beta < 0.1$ in combination with the large distances between the encounters results in a long time scale for this mechanism.

- **First order Fermi acceleration** On the search for a more efficient acceleration method a mechanism was proposed during the 70's that focused on statistic acceleration in the special surrounding of plane wave fronts [48]. This shock front divides two regions with unshocked or 'upstream' region from a shocked or 'downstream' region. The shock front propagates with a velocity $-\vec{u}_2$ and the shocked gas departs after the shock from the front with the velocity $\vec{u}_1$ where $|\vec{u}_2| > |\vec{u}_1|$ is given. In the laboratory frame the downstream region still moves in direction to the shock front with $V = -\vec{u}_2 + \vec{u}_1$. Particle crossing the front from both sides can undergo diffusive scattering in the magnetized plasma and can eventually again cross the shock front. The advantage in respect to the second order mechanism is that always head-on collisions take place. Hence, the fractional energy change is

  $$\zeta \propto \beta$$

  where β is the velocity of the downstream plasma in the laboratory frame in units of the speed of light. The energy gain per encounter is proportional to β and therefore enables a more efficient acceleration and gives the name 'first order Fermi acceleration'. It can be shown, that for strong shocks this mechanism yields a E^{-2} energy spectrum [49].

Source Requirements

A potential acceleration site for cosmic rays have to confine the particles up to the desired energies. For this reason the magnetic fields B and the extension of the object have to meet some requirements depending on the desired maximum energy $E_{\max}$ and the electric charge Z of the particle. Requiring the size of the site R to be larger than twice the Larmor radius of the cosmic ray particle and taking into account the velocity of the scattering centre in case of a statistical acceleration one obtains the condition

$$\left(\frac{B}{10^{-6}\,\mathrm{G}}\right)\left(\frac{R}{1\,\mathrm{pc}}\right) > 2\left(\frac{E_{\max}}{10^{15}\,\mathrm{eV}}\right)(Z\beta)^{-1}.$$

$$\left(\frac{E_{\max}}{10^{15}\,\mathrm{eV}}\right) \approx Z\beta\left(\frac{B}{10^{-6}\,\mathrm{G}}\right)\left(\frac{R}{1\,\mathrm{pc}}\right)$$

as derived in [51].

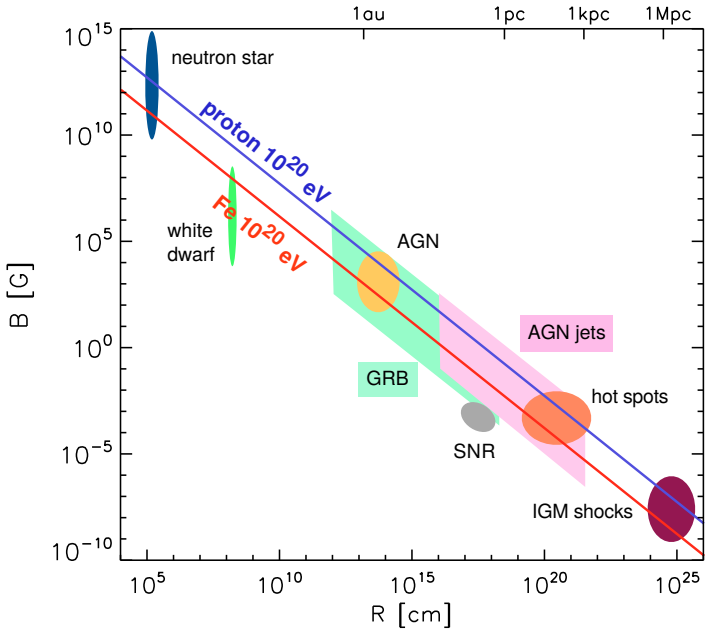

Figure 2.4: An updated overview of the size and magnetic field strength of different UHECR source candidates from [50]. The blue and the red line marks the minimal requirements to achieve a maximum energy of 10^{20} eV for a cosmic ray proton or iron, respectively.

These equations also hold for the one shot acceleration in electric fields which arises from rotation of magnetic fields, B. For this case the rotating velocity $\beta = \frac{\omega R}{c}$ and the size of the rotation region R have to be considered. A graphical representation of R vs. B for different UHECR source candidates along with the required range of parameters to enable a maximum energy of 10^{20} eV is displayed in Fig. 2.4 as originally introduced by Hillas [51]. The region above the blue and red line shows the required R-B combinations to achieve a maximum energy of 10^{20} eV for a cosmic ray proton or iron nuclei, respectively. Here the most optimistic case of $\beta = 1$ is assumed. More realistic lower velocities of the scatter centres or rotation seed of magnetic fields would push the allowed region further to the upper right corner of the plot. The best candidates from this diagram are neutron stars, active galactic nuclei and their surroundings and accretion shocks in the intergalactic medium. This is only a necessary criterion and also other requirements have to be fulfilled by the candidates to ensure cosmic ray acceleration.

Candidates for UHECR Sources

In the following the most promising candidates for acceleration sites are introduced. A more detailed overview is given for example in [52].

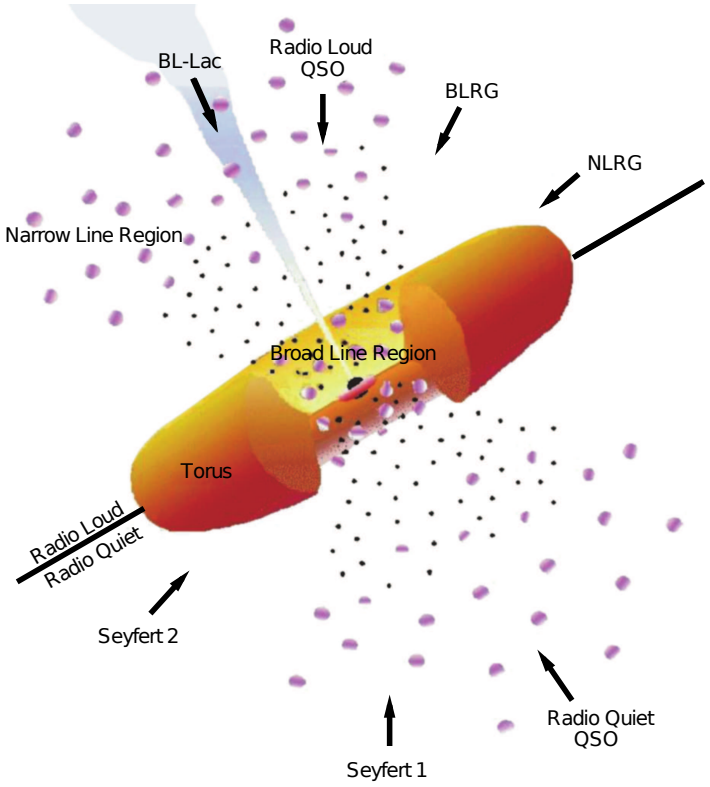

Figure 2.5: AGN unification scheme (taken from [53], originally from [54])

Active Galactic Nuclei Very promising candidates are galaxies which inhabit extremely luminous central regions called active galactic nucleus (AGN). Initially, AGN galaxies which make up about 10 % of all galaxies, were divided in several subtypes related to their observational characteristics. Finally, an AGN unification model emerged, explaining most of the subtypes by different viewing angles of the observer relative to the galactic disk of the AGN which obscured different parts of the galaxy as sketched in Fig. 2.5. In addition, the AGNs can be divided by their radio emission in 'radio quiet' and 'radio loud' AGN. The latter providing 15 % to 20 % of all AGN is the most interesting subtype for a cosmic ray acceleration site.

In the centre of the AGN is a fast rotating very massive black whole that accretes matter from a surrounded disk structure in the plane of the galaxy called the accretion disk. Next to the galactic plane and close to the centre of the AGN lies the broad-line region (BLR) consisting of heated optically thick clouds of gas emitting radiation in form of a line spectrum. It is suggested that these clouds orbit the central region which yield a broadening of the emission lines. The BLR is surrounded by an optical thick torus of gas and dust which obscures the emission from the BLR for low viewing angles relative to the galactic plane. Outside the torus a more or less spherical distribution of also clumpy clouds is assumed, which is named the narrow-line region (NLR). Having roughly the same temperature as the BLR, the absence of the orbital motion results

in narrow emission lines from this region. If the viewing angle is near the galactic disk the BLR is hidden and only narrow emission lines are seen in the spectrum as in case of Seyfert 2 galaxies and narrow line radio galaxies (NLRG). Using an older classification scheme for radio galaxies these galaxies would corresponds to the Fanaroff-Riley I (FRI) type galaxies [55]. For a higher viewing angle also the BLR is visible which results in Seyfert 1 galaxies and broad line region radio galaxies which would also correspond to the Fanaroff-Riley type II galaxies (FRII). If the observational direction is perpendicular to the galactic disk the bright central region is directly seen. This corresponds to the radio loud quasi stellar objects (quasars) and radio quiet quasi stellar objects (QSO).

Radio loud AGNs eject jets from the central region containing relativistic particles, plasma and the therein confined magnetic fields. The jets are generated by magneto-hydrodynamic processes during the accretion of the matter through the rotating black whole. The matter along with the confined magnetic field rotates with the black whole which is called frame dragging. Magnetic fields with opposite polarization overlap and annihilate. Therefore the magnetic energy can be transferred into kinetic energies of the plasma. A similar magnetic reconnection procedure is for example used to explain the formation of solar winds. The ejection of the plasma is pulsed and causes so called blobs or knots causing short active periods called flares followed by longer rest periods.

BL-Lacertae (BL Lac) objects which show highly polarized and variable spectra may be AGN where we directly look into the direction of the jet. Also a combination of the properties of quasars and BL Lac galaxies exists which are called blazars.

The radio signal from these galaxies stem from relativistic electron in the jets doing synchrotron radiation by movements in the magnetic fields. When the matter in the jets hit the inter cluster medium or remnants of previous ejection shock waves can be produced. This could be an explanation of high radio intensity regions called the hot spots observed in some AGN jets. With further propagating into the inter galactic space the particles cool down by synchrotron radiation submitting further radio emission and filling fast areas which then are called radio lobes. These radio lobes are also regions of termination shocks. The acceleration of cosmic rays is proposed in the central region, the jets, the hot spots and the lobes of AGN [36]. But the central region is disfavoured for the acceleration to ultra high energies as high energy losses are expected by interaction with the high photon density [56].

Beside the radio luminosity, AGN differ in the mass of the central black hole which yields a variation of the total luminosity.

Pulsars Another very promising candidate for cosmic ray sources are fast rotating neutron stars which are called pulsars and are described in [57]. Neutron stars are mainly made out of neutrons but they have a crust consisting of protons, heavy ions and electrons [58]. The fast rotation of the giant magnetic fields of $B \sim 10^{11}\,\mathrm{G}$ or even $B \sim 10^{14}\,\mathrm{G}$ for so called magnetars induces electric fields that could accelerate charged particles to cosmic ray energies. The capability to accelerate particles up to energies of $10^{20}\,\mathrm{eV}$ only exists during the first days after formation of the magnetar after which

the rotation speed significantly decreases allowing only maximum cosmic ray energies of several EeV. As one possible site for non Fermi like acceleration much harder energy spectra as $dN/dE \propto E^{-1}$ are possible as shown for example in [59]. Accounting for the abundance and energy output of magnetars it would be sufficient if 10 % of them would accelerate cosmic rays to energies of 10^{20} eV, to realize the observed UHECR flux.

Gamma Ray Burst Gamma ray bursts (GRBs) are the most luminous electromagnetic events in the universe appearing only for small periods from 30 ms up to 100 s roughly once a day. These phenomena originate from massive explosions which also lead to a formation of multiple shock regions. Statistic acceleration in these shocks as shown for example in [60, 61] could possibly yield cosmic ray energies up to 10^{20} eV. The transient nature of the GRB could be one possible explanation for the lack of correlation of the highest energetic measured cosmic rays with source candidate catalogues. One weak point of this candidate is their need of a high GRB activity as most GRB are measured from distant galaxies with z>1.

Gravitational Accretion Shocks A possible acceleration in large scale structures as galaxy clusters, filaments and galaxy walls is discussed for example in [50]. The gravitational structure formation on these large scales could cause shocks in the inter cluster medium and in the filaments with extensions up to 1–10 Mpc and a speed of few thousand km/s. The magnetic field of μG order allow to confine charged particles up to 10^{20} eV. Calculations show that protons could be accelerated up to energies of a few times 10^{19} eV in such shocks [62].

Starburst Regions Starburst galaxies are in a stage of strong star formation periods. They also inhabit a large amount of giant stars and have consequently a high supernova rate. These starburst regions emit a wind of plasma that produces strong termination shocks at the outer regions of the galaxies. The time a galaxy stays in this stage is less than $\sim 10^8$ yr and the number density of galaxies that hosted a starburst in the last 1 Gyr is $10^{-4}\mathrm{Mpc}^{-3}$ [63]. These starburst galaxies are also suggested to be sources of UHECR [64]. The acceleration is proposed to be performed in a two step procedure. At first, particles are accelerated in supernova remnants up to energies of 10^{15} eV. These cosmic rays leave quickly the starburst region through a convective transport by the wind instead of a slower diffusion, which would cause disintegration. The second acceleration to ultra-high energies occurs then in the termination shocks.

2.1.6 Source Evolution

The density ρ of the general matter density as well as the density of potential cosmic ray source candidates have been passed through an evolution with redshift, z. The mass density in general is traced by measurements of the star formation rate (SFR) as done by [66, 67]. The emissivity increases with $(1+z)^{3.4}$ for $z < 1$ followed by a

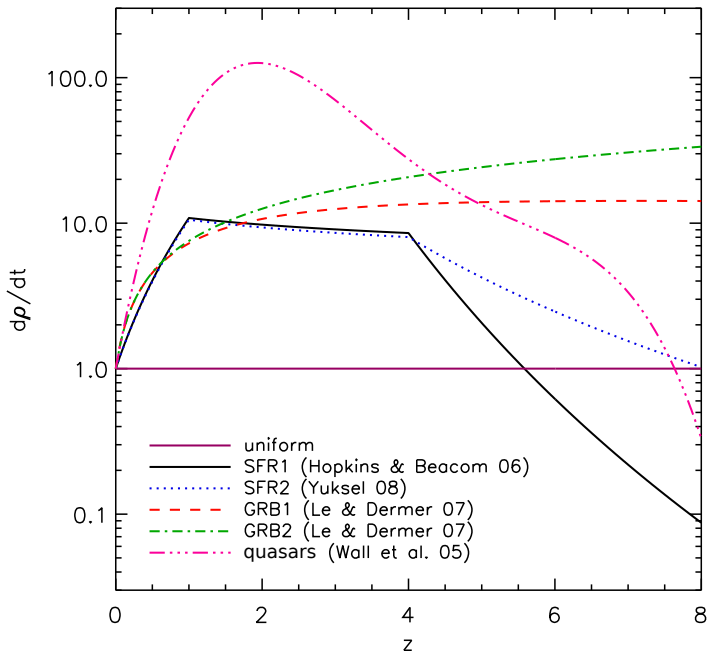

Figure 2.6: Evolution of the co-moving density with redshift for different astrophysical objects slightly modified from Kotera et al. [65]. Two different versions of the evolution of the star formation rate SFRI [66] and SFRII [67], two versions of the rate of gamma ray bursts GRBI and GRBII [68] and the evolution of quasars [69] are shown.

nearly flat region with $(1+z)^{-0.3}$ between $1 \leq z \leq 4$ and a decrease with $(1+z)^{-3.5}$ for $z \geq 4$ [67]. Pulsars and star burst galaxies follow this general evolution as used for example in [70] and [71]. GRB show a departure from the evolution seen from SFR especially for higher z, where still an increase is seen in case of GRB [72, 68, 73, 74]. In [68] for example two different models are parametrized with $(1+8z)/(1+(z/3)^{1.3})$ (GRB1) and $(1+11z)/(1+(z/3)^{0.5})$ (GRB2). The evolution of the density with redshift of radio loud AGN galaxies shows even stronger increase for small z compared to SFR and GRB. Especially for quasars (in [69] denoted as FRII galaxies) this yields the parametrization $\log \dot{\rho} = 2.7z + 1.45z^2 + 0.18z^3 - 0.01z^4$ from [69]. Fig.2.6 shows a comparison of the density evolution with z for the different astrophysical objects taken from [65]. Here, also a uniform distribution is displayed which is in general disfavoured. Even though in [75] this evolution is discussed for the case of FRI galaxies.

2.2 Extragalactic Magnetic Fields

Observations show magnetic fields of different strength in the Universe in huge structures like in galaxy clusters (a few μG) [76] and filament of superclusters [77].

Theoretical models for the origin of these fields exist, which describe the formation as a combination of two processes. At first, a primary seed field is needed. Candidates for

these seeds are primordial magnetic fields produced for example during the electroweak phase transition right after the big bang or fields produced through cluster acceleration shocks in the so called Biermann battery effect [78]. Once such a seed exists it can be amplified through magnetohydrodynamical processes during the large scale structure formation processes of the Universe in which galaxies, galaxy clusters and superclusters were formed. This could for example explain the fields measured in galaxy clusters.

For the propagation of cosmic rays in particular the spaces between superclusters, the so called voids, are important. As magnetic field measurements of this regions were not successful yet, numeric simulations of the large scale structure formation of the Universe can supply predictions for magnetic fields in this regions as for example in [79, 80, 81, 82, 83].

In this thesis, one model with strong magnetic field strength by Miniati et al. [84] and one with weaker fields by Dolag et al. [81] are used.

In [84] the hydrodynamical flow of dark matter and baryonic gas is calculated along with the passive magnetic fields. The expected magnetic fields of up to μG are assumed not to effect the dynamics of large scale structures and hence their influence is neglected. For this simulation an Eulerian grid based total hydro + N-body code [85] with box size of $50\,h_{67}^{-1}\,\mathrm{Mpc}$, a dark matter component described by 256^3 particles and a gas component on a comoving grid of 512^3 zones are used. This results in a fixed resolution in the whole simulation box. The simulation starts at $z \simeq 60$ with a zero magnetic field after which the seed fields are generated at cosmic shocks by the Biermann battery effect [78]. The large scale structure are not connected to the real Universe although this magnetic field is good to study the statistical properties of the UHECR propagation. The initial distribution of these seeds are chosen arbitrarily so that the localisation of the magnetic field structure in the end have no correlation with the real Universe. But the strength and structure should be realistic. The simulation predicts magnetic fields in the voids of the order of 10 fG and an average field in the whole simulated space of the order of 10 nG [79].

In [81] a smoothed-particle-hydrodynamic method is used to simulate large scale structure formation. In this grid free Lagrangian method an adaptive resolution is possible which improves the description especially in the galaxy cluster regions. The simulation is constrained by the large scale structure of the nearby Universe within 110 Mpc around the Milky Way. The whole simulation is performed in a periodic box with 343 Mpc edge length where the region outside the constrained volume is filled with low resolution dark matter to take into account the long range gravitational forces. A homogeneous seed field is assumed which is justified by previous results from simulations of galaxy clusters with a uniform seed field that show good agreement with data. Back-reactions of the magnetic field on the ionized gas is taken into account.

In [84] about 10 % of the volume contains a magnetic field with 10^{-9} G and a fraction of 10^{-3} a field above 10^{-6} G, whereas in the predictions from [81] the corresponding proportions of the space account $< 10^{-4}$ and $3 \cdot 10^{-6}$, respectively. This differences have a severe impact on the deflection of cosmic rays and stem most probably mainly from the differences in the simulation methods as already stated in [84].

2.3 Galactic Magnetic Field

Also in our galaxy magnetic fields are omnipresent in small constrained regions like around stars, supernova remnants or pulsars as well as on large scales in the interstellar medium where it's strength ranges from $\sim 1\mu$G to $\sim 10\mu$G [86]. The knowledge of these magnetic fields mainly stems from Faraday rotation measurements and synchrotron radiation, which both are measured as integrated value in line-of-sight. As no in situ measurements are available, models of the magnetic field in our galaxy have to be applied to the data to interfere the magnetic field map of our galaxy. In this thesis, the model from Janson and Farrar [87, 88] is used as it shows an improved agreement with galactic magnetic field data compared to other models as given in [89, 90, 91]. This model is made up of three different components that belong to different physical origins. On the large scale, a regular field exists which is supplemented by a small scale random field with coherence length of 100 pc which is caused by different phenomena as for example supernova outflows. The third component is the striated random field which is aligned along some particular axis on large scale but varies in strength and sign on small scales. These fields have their origin in the levitation of bubbles of hot plasma which contain random magnetic fields.

Further the GMF model is composed of a galactic disk component and a halo component, where the halo itself consists of a toroidal Halo component and a so called out-of-plane component. The latter is also called X-shaped component and is partly motivated by X-shaped structures seen in the radio measurements. This model has a large number of free parameters which are used to optimize the model to over 40000 extragalactic rotation measures and the WMAP7 galactic synchrotron map.

The deflection in galactic magnetic fields is applied to the directions of the simulated cosmic rays from 3d simulations by using the so called 'magnetic' lenses which have been introduced in the PARSEC simulation engine [92], but can be used also in other simulation frameworks. In the lensing approach, the arrival directions n on the surface of a sphere around our galaxy and the directions m at the observer are pixelised for this purpose. For the observer only the position inside the galaxy and the direction of the incoming particle are relevant. The position on the surface of the observer can be neglected as regarding the small size of the Earth compared to the galaxy. The same is also presumed for the galaxy, which is justified compared to the intergalactic distances assumed for UHECR propagation. Because of this, the arrival directions at the edge of our galaxy are averaged over all points of entry on the galactic surface. In conclusion, one direction n can be observed in different directions at the observer. Backtracking simulations in galactic magnetic field models are used to derive the transition probability $l_{m,n}$ from one direction n to one direction m for different energy bins i. The matrix $\mathbf{L_i}$ is build up of these $l_{m,n}$ and represents the galactic lens for an energy bin E_i. Assuming a vector $\mathbf{p^i_{eg}}$ consisting of j components which are the probabilities of the extragalactic arrival direction $(\theta, \phi)_j$ at one energy E_i. $\mathbf{L_i}$ can now be used to convert $\mathbf{p^i_{eg}}$ to an according vector $\mathbf{p^i_{0bs}}$ at the observer executing the matrix multiplication

$$\mathbf{L_i} \cdot \mathbf{p^i_{eg}} = \mathbf{p^i_{obs}}.$$

Additionally, the normalisation

$$\mathbf{L_i} = \frac{1}{\max\|\tilde{\mathbf{L}}_\mathbf{i}\|_1}\tilde{\mathbf{L}}_\mathbf{i}$$

is applied to avoid the deformation of the energy spectrum. $\tilde{\mathbf{L}}_\mathbf{i}$ is here the matrix that is directly derived from backtracking of isotropic directions from the observer. Due to the small propagation distance inside the galaxy no energy loss processes have to be taken into account.

2.4 Propagation of UHECR

2.4.1 Interactions with the Photon Background

UHECRs experience various interactions on their way from their sources to Earth. Nucleons above the energy threshold of 10^{18} eV lose energy due to production of e^--e^+ pairs in interactions with photons from the cosmic microwave background (CMB) [93]. Nucleons with energies above $7 \cdot 10^{19}$ eV also lose energy by producing pions in interactions with CMB. This was predicted by Greisen [23] and independently Zatsepin and Kuzmin [24] in 1966 and therefore called is GZK-effect. The cross section for this photo-pion production increases strongly at the $\Delta^+(1232)$ resonance. In case of a proton, the process can be described as

$$\begin{aligned} p + \gamma_b \rightarrow \Delta^+(1232) &\rightarrow p + \pi^0 \\ &\rightarrow n + \pi^+. \end{aligned}$$

For higher energies also further baryonic resonances like $\Delta(1620)$ and $\Delta(1700)$ and further processes like

$$p + \gamma_b \rightarrow \Delta^{++} + \pi^- \rightarrow p + \pi^+ + \pi^-$$

become possible. These interaction also take place with the infrared background field where the higher energy of the photons causes a significant contribution at lower nuclei energies as for the CMB interactions as displayed in the left plot of Fig. 2.7. A significant role of the pion production on the infrared background is given for nucleon energies between 10^{17} eV and $5 \cdot 10^{19}$ eV.

As nucleons, also nuclei lose energy by pair production. Whereas the GZK-effect leads to photodisintegration of the nuclei due to several processes. In the right plot of Fig. 2.7 the cross section for the different GZK interaction processes are shown for iron nuclei. At low energies Giant dipole resonances (GDR) dominate which are a collective excitations of the whole nucleus. The photon energy E_γ in the rest frame of the nucleus have to be in the range $10-50$ MeV. The main decay channel is the emission of one nucleon. The emission of α particle or 2, 3 and 4 nucleons are also significant for some nuclei. At higher energies of the nuclei corresponding to $E_\gamma \simeq 30$ MeV the

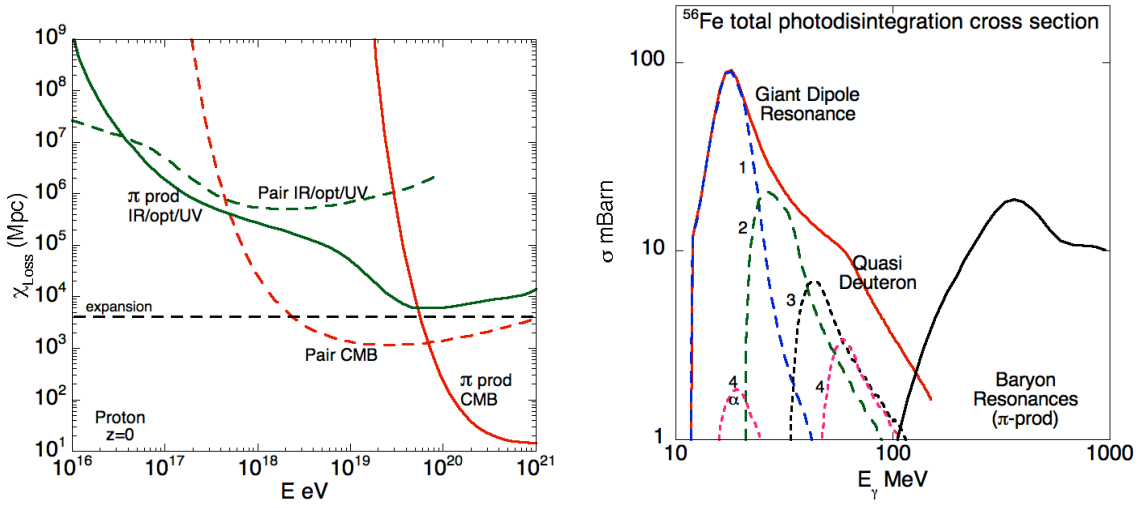

Figure 2.7: **Left:** Energy loss length of protons for different interaction processes [93]. **Right:** Different cross sections for iron [93].

quasi-deuteron (QD) process is in the order of the GDR are and starts to dominate at higher energies. In this process the incoming photon interacts with a proton-neutron pair. The QD process mainly emits multiple nucleons. Above 150 MeV photon energy in the rest frame of the nucleus, which corresponds to $5 \cdot 10^{21}$ eV in the lab frame for a iron interacting with the CMB, the photopion production, also known as baryonic resonance (BR) becomes dominant. Besides the pion which can also be absorbed inside the nucleus, several nucleons are emitted in this interaction. $E_\gamma > 1$ GeV corresponds to nuclei energies well above 10^{21} eV even for protons and hence have not to be considered for UHECR propagation. In the left plot of Fig. 2.8 one can see that the minimal energy loss length of nuclei is well below that of protons. Only iron nuclei have an energy loss length in the order of the protons at least in the energy range below $10^{20.4}$ eV. This results in higher stability of iron nuclei compared to other nuclei. Regarding the energy evolution of the energy loss length a first drop at $A \times 10^{18}$ eV due to a combination of photodisintegration on far-infrared and pair production on the CMB can be seen in the right plot in Fig. 2.8. At $A \times 4 \cdot 10^{18}$ eV the second steep decrease due to photodisintegration on the CMB is visible. This predicted steepening at the highest energies is also called GZK-suppression. As described in Sec. 2.1.2, such a behavior is seen in the measurements of the HiRes experiment [94] and The Pierre Auger Observatory [95]. But this is not a clear proof of the GZK-suppression, because also other explanations of the observed steepening exists like the exhaustion of the acceleration processes. This will be further discussed in Sec. 5.2.4.

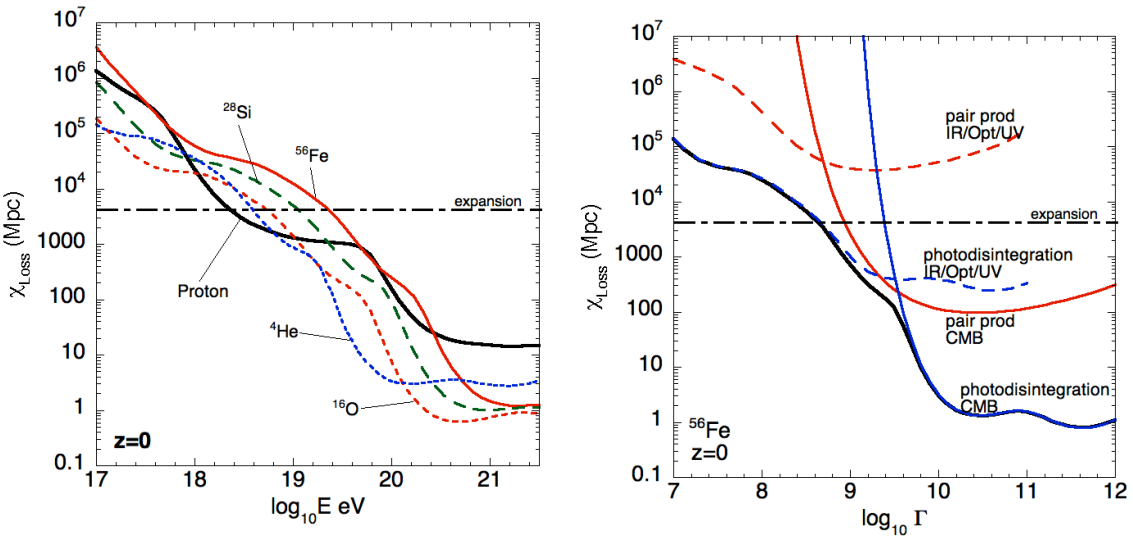

Figure 2.8: **Left:** Energy loss length for different nuclei [93]. **Right:** Energy loss length for iron nuclei showing the different subprocesses and photon background fields in dependence of the Lorentz factor Γ [93].

2.4.2 Ultra High Energetic Photon Production and Propagation

Photons with energies ranging from radio waves over infrared, optical, ultraviolet, x-rays up to gamma rays are the main messenger of the universe. At the high energy end, gamma rays up to 10^{14} eV have been observed with atmospheric Cerenkov telescopes in recent years [97]. Large area cosmic ray experiments like the Pierre Auger Observatory allow to search for photons exceeding energies of 10^{18} eV. These photons are predicted from different production mechanisms of cosmic rays. In most models, photon pairs are produced in decays of UHE neutral pions originating from primary processes as stated in Sec. 2.1.5 and Sec. 2.4.1. The photons produced in the decay of the pion have a factor of ~ 10 times [96] lower energy than the cosmic ray nucleon from which it originates. In the Z-burst model [41, 42] UHE neutrinos annihilate on relic neutrinos leading to resonant production of Z-bosons which then decay into photons and neutrinos.

Once produced, these UHE-photons can generate electromagnetic cascades by interacting with the low energy photon background γ_b. High energy photons produce multiple electrons and positrons, which again produce high energetic photons by inverse Compton scattering. These new photons again produce higher energetic electrons and positrons and the cascade continues. In these electromagnetic cascades, the photons lose energy until their energy falls in the GeV to TeV region, where the universe becomes transparent for photons, as can be seen in Fig. 2.9. The relevant interaction

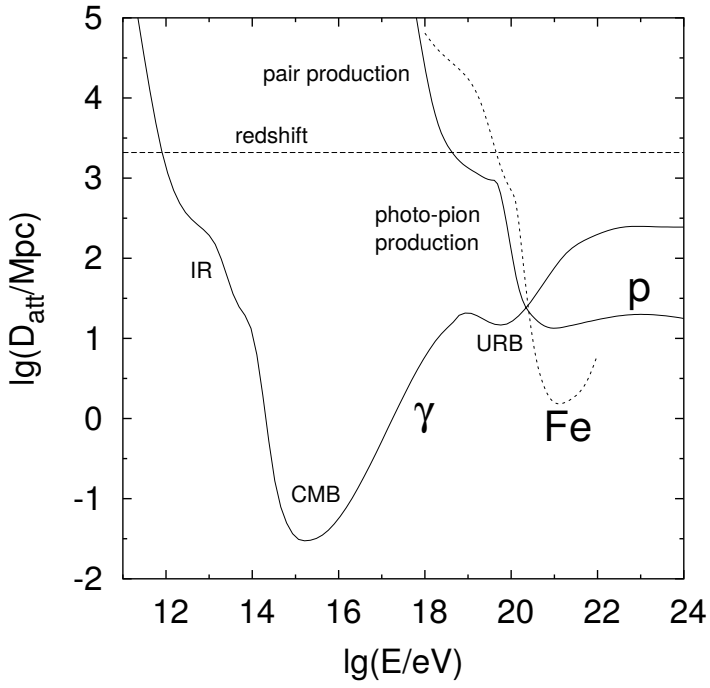

Figure 2.9: Energy loss length of photons, protons and iron[96].

for this cascades are

pair production	$\gamma + \gamma_b$	$\rightarrow$	$e^+ + e^-$
double pair production	$\gamma + \gamma_b$	$\rightarrow$	$e^+ + e^- + e^+ + e^-$
inverse Compton scattering	$e + \gamma_b$	$\rightarrow$	$e + \gamma$
triplet pair production	$e + \gamma_b$	$\rightarrow$	$e + e^+ + e^-$

The electron-positron component of the electromagnetic cascade also loses energy by synchrotron radiation in extragalactic magnetic fields. The photons produced in this process again can enter the electromagnetic cascade.

Also minor contribution of photons from interaction of cosmic rays with matter directly at the sources could be possible as described in [98].

2.4.3 Ultra High Energy Neutrino Production and Propagation

Observing cosmic rays in the UHE regime also give reasons to expect neutrinos with nearly the same energies [99]. The source of these neutrino fluxes should be similar to the one of UHE photons as introduced in the previous section. A direct production in the vicinity of the cosmic ray sources is expected in the interactions of UHE nucleons and nuclei with matter and radiation in this environment. The pion originated in these processes have the neutrinos as decay products. The already mentioned GZK-effect that also should produce UHE photons also leads to UHE-neutrinos from the cosmic ray propagation. Once the neutrinos are produced they should reach Earth without disturbance due to the low interaction cross section.

2.4.4 Cosmological Effects

The expansion of the universe has influence on the emission and propagation of cosmic rays. Four effects are sketched in the following. A flat universe with a ΛCDM cosmology with the Hubble parameter

$$H(z) = H_0\sqrt{(\Omega_{m,0}(1+z)^3 + \Omega_{\Lambda,0})}$$

as given for example in [36] is assumed. In this work the following values are used for the dark matter density $\Omega_{\Lambda,0} = 0.7$, the matter density $\Omega_{m,0} = 0.3$ and the Hubble constant $H_0 = 0.72 \cdot 100\,\mathrm{km\,s^{-1}Mpc^{-1}}$ as measured by the WMAP satellite [100].

In Sec. 2.1.6 it was already pointed out that the density of potential sources related to the comoving volumes evolves with the redshift z due to the formations of these sources. In addition the source density also increases as the space shrinks with z. The second influence of the expansion of the universe is the increase of the time interval between two events with time. Conclusively, the observed luminosity ($L(z)$) of distant sources that emitted a luminosity L_0 at redshift z also decreases with $L(z) = L_0/(1+z)$.

The third point is the energy loss due to adiabatic expansion of the universe which can be described with $E(z) = (1+z)E(z=0)$. This leads to an adiabatic energy loss length of $L_{ad} = \frac{c}{H(z)}$.

And finally also the density n of the photon background at energy ϵ at z increases due to the smaller volume compared to the density at $z = 0$ with

$$n(\epsilon, z) = (1+z)^2 n\left(\frac{\epsilon}{1+z}, z = 0\right)$$

This decreases especially the interaction length λ for the different interactions of the cosmic rays with the photon background and so translates into

$$\lambda^{-1}(E, z) = (1+z)^3\lambda^{-1}((1+z)E, z = 0)[2]$$

For the infrared, ultraviolet, visible and the radio background the production of these backgrounds itself has to be considered in addition, which counteracts the effect from the expansion.

2.5 The Development of Air Showers

In Sec. 2.1.2 it is described that the cosmic ray flux at the highest energies is too low for direct measurements but their energy is sufficient to create particle cascades that can be measured at ground level. Every single cosmic ray that hits the molecules at the top of the Earth atmosphere causes these cascades which are called 'extensive air showers'. For example one vertical cosmic ray proton with the energy of $10^{19}\,\mathrm{eV}$ would yield a foot print at sea-level with 10^{10} secondary particles which extents over several kilometres [103]. The cascade of secondaries propagates with nearly speed of light in a so called 'shower front' which has a thickness in the order of meters as

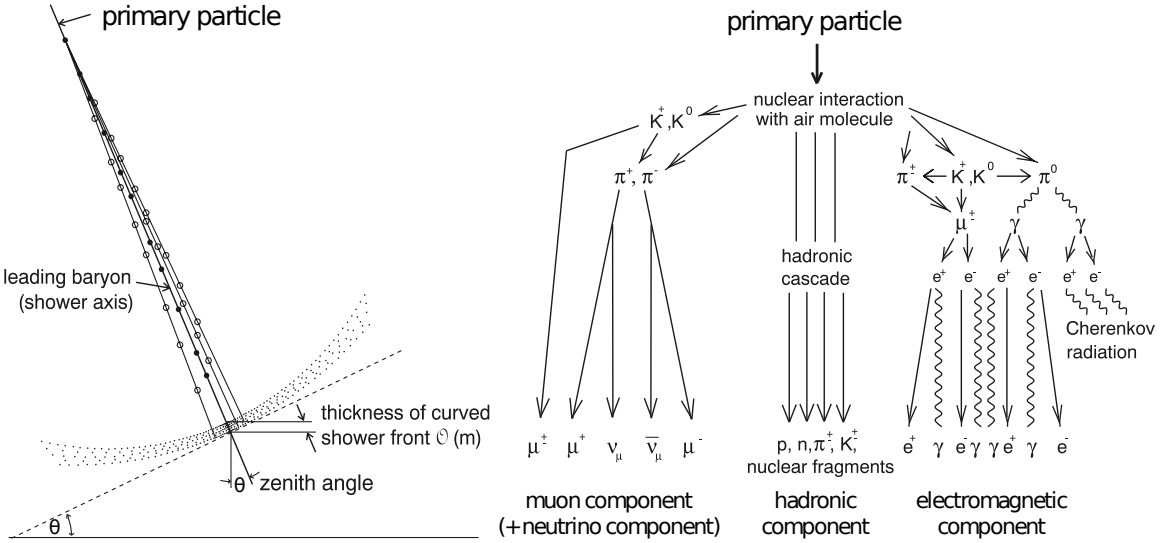

Figure 2.10: **Left:** Sketch of the geometry of an extensive air shower. **Right:** Main processes in the development of air showers separated by component. Taken from [101] and originally from [102]

sketched in Fig 2.10. The processes in air showers are divided into three components to handle their complexity. These are the electromagnetic, the hadronic, and the muonic component by taking into account the individual interactions. The development of the first two components basically determine the development of the whole shower and will be discussed in the following. Once produced, muons and neutrinos in showers with a zenith angle up to $\theta = 80°$ do not interact or decay over the time scale of the shower development.

2.5.1 Electromagnetic Cascade

Electromagnetic cascades contain electrons, positrons and photons. For the basic understanding of the development of electromagnetic cascades an analytic model has been introduced by Heitler [104]. In this model, only bremsstrahlung for electrons and positrons and pair production for photons are considered, assuming equal cross section independent from the energy for both interactions. The interplay of these two processes leads to the cascade having the particle number after n propagated interaction length of $N = 2^n$. The energy of the parent particle is evenly distributed between the two child particles in each step which leads to an average energy of $E_n = E_0/N$ per particle in the cascade after n steps assuming the first particle starts with the energy E_0. Below the critical energy of $E_c \sim 80\,\mathrm{MeV}$ the ionization dominates over the bremsstrahlung which stops the cascade as the photons from the ionization process have not sufficient energy for pair production.

This model is obviously not accurate as it neglects other interaction as for example multiple photon production due to bremstrahlung and also overestimated the electron

interaction length. In comparison with simulations [101] it is shown that for example the maximum number of particles at the end of the cascade are overestimated by a factor of two to three. This model also leads to two times more electrons than photons, although some simulations show six times more photons than electrons.

Nevertheless this simple model provides a fundamental understanding of the air shower and can also predict important properties as the maximum number of particles at the shower maximum which is proportional to the primary energy

$$N_{\max} \propto \frac{E_0}{E_c}.$$

Important is the corresponding slant-depth $X_{\max} = n_{X_{\max}} d + X_0$ at the shower maximum which is reached after $n_{X_{\max}}$ interactions each after a length d from the beginning depth X_0. Having $d = \lambda_r \ln(2)$ with the radiation length $\lambda_r = 37\,\mathrm{gcm}^{-2}$ this results in

$$X_{\max}^{\mathrm{em}} = X_0 + \lambda_r \ln\left(\frac{E_0}{E_c}\right).$$

2.5.2 Hadronic Air Showers

A similar approach as chosen for the electromagnetic one is used for the model of hadronic cascades. Again a constant distance between interactions is chosen with $d = \lambda_{\mathrm{I}} \ln(2)$ using the interaction length $\lambda_{\mathrm{I}} = 120\,\mathrm{gcm}^{-2}$ which is assumed constant for all particles. In every interaction N_{tot} secondaries are produced distributing the primary energy of the parent particle evenly to these products. Here only charged and uncharged pions are considered with an ratio of ~ 2 resulting from the fact that pions form an isospin triplet under the strong interaction. The neutral pions decay in two photons which immediately starts an electromagnetic cascade whereas the charged pions continue the hadronic cascade. Hence, after each interaction one third of the energy is transferred to the electromagnetic component. For energies above $10^{14}\,\mathrm{eV}$ more than five interactions occur in average and hence nearly all energy is transferred to the electromagnetic component. The cascade proceeds until the energy of the charged pions drops below the critical energy of $E_{\mathrm{c}}^{\mathrm{H}} = 20\,\mathrm{GeV}$. Again, this simple model allows to draw conclusions that are confirmed by detailed simulations. Assuming that every charged pion produces one muon, the dependence of the number of muons at the shower maximum from the energy of the initial particle and the multiplicity of the charged pions N_{ch} is given by

$$N_{\mu}^{\max} = \left(\frac{E_0}{E_{\mathrm{c}}^{\mathrm{H}}}\right)^{\beta}$$

with $\beta = \frac{\ln(N_{\mathrm{ch}})}{\ln(3/2 N_{\mathrm{ch}})}$. Nuclei are treated as a superposition of A nucleons each with a energy of E_0/A which gives the result

$$N_{\mu}^{\max} = A\left(\frac{E_0/A}{E_{\mathrm{c}}^{\mathrm{H}}}\right)^{\beta} = \left(\frac{E_0}{E_{\mathrm{c}}^{\mathrm{H}}}\right)^{\beta} A^{1-\beta}.$$

Also the fraction of the total energy dedicated to the electromagnetic part E_{em} of the air shower can be derived from this model. As the energy in the hardronic part of the air shower is calculated to $E_{\mathrm{H}} = N_{\mu}^{\max} E_{\mathrm{c}}^{\mathrm{H}}$ one gets

$$\frac{E_{\mathrm{em}}}{E_0} = 1 - \left(\frac{E_0}{E_{\mathrm{c}}^{\mathrm{H}}} \right)^{\beta - 1} A^{1-\beta}.$$

The atmospheric depth of the hadronic shower maximum can be approximated by the one of the electromagnetic shower initiated after the first interaction. Hence, the additional hadronic interaction length and the distribution of the primary energy have to be considered and yield for a nucleon primary

$$X_{\max}^{\mathrm{had}}(E) \sim \lambda_{\mathrm{had}} + X_{\max}^{\mathrm{em}} \left(\frac{E}{N_{\mathrm{tot}}} \right).$$

Air showers triggered by a nucleus will not change the total number of particles in the shower maximum compared to pure electromagnetic showers, as the amount of energy for particle production stays the same. But the number of muons in the shower maximum and the atmospheric depth of this is altered for nuclei

$$N_{\mu}^{A} \approx A^{1-\beta} N_{\mu}^{\mathrm{had}},$$

respectively

$$X_{\max} \approx X_{\max}^{\mathrm{had}}(E/A) = X_{\max}^{\mathrm{had}}(E) - \lambda_{\mathrm{r}} \log_2(A).$$

The superposition model also suggested that the shower to shower fluctuation of the $X_{\max}$ should be reduced with increasing mass by the relation

$$\sigma(X_{\max}) \sim 1/\sqrt{A}$$

compared to protons.

2.6 Parametrization of the $\langle X_{\max} \rangle$ and $\sigma(X_{\max})$

In Sec. 2.5 it is introduced that the mean value of the depth of the shower maximum $\langle X_{\max} \rangle$ and the standard deviation for the shower to shower fluctuation $\sigma(X_{\max})$ can be used as a measure of the mass of the primary cosmic ray particle on top of the Earth atmosphere. For the translation of $X_{\max}$ measurements into the information of the primary particle mass and vice versa the interactions in the atmosphere have to be considered. An interpolation of the hadronic interaction cross sections to the energies relevant in air showers are necessary as only data from particle accelerators at lower energies are available. For this purpose, simulations of the air shower development are usually performed with a variety of different models for the interpolation of the hadronic interaction, which is a source of uncertainty.

In this thesis the calculation of $\langle X_{\max} \rangle$ and $\sigma(X_{\max})$ from the mass number received from the simulations is done by the parametrizations derived in [105, 95]. These

parametrizations are based on the generalized Heitler model for extensive air showers as given in [106]. The parameters are derived by air shower simulations performed with the CONEX [107] code for different hadronic interaction models.

For the mean of the shower maximum one gets

$$\langle X_{\max} \rangle = \langle X_{\max} \rangle_{\mathrm{p}} + f_{\mathrm{E}} \langle lnA \rangle$$

with

$$f_{\mathrm{E}} = \xi - \frac{D}{\ln(10)} + \delta \cdot \log_{10} \left(\frac{E}{E_0} \right)$$

and

$$\langle X_{\max} \rangle_{\mathrm{p}} = X_0 + D \log_{10} \left(\frac{E}{E_0} \right).$$

The dispersion of the maximum of shower depth is given by

$$\sigma(X_{\max}) = \sqrt{\langle \sigma^2_{\mathrm{sh}} \rangle + f^2_{\mathrm{E}} \sigma^2_{\ln A}}$$

with

$$\langle \sigma^2_{\mathrm{sh}} \rangle = \sigma^2_{\mathrm{p}} [1 + a \langle \ln A \rangle + b \langle (\ln A)^2 \rangle]$$

$$\sigma^2_{\mathrm{p}} = p_0 + p_1 \log_{10} \left(\frac{E}{E_0} \right) + p_2 \left[\log_{10} \left(\frac{E}{E_0} \right) \right]^2$$

$$a = a_0 + a_1 \log_{10} \left(\frac{E}{E_0} \right).$$

The mean depth for proton showers X_0 at the reference energy $E_0 = 10^{19}\,\mathrm{eV}$, the elongation length D, and the parameters ξ, δ, p_0, p_1, p_2, a_0, a_1 and b are obtained for different hadronic interaction models as given tables in [105, 95].

3 The Pierre Auger Observatory

The Pierre Auger Observatory [109] is currently the largest experiment dedicated to measure cosmic rays at the highest energies. The observatory is located in the Pampa Amarilla in the south of the Province of Mendoza in Argentina near the city of Malargüe at an altitude of about 1300–1400 m. It combines two established techniques for ground based cosmic ray observation. Experiments with only one of these two techniques already supply important contributions to the understanding of cosmic

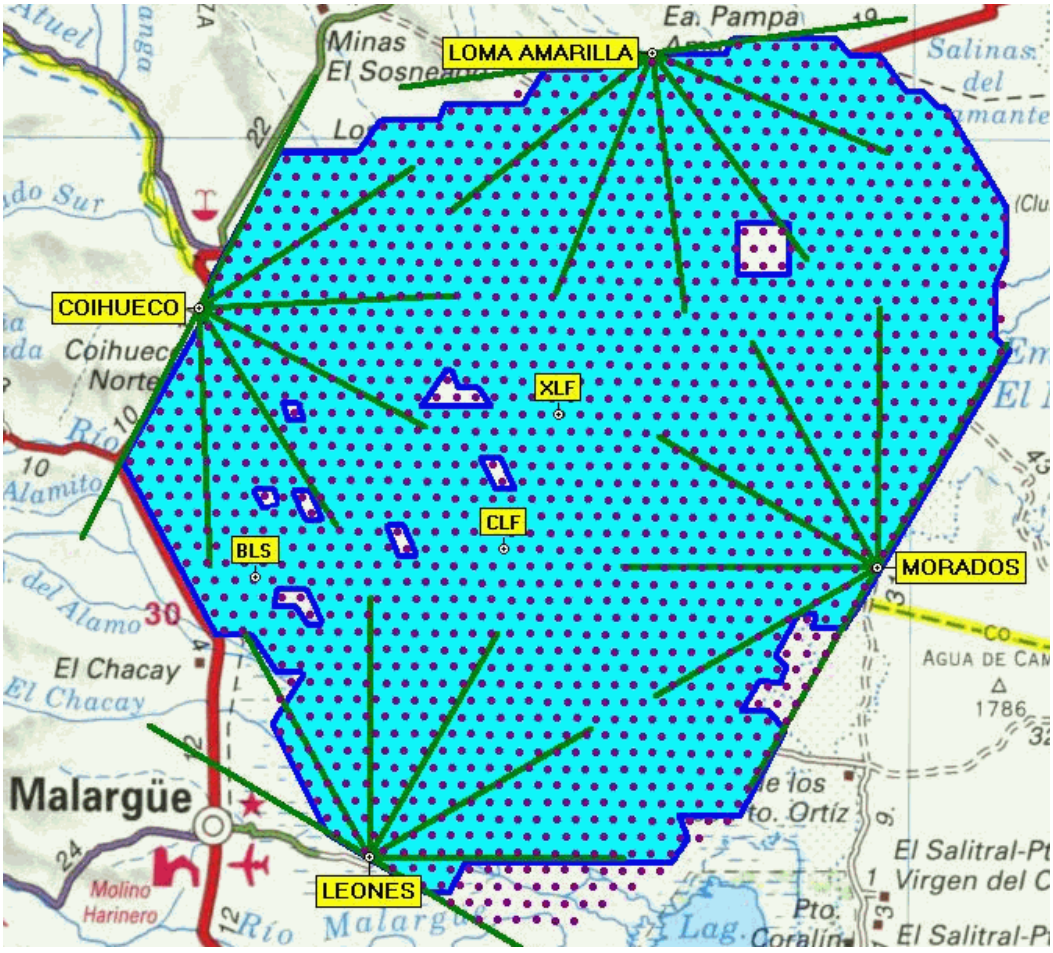

Figure 3.1: Map of the Pierre auger Observatory [108]. The area with the dots indicate the surface station. The position and field of view of the four fluorescence telescope sites Coihueco, Los Leones, Los Morados and Loma Amarilla as well as additional facilities are marked.

rays, but also introduced some controversies. These concerns let Jim Cronin and Allen Watson came up with a proposal in 1991 to construct the Pierre Auger Observatory which now combined the benefits of both techniques to start a hybrid era of air shower detection.

The first component is called 'surface detector' (SD) and consists of 1600 water Cherenkov stations arranged in an hexagonal grid with a station to station distance of 1.5 km covering an area of 3000 km^2 which is used to measure events with energies above $3 \cdot 10^{18}$ eV [110]. Additionally, a more dense grid with a 750 m spacing consisting of 60 stations is used which reduces the threshold for this part of the array to $3 \cdot 10^{17}$ eV [95]. The SD component measures the 'foot print' of an extensive air shower on the ground which is build up of secondary particles as described in Sec. 2.5. The advantage of the SD is the high amount of events gathered because of the large extension of the array and a theoretical duty cycle of 100%. But to get the energy estimation one has to rely on simulations that depend on extrapolations of hadronic interaction models which are subject to large uncertainties as already mentioned.

The second component, called the 'fluorescence detector' (FD) is built out of 24 telescopes positioned at four sites surrounding the area covered by the SD stations as can be seen in Fig. 3.1. The FD is able to measure the full longitudinal development of the air shower by the observation of the ultraviolet fluorescence light emitted by nitrogen molecules exited by the electrons of the air shower. The benefits are the absolute energy calibration and the direct measurement of the shower maximum that enables composition measurements as described in Sec. 3.3.2. However, the FD telescopes are only able to operate in clear moonless nights reducing the duty cycle to about 13 % of the total time of the experiment.

3.1 The Surface Detector

Each of the surface detector station is filled with 12 m^3 water and equipped with three PMTs. Charged particles with nearly the speed of light produce ultraviolet light due to the Cherenkov effect. Extensive air showers can be detected by a coincident signal in neighbouring SD stations. Only signals that triggered at least three stations within 100 μsec are used for further analysis. The timing difference is used to reconstruct the direction of the shower front and hence the shower axis which is perpendicular to the shower front. The stations have an autonomous power supply by solar panels and the data is communicated via radio connections as displayed in Fig. 3.2.

The energy of the surface detectors is calibrated by the FD energy by using air showers that are independently reconstructed by both detector components. For the energy estimator of the surface detector the signal at 1000 m distance to the shower core called S_{1000} is used. S_{1000} is proportional to the energy of the primary cosmic ray on top of the atmosphere. This property is nearly independent of the cosmic ray mass but depends on the zenith angle θ of the shower as this determines the amount of transversed atmosphere. To take this into account, the Constant Intensity Cut (CIC) method [111] is applied. The equivalent signal at median zenith angle of 38°

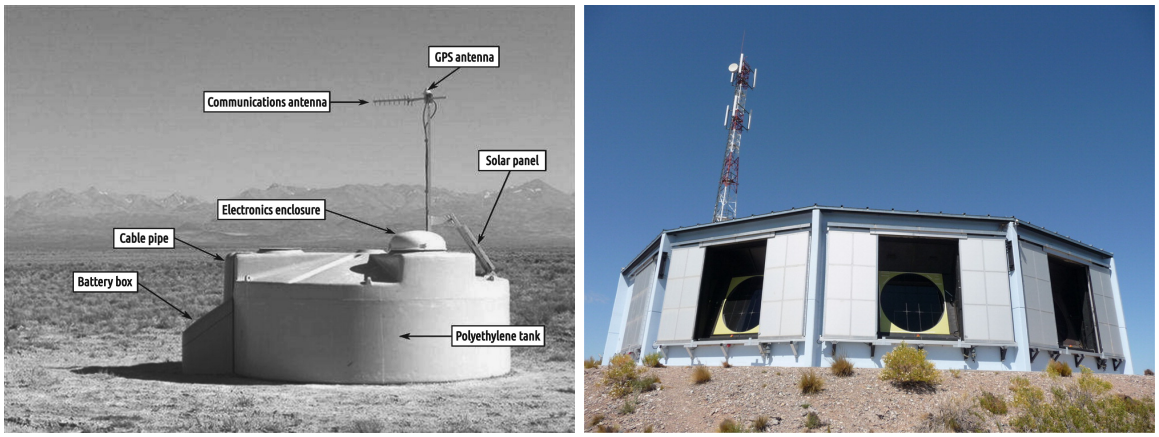

Figure 3.2: **Left:** Surface detector tank in the field with description of the main components [112]. **Right:** Fluorescence detector building containing six telescopes [112].

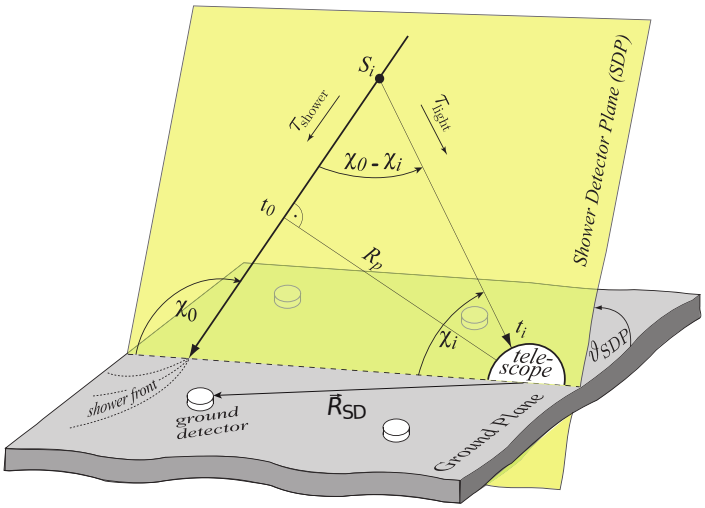

Figure 3.3: Sketch of the reconstruction of a hybrid shower with all relevant quantities [113].

(S_{38}) is finally used as an energy estimator. For the 750 m array the procedure is analogue with the difference that the signal at 450 m distance to the shower core and a median zenith angle of 35° are used instead. In case of the inclined events ($\theta > 60°$) the relative muon content of the signal N_{19} in respect to simulated proton showers at 10^{19} eV is used as the energy estimator.

3.2 The Fluorescence Telescopes

The camera of each of the 24 telescopes is equipped with 440 hexagonal photomultiplier tubes (PMT) with an opening angle of 1.5° enabling an imaging of the air shower. The derivation of the shower geometry needs at first a so called 'shower detector plane' which is fixed by the image of the shower axis in the telescope and the telescope position as displayed in Fig. 3.3. The air shower transverse the atmosphere with the speed of light which causes an increased angular speed $\dot{\chi}$ for near showers compared to more distant ones. The exact direction of the shower axis in the shower detector plane can be derived from geometrical considerations by finding the optimal angle χ_0 and nearest distance R_p for describing the measured timing and directional information of each illuminated pixel. With the information of the shower axis the signal can be corrected for attenuation in the atmosphere. This allows to convert the measured light signal into the number of air shower particles as function of the atmospheric depth X. The empirically formula found by Gaisser and Hillas [114]

$$N(X) = N_{\max}\left(\frac{X - X_0}{X_{\max} - X_0}\right)^{(X_{\max}-X)/\lambda} \cdot e^{(X_{\max}-X)/\lambda}$$

is fitted to the data. Here, $X_{\max}$ and $N_{\max}$ are atmospheric depth and the number of particles at the shower maximum. This allows to extract the shower maximum $X_{\max}$ and the total energy of the shower by the integral over the whole profile $E = \alpha \int N(X)dX = \int dX dE/dX$ with $\alpha \approx 2.2\,\mathrm{MeV\,g^{-1}\,cm^{-2}}$. The reconstruction is further improved by addition of the timing information of the SD station with the strongest signal which is then called hybrid reconstruction. These hybrid events have an angular resolution of 0.5° for $E > 3\,\mathrm{EeV}$. Only a selection of events that pass strict quality criteria are used in the individual analysis. Additionally, allowing only events with $\theta < 60°$ for $E > 10^{18}\,\mathrm{eV}$ prevent a bias in the event selection which would otherwise exist for different primary masses. To calculate the detector exposure for hybrid events the dependencies on energy, distance from telescope, atmosphere and data taking conditions have to be taken into account in the according simulations. Also the amount of energy which is carried away mostly by neutrinos and high-energy-muons and hence is not deposited in the atmosphere have to be taken into account. For primary nucleons and nuclei this ranges between $7 - 13.5\,\%$ at $10\,\mathrm{EeV}$. After correcting this effect an uncertainty of $1.5 - 3\,\%$ remains. Systematic uncertainties for the exposure range from $14\,\%$ at $10^{18}\,\mathrm{eV}$ to $< 6\,\%$ for $E > 10^{19}\,\mathrm{eV}$.

3.3 Data from the Pierre Auger Observatory

In the following some important results of the Pierre Auger Observatory which are used in this thesis are given and the associated analysis are described.

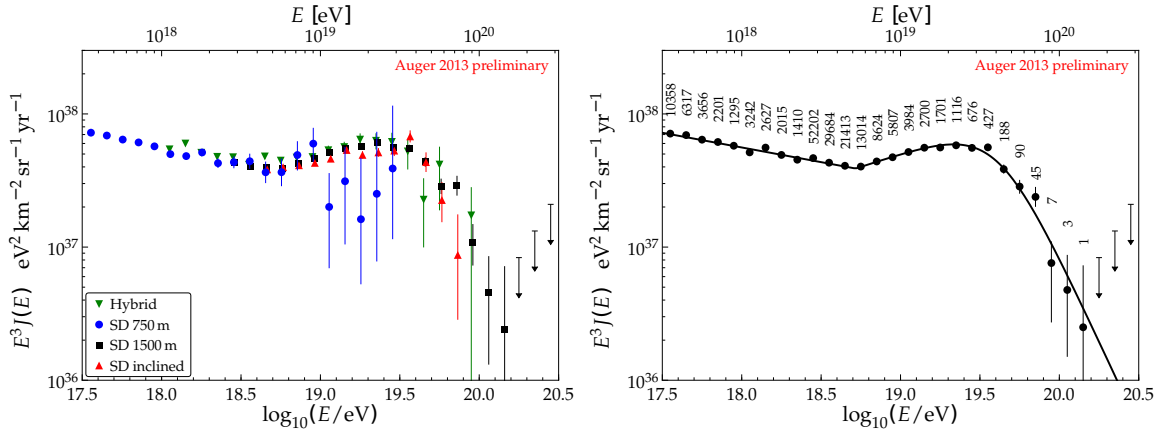

Figure 3.4: **Left:** Energy spectrum from various Auger analysis [95]. **Right:** Combined Auger energy spectrum with the fit of a broken power law [95].

3.3.1 Energy Spectrum Measured by the Pierre Auger Observatory

The energy spectrum [95] is obtained from four different analysis each specialised on a certain subset of events. Two of them are done with the 1500 m surface array using vertical events with $\theta < 60°$ or inclined events with $62° \leq \theta < 80°$. A further analysis uses data from the 750 m surface array taking into account only one zenith angle range of $\theta < 55°$. The forth analysis is done with hybrid events.

The energy resolution accounts for the 1500 m array for inclined showers from 15 % for energies below $6{\cdot}10^{18}$ eV to less than 12 % for energies above 10^{19} eV. In combination with the steep energy spectrum these uncertainties cause an alteration of the true energy spectrum due to bin-to-bin migration which is corrected accordingly. The uncertainties in the energy scale of 14 % stems from the FD measurements and is also valid for the SD data, as the absolute energy scale of the SD data is gained by as calibration with the FD data.

A combined energy spectrum is derived from the results of the four single spectra using data from 1 January 2004 to 31 December 2012. The 1500 m array spectrum has the largest exposure and hence dominates the energy spectrum. The hybrid and the 750 m array spectra make it possible to extend the 1500 m array spectrum down to $10^{17.5}$ eV and the inclined spectrum gives an independent measurement. To match the single spectra the absolute normalization of the individual fluxes is allowed to vary within the uncertainties of the individual exposures. This results in a 2 % up-scaling of the SD 750 m spectrum, 5 % up-scaling of the inclined spectrum and a 6 % down-scaling of the hybrid spectrum. The individual spectra are displayed in the left plot of Fig. 3.4. A broken power low with a smooth suppression at highest energies is fitted to the combined spectrum as can be seen in the right plot of Fig 3.4. A spectral index of $3.23 \pm 0.01(\text{stat.}) \pm 0.07(\text{sys.})$ and an ankle position at $\lg(E_a) = 18.72 \pm 0.01(\text{stat.}) \pm 0.02(\text{sys.})$ are extracted from this fit.

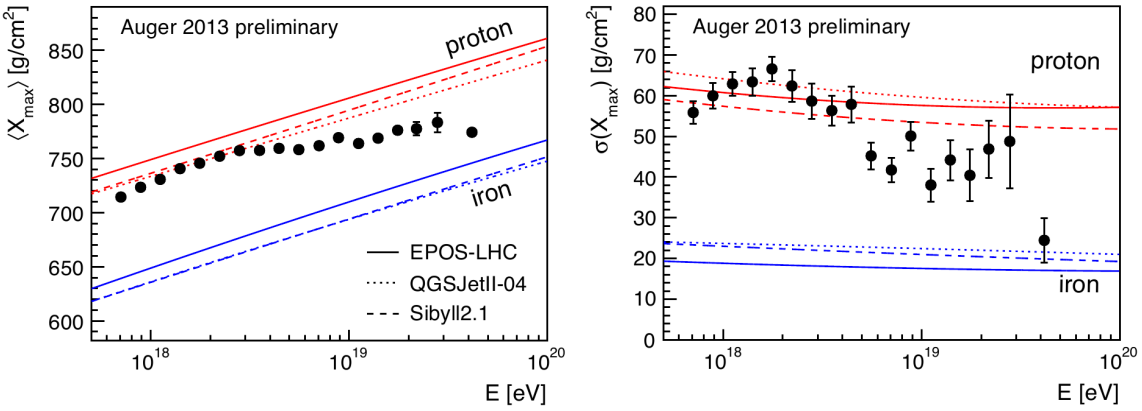

Figure 3.5: **Left:** $\langle X_{\max} \rangle$ in dependence of the energy. **Right:** $\sigma(X_{\max})$ in dependence of the energy [95].

3.3.2 Auger $X_{\max}$ Measurements

The average of the maximum of the shower development $\langle X_{\max} \rangle$ and the amplitude of the shower to shower fluctuations of $\sigma(X_{\max})$ are the main observables used by the Pierre Auger Observatory to measure the heaviness of the mass composition. Only data with statistical uncertainties of $X_{\max}$ below $40\,\mathrm{g/cm^2}$ are used in the analysis. Atmospheric variations are taken into account by excluding cloud contaminated events and using aerosols monitoring. A required profile fit quality of $\chi^2/ndf < 2.5$ additionally reduced residual clouds. A minimum energy of $10^{18}\,\mathrm{eV}$ is required to ensure full trigger efficiency for all primary masses. Events with light emission angle towards FD smaller than 20° are rejected as the apparent angular speed of the image in the telescope would otherwise reach the time scale of synchronization between FD and SD. Additionally, this cut removes events with a high Cherenkov contribution. The main part of the shower profile has to be inside the field of view of the the FD ($1.5° < \theta < 30°$) to avoid misreconstructions. Fiducial volume cuts guarantee that relevant $X_{\max}$ range is covered.

Data from 1st of January 2004 to the 31 December 2012 are used to derive the $\langle X_{\max} \rangle$ and $\sigma(X_{\max})$ distribution shown in Fig. 3.5.

3.3.3 Upper Limits for UHE-Photons with the Pierre Auger Observatory

In this section the separation of photon air showers from nucleon and nuclei air showers is described, as done by the Pierre Auger Observatory. Photons induce pure electromagnetic showers in which each interaction has a smaller multiplicity than hadronic interactions. Therefore, the shower undergo more interactions until the energy of the secondaries drops below the threshold for interaction as described in Sec. 2.5. Additionally, for photons with energies above $\sim 10\,\mathrm{EeV}$ the LPM effect [115, 116, 117]

suppresses the cross section. At these energies a very small longitudinal momentum transfer exists. This results in a pair production which occurs over long distances. Therefore, multiple scattering centres interfere destructively and cause reduction of the cross section. As a consequent a larger $X_{\max}$ for photon showers is given for high energies. Furthermore, the muon content of photon induced showers is much smaller because photo muon production and direct muon pair production are sub-dominant processes. The separation can be done according to these differences to showers from nucleons and nuclei with observations of the fluorescence detector as well as of the surface detectors.

Detection with the Surface Detector In the first analysis used at the Pierre Auger Observatory [43] only the surface detector was used relying on two observables that are sensitive to both described differences between air showers introduced by photons and nuclei.

The radius of curvature R of a spherical shower front uses the delay in the arrival time of particles at a certain lateral distance r with respect to the shower core position. Showers starting higher in the atmosphere and having a smaller $X_{\max}$, as expected for nuclei, results in smaller delays in time for fixed r. The muons can reach the ground also from higher in the atmosphere decreasing also the delay in arrival time for nuclei. The radius of curvature is derived from a fit of a curved shower front to measured trigger times $t_i(r_i)$ of the first particle registered at distance r_i.

The second observable is the rise time $t_{1/2}$ defined by the time the signal needs in a surface detector station to rise from 10% to 50% of the total signal. The signal at 1000 m distance on the line of projection of the shower axis on ground is used. For a smaller production hight, as expected for photons, an increased spread in time is expected. The increased muon content of nuclei air showers results in an additional decrease in the spread in arrival time for nuclei.

The energy estimator $S(1000)$ for photon showers can be a factor ≥ 2 below the value for showers induced by nuclei. The main reasons are smaller numbers of muons and a steeper ground lateral distribution caused by the later shower development. Because of this the energy scale for photons is derived from dedicated simulations. As pure electromagnetic interactions have to be taken into account in these simulation, the energy scale is largely independent from hadronic interaction models. Using simulation results delivers a poor energy resolution of 40%. A special energy conversion is applied for photons, using the universal behaviour of electromagnetic showers [118] which improves the energy resolution up to a value of $\sim 25\%$.

The selection of photon candidates is done with the following method. The whole data set undergoes different selection cuts to insure good reconstruction quality and high acceptance of the detector for photons. Data with energies ≥ 10 EeV and zenith angle in the range $30^\circ \leq \theta \leq 60^\circ$ are chosen, as they show the best photon reconstruction and detection efficiency. More inclined showers are not used due to more complex reconstruction algorithm required for these events.

Once the data set is selected, the deviation Δ_x of the two observables risetime $t_{1/2}$

and radius of curvature R from the mean of photon expectations in units of the spread of the observable for photons $\sigma_{x,\gamma}$ is calculated for each event. Then, $\bar{x}_\gamma$, $\sigma_{x,\gamma}$ and

$$\Delta_x = \frac{x - \bar{x}_\gamma(S(1000), \theta)}{\sigma_{x,\gamma}(S(1000), \theta)},$$

are derived by photon simulations. $\Delta_{t_{1/2}}$ and Δ_R are combined in a principal component analysis. 5% of the data and photon simulations are used to determine the principle component. The remaining 95% of the data are projected on the principal axis along with simulated photons. The cut is executed on this projected distribution at the mean for the simulated photons to obtain photon candidates. This introduces a cut efficiency of $f = 0.5$ by construction.

With data from 2004 to 2006 no candidates were found for the threshold energies of $E_{\mathrm{min}} = 10, 20, 40\,\mathrm{EeV}$. Upper limits on the photon flux

$$\Phi_\gamma^{CL}(E > E_{\mathrm{min}}) = \frac{\mathcal{N}_\gamma^{\mathrm{CL}}(E_\gamma \geq E_{\mathrm{min}}) \times \frac{1}{f} \times \frac{1}{\epsilon}}{0.95A}$$

and the photon fraction

$$\mathcal{F}_\gamma^{CL}(E > E_{\mathrm{min}}) = \frac{\mathcal{N}_\gamma^{\mathrm{CL}}(E_\gamma > E_{\mathrm{min}}) \times \frac{1}{f} \times \frac{1}{\epsilon}}{N_\gamma(E_\gamma > E_{\mathrm{min}}) + N_{\mathrm{non-}\gamma}(E_{\mathrm{non-}\gamma} > E_{\mathrm{min}})}$$

are calculated. $\mathcal{N}_\gamma^{\mathrm{CL}}$ is the upper limit on the number of photons at confidence level CL calculated from number of photon candidates N_γ using the Poisson distribution and ϵ the integrated efficiency of accepting photons. A is the exposure according to the used data set.

The resulting limits on the photon flux are $\Phi_\gamma^{0.95} = 3.8 \times 10^{-3}\,\mathrm{km^{-2}\,sr^{-1}\,yr^{-1}}$, $2.5 \times 10^{-3}\,\mathrm{km^{-2}\,sr^{-1}\,yr^{-1}}$, $2.2 \times 10^{-3}\,\mathrm{km^{-2}\,sr^{-1}\,yr^{-1}}$ and on the photon fraction $\mathcal{F}_\gamma^{0.95} = 2.0\,\%, 5.1\,\%, 31\,\%$ at 95 % confidence level and the energy thresholds $E_{\mathrm{min}} = 10, 20, 40\,\mathrm{EeV}$, respectively. These limits are displayed with black arrows in Fig. 3.6.

Hybrid Detection In a second analysis [119], hybrid data is used to search for UHECR photons. The direct information of the longitudinal development of air showers obtained from the fluorescence telescopes allows to decrease the energy threshold for the analysis below 10 EeV. The increased cosmic ray flux at lower energy nearly balance out the lower exposure of hybrid data due the factor of ~ 10 reduced duty cycle. Again the energy scale for photons deviates from nucleons and nuclei as only a missing energy of 1 % is expected for photon showers, which causes a decrease of the photon energy. This behaviour is contrary to that observed for SD only data. Data taking during the presence of clouds have to be removed as the clouds can significantly alter the reconstruction of events. As a full automatic processing is not available till now, only the final photon candidates are checked for clouds by hand. The efficiency ϵ_{clc} of passing the cloud cut is determined for data above $E_\gamma = 10\,\mathrm{EeV}$ yielding $\epsilon_{\mathrm{clc}} = 0.51$. To distinguish photon candidates, a cut on the X_{max} distribution is applied. Events have to be above the median of the X_{max} distribution for

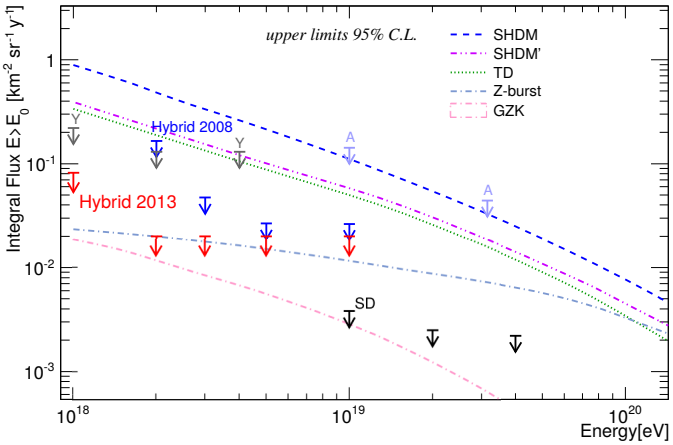

Figure 3.6: Upper limits on the photon flux slightly modified from [119].

photons from simulations $X_{\max}^{\gamma,\mathrm{med}}$ concerning the dedicated energies and direction. A number of $n_{\gamma\text{-cand}} = 8, 1, 0, 0$ photon candidates were found for the energy thresholds $E_{\min} = 2, 3, 5, 10\,\mathrm{EeV}$, respectively. Simulations with nucleons and different nuclei show that the found photon candidates are well within the expectations from these backgrounds.

The upper limit on the photon fraction is calculated using

$$\mathcal{F}_{\gamma}^{CL}(E > E_{\min}) = \frac{n^{\mathrm{CL}}_{\gamma-\mathrm{cand,obs}}(E_{\gamma} > E_{\min}) \times \frac{1}{\epsilon_{\mathrm{fvc}}} \times \frac{1}{\epsilon_{\mathrm{pcc}}}}{n_{\mathrm{total}}(E_{\gamma} > E_{\min}) \times \epsilon_{\mathrm{clc}}}.$$

The upper limit $n^{95}_{\gamma\text{-cand,obs}}$ is calculated from $n_{\gamma\text{-}cand}$. Here ϵ_{fvc} and ϵ_{pcc} are the photon reconstruction efficiencies for the fiducial volume cuts and the photon candidate cut, respectively. For the total number of events also the photon energy is assumed. This can be regarded as a conservative estimation leading to a reduced number of total events.

The resulting upper limit of the photon fraction for data from 1 st of December 2004 till 31 st of December 2007 are $\mathcal{F}_{\gamma}^{95} = 3.8\,\%, 2.4\,\%, 3.5\,\%$ and $11.7\,\%$ above $E_{\gamma} = 2, 3, 5$ and $10\,\mathrm{EeV}$ at $95\,\%$ confidence level. The corresponding upper limits for the photon flux are shown as blue arrows in Fig. 3.6.

Combined Detection with Surface and Hybrid Data In a further publication [44] of the Pierre Auger collaboration a photon search is performed using a combination of the fluorescence detector observable $X_{\max}$ and the surface detector observable S_b. Additionally, the energy threshold is extended down to 1 EeV. S_b is defined as

$$S_b = \sum i, S_i \left(\frac{R_i}{R_{\mathrm{ref}}}\right)^b$$

where the sum runs over all stations in the events. S_i is the signal hight at station i and R_i the corresponding distance to the reconstructed hybrid shower axis. R_{ref}

is a reference distance set to 1000 m and the parameter b is set to 4 yielding the optimized separation power between photons and hadrons. The classification of photon candidates is obtained performing a Fisher analysis. The analysis is trained with simulated photon and proton induced showers where the latter are taken as background events. The photon candidate cut is applied to the Fisher response at 50 % of the photon events. Finally 6, 0, 0, 0 and 0 candidates are found above 1, 2, 3, 5 and 10 EeV using the data collected from January 2005 to September 2010. A check with simulated showers show consistency of the number of candidates with expectations from nuclear primaries. Upper limits of the photon flux are calculated with

$$\Phi_{\gamma}^{95CL}(E > E_{\mathrm{min}}) = \frac{\mathcal{N}_{\gamma}^{\mathrm{CL}}(E_{\gamma} \geq E_{\mathrm{min}})}{\mathcal{E}_{\gamma,\mathrm{min}}}.$$

$\mathcal{N}_{\gamma}^{\mathrm{CL}}$ being again the number of photon candidates at confidence level CL and $\mathcal{E}_{\gamma,\mathrm{min}}$ the minimum hybrid exposure for photons after the photon candidate cut.

This exposure is obtained by shower and detector simulations with photons as primary particles. The results are smoothed with a gamma function to reduce the impact of statistical fluctuations. The upper limit on the photon flux are $8.2{\cdot}10^{-2}\mathrm{km}^{-2}\mathrm{sr}^{-1}\mathrm{yr}^{-1}$ for $E_{\gamma} \geq 1\,\mathrm{EeV}$ and $2.0 \cdot 10^{-2}\mathrm{km}^{-2}\mathrm{sr}^{-1}\mathrm{yr}^{-1}$ for $E_{\gamma} \geq 2, 3, 5$, and 10 EeV as displayed with red arrows in Fig. 3.6. The derived limits to the photon fraction are $0.4\,\%, 0.5\,\%, 1\,\%, 2.6\,\%$ and $8.9\,\%$ above $1, 2, 3, 5$ and 10 EeV.

3.3.4 Upper Limits for UHE-Neutrinos with the Pierre Auger Observatory

The surface detector of the Pierre Auger Observatory is used for the search of UHE-neutrinos in three analysis using data from different bins in the zenith angle θ which allows to optimize the identification criteria in each range for the best neutrino discrimination.

Neutrinos interacting in the Earth crust, the so called 'upward going' or 'Earth-skimming' (ES) neutrinos refer to $90° \leq \theta \leq 95°$. Although only a narrow angular range is observed for this subset, it can benefit from lower background. Only tau neutrinos and charge current interactions are possible.

In addition the two angular bins $75° \leq \theta \leq 90°$ and $60° \leq \theta \leq 75°$ are chosen to select events that transverse a large amount of atmosphere named 'downward-going high angle' (DGH) and 'downward going low angel' (DGL) selection, respectively. For both sets detection of all neutrino flavours with charged current and neutral current interactions are possible. These analyses can use broader angular ranges but have a higher background.

In all three cases the basic concept is, that neutrinos due to their small cross section can interact late in the atmosphere or even in the Earth crust. Nucleons, nuclei and photons on the other hand interact at the beginning of the atmosphere. Hence, selecting only young showers prefer showers induced by neutrinos.

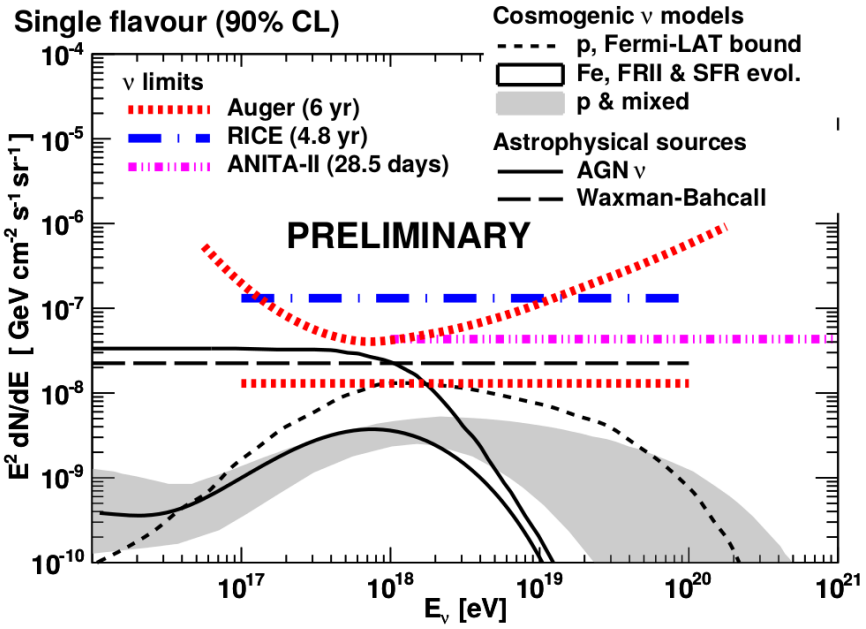

Figure 3.7: Upper limits on the neutrino flux given by the Pierre Auger collaboration [95].

For the ES and DGH multiple criteria are used to determine inclined showers. The elongation of the shape of the shower pattern on the ground is measured by the ratio L/W with L the length and W the with of the pattern. A higher elongation corresponds to a more inclined shower. Also the average apparent speed $\langle V \rangle$ over all pairs of stations in the event is used. It should peak at the speed of light c for very inclined showers and have a low root mean square. For the DGH events in addition and for the DGL solely a further quality cut is applied directly to the reconstructed zenith angle.

Showers in the first stage of development have a large time spread of the particles in the shower front in the order of $\sim 1\,\mu s$. In contrast to this, old showers are dominated by high energy myons yielding a small spread in arrival time. The main observables to measure this time behaviour is the time of the signal above a certain threshold value also (ToT) and the ratio of the signal area over the peak value (AoP) for all the three data selections. For the ES analysis a cut is applied to these variables. In the DGH and DGL selection a linear Fisher-discrimination polynomial based on the AoP and other variables constructed from AoP is used for the discrimination.

The selection criteria are optimized on a small subset of the data where it is assumed that in general dominating part is made of background events. Applying the analysis on the data recorded between January 2004 and 31 th December 2012 yield no neutrino candidate. Consequently, three distinctive upper limits on the neutrino flux are placed assuming a neutrino flavour ratio of 1:1:1 as expected from neutrino oscillations. The differential neutrino flux is set to $\frac{dN}{dE}(E_\nu) = kE_\nu^{-2}$.

To improve the final upper limit, a combined exposure $\mathcal{E}_{\text{tot}}$ is calculated by Monte

Carlo simulations demanding the pass of at least one of the three selection criteria for each event to be counted as a neutrino.

The upper limit on the value k is given as

$$k = \frac{N_{up}}{\int_{E_{\min}}^{E_{\max}} E_\nu^{-2} \mathcal{E}_{\mathrm{tot}}(E_\nu)\, dE_\nu}.$$

The upper limit on the signal events N_{up} is obtained using a semi Bayesian extension [120] of the Feldman-Cousins [121] approach to include the uncertainties in the exposure. This departs from the nominal value for zero candidates and no expected background.

The final single-flavour limit with 90 % confidence level is

$$k_{90} < 1.3 \cdot 10^{-8} \mathrm{GeV cm^{-1} s^{-1} sr^{-1}}$$

for the energy interval $\sim 1.0 \cdot 10^{17}\,\mathrm{eV}\ -1.0 \cdot 10^{20}\,\mathrm{eV}$. In addition also the limits are given for different bins of width 0.5 in $\log_{10} E_\nu$, both are shown in Fig. 3.7.

3.3.5 Search for Anisotropies in the Arrival Directions of UHECRs

Correlation of UHECR Events with Near AGN Positions

The correlation of the arrival directions of the highest energetic events with $E > 40\,\mathrm{EeV}$ measured by the Pierre Auger Observatory with the AGN positions in the 12^{th} edition of the catalogue of quasars and active nuclei by Véron-Cetty and Véron [122] is analysed in [123, 124].

The probability that k or more out of N events with isotropic arrival directions correlate within an angular distance of ϕ degree is given by

$$P = \sum_{j=k}^{N} \binom{N}{j} p^j (1-p)^{N-j}. \tag{3.1}$$

Here p is the probability of one event to correlate with an AGN position within ϕ degrees by chance. This probability is given by the fraction of the sky covered by the solid angles around the catalogue positions given by ϕ and weighted by the directional exposure. It should be mentioned here, that the catalogue can not be seen as complete or an unbiased statistical sample of AGN. In particular, the region around the galactic centre is partly incomplete. However, this is not crucial to prove the existence of anisotropy.

In this analysis the dependencies of the correlation on the maximum redshift $z_{\max}$ of the AGNs, the maximum angular separation ϕ and the threshold energy E_{th} for the cosmic rays are considered. The probability P from Eq. 3.1 was minimized by doing an exploratory scan in the three parameters $z_{\max}$, ϕ and E_{th} with data from 1 January 2004 to 27 May 2006. The minimum was found for $z_{\max} = 0.018\,(D_{\max} = 75\,\mathrm{Mpc})$,

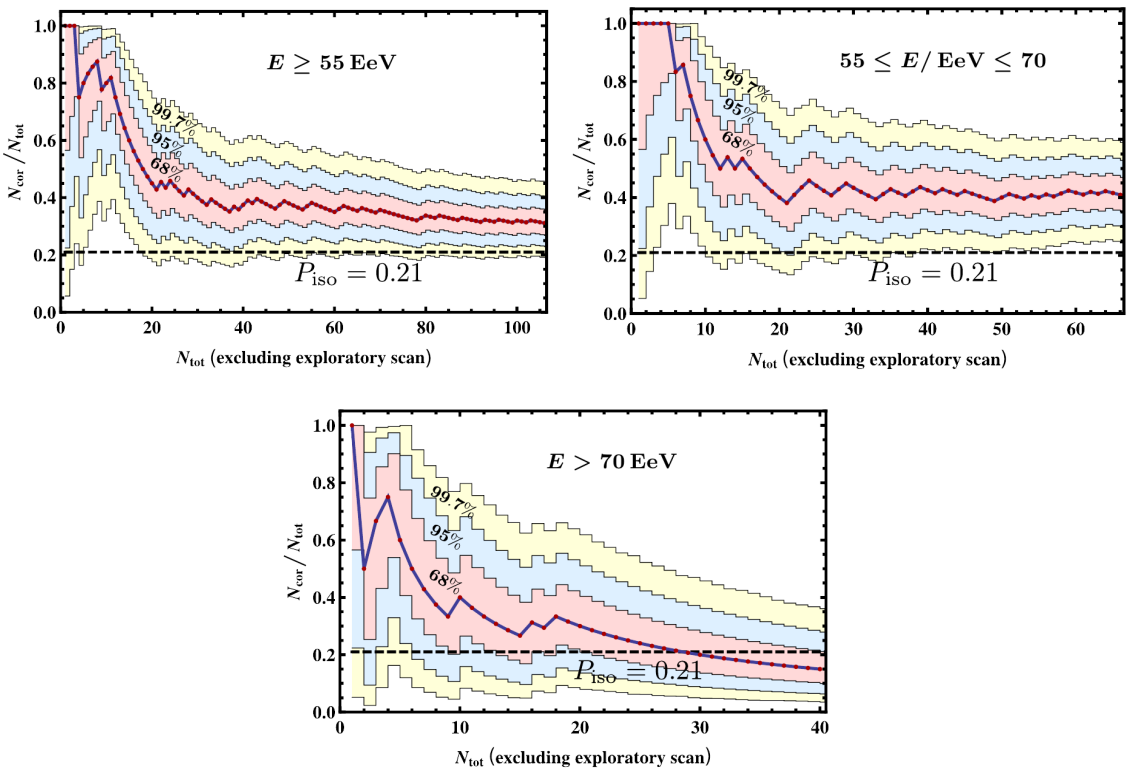

Figure 3.8: Evolution of the fraction of events measured by the Pierre Auger Observatory that correlate with the positions of AGN from the Véron-Cetty and Véron catalog [122] for the following energy ranges. **Top left:** $E \geq 55\,EeV$ **Top right:** $55\,EeV \leq E \leq 70\,EeV$. **Bottom row:** $E > 70\,EeV$ [125].

$E_{\mathrm{th}} = 56\,\mathrm{EeV}$ and $\phi = 3.1°$ having 12 correlations with at least one AGN out of 15 events. To evaluate the chance probability of such a correlation to happen for an isotropic distribution of events was derived with sets of simulated isotropic arrival directions with the same number as the exploratory scan. The fraction of sets that have an equal or lower value than the result of the minimization P_{min} estimates the chance probability of such a correlation not to happen for an isotropic distribution of arrival directions.

In case of an anisotropic signal, the reduction of the statistical significance of this signal due to the trail factor has to be determined. For this reason a test was performed on an independent data set observed after 27 May 2006 where the selection criteria and correlation parameters were fixed by the exploratory scan. As it is not known how many events are required to confirm the statistical significance before hand, a running prescription was applied after each new event passing the selection criteria. After this criterion was satisfied, the hypothesis of isotropy could be rejected with 99 % confidence level. The minimum number of correlations k_{min} out of N independent events were reached on 25 May 2007 with $k = 6$ and $N = 8$.

Alternatively, a sequential likelihood ratio test was done to monitor the evolution of

the correlation signal. A likelihood ratio R defined by Wald [126, 127] was calculated for every new event. The reaching of $R \geq 95$ is demanded in this test to reject the hypothesis of isotropy which was achieved after 10 events out of which 7 correlated.

The here used catalogue is expected to be increasingly incomplete towards the galactic plane due to absorption of light. Also cosmic rays should be more deflected in galactic magnetic fields from this direction than from higher galactic latitudes. Consequently, events near the galactic plane ($|b| > 12°$) are excluded in the scan. Here the minimum probability $P_{\min}$ occur for the same parameter and the strength of the correlation improved.

The correlation with AGN from the VCV-catalogue do not necessarily imply that AGN have to be the sources of UHECR. The AGN are a tracer of the strongly non-uniform matter distribution in our local universe. For this reason a catalog of all galaxies, different galaxy cluster surveys and a catalog of star burst galaxies are tested. No significant correlation was found in this searches.

In [125] an update of the correlation fraction showed weakening of the signal with time as can be seen in the upper left plot in Fig. 3.8. In the data up to 30 November 2012 33 events out of 106 above 55 EeV correlated with AGN yielding in a correlation fraction of 31^{+5}_{-4} %. The energy threshold is lowered from 56 EeV to 55 EeV due to a change in the absolute energy calibration. A consideration of the correlation signal in different energy intervals indicates that the departure from isotropy mainly arises for energies between 55 EeV and 70 EeV and decreases for higher and lower energies as displayed in the upper right and lower plot in Fig. 3.8.

The data is also checked with the 2MASS [128] and the Swift-BAT [129] catalogue by using two different methods in [124]. At first the cross correlation of events with nearby extragalactic objects from these two catalogues are considered. In both cases correlations in excess above isotropic expectations are observed. In addition a likelihood test with smoothed density maps derived from both catalogues is performed in [124] and [125]. The log-likelihood analysis yields a high isotropic fraction in the data which could imply an incompleteness of the catalogues. Here the 2MASS catalogue yields a smaller isotropic fraction than the Swift-BAT. With a smoothing angle of $\sigma < 1.4°$ for both catalogues a small scale correlation is found for the anisotropic part of the data.

Further Anisotropy searches by the Auger Observatory

In addition, also a number of catalogue independent analyses are performed by the Pierre Auger Collaboration to search for anisotropies in the arrival direction of cosmic rays. The clustering of events are investigated in [124, 130] using different autocorrelation functions and testing a range of separation angles defining the scale of the clustering. In another approach, energy dependant patterns are investigated using dedicated observables [131, 132]. In all these studies no significant evidence for a departure from the isotropic expectation were found.

In addition a search for anisotropies in the large angular scale distribution of the arrival direction of cosmic rays for E > 4 EeV is performed in [133, 95, 134]. The largest

departure from isotropy is observed for events with E$>$ 8 EeV with an amplitude for the first harmonic in right ascension of $r_1^\alpha = (4.4 \pm 1.0) \cdot 10^{-2}$ that has a chance probability of $P(\geq r_1^\alpha = 6.4 \cdot 10^{-5})$.

4 CRPropa

As described before, the energy spectra, the composition and the arrival directions of ultra high energy cosmic rays observed at Earth, are strongly influenced by effects on their way from sources. For a better understanding of these effects it is necessary to perform holistic simulations of all the relevant processes. CRPropa is a publicly available numerical tool that was created by Eric Armengaud et al. [135] for this purpose and was extended by Kampert et al. [2] to enable nuclei propagation. It is capable of propagating nuclei with mass numbers from proton to iron and the secondary electromagnetic cascades and neutrinos produced during the cosmic ray propagation.

4.1 General Capabilities of CRPropa

Pair production by nucleons on the photon background radiation is treated as a continuous energy loss for the protons using the parametrization derived by [136, 137]. For nuclei, a scaling of the energy loss is applied and the energy distribution of the produced electron-positron-pairs is calculated according to the parametrization given by [138]. For photo-pion production the SOPHIA event generator [139], which employs particle production cross sections measured at particle accelerators is used. SOPHIA determines the energy and type of the stable particles generated in the whole interaction. In case of nuclei the pion production cross section is approximated by considering the nucleus as a superposition of protons and neutrons as the nuclear binding energies are small compared to the energy of the nucleus. Here also a scaling is applied to take into account shielding effects in the nucleus. Different approximations are discussed in Sec. 4.2 by their impact on the cross section and the interaction length. In addition, all necessary interactions for the photodisintegration of nuclei as described in Sec. 2.4 are included. For the GDR and the QD processes, 287 cross sections are calculated in the energy range $1\,\mathrm{keV} \leq E_\gamma \leq 250\,\mathrm{MeV}$ from the TALYS framework [140] version 1.0 for $A \geq 12$. For lower mass numbers TALYS does not supply reliable results. For these nuclei the cross sections are taken from other sources as described in [141]. In this thesis mainly cross sections from the current version TALYS 1.6 are used instead the TALYS 1.0 unless it is mentioned otherwise.

The tracking of secondaries, namely electrons, positrons, photons and neutrinos is possible. Neutrinos propagate in straight lines without any energy loss except the adiabatic one. The other three particle types interact on their way with the low energy photon background and therefore evolve through an electromagnetic cascade, which is calculated with the DINT [142] package. Here all relevant interactions are taken in account. These are pair production, double pair production, triplet pair production

and inverse Compton scattering. In the presence of extragalactic magnetic fields also synchrotron losses of electrons and positrons are included and the electromagnetic cascades resulting from the synchrotron-photons are also followed. Because of the deflections of the charged components of the electromagnetic cascade in the magnetic fields, the 1-dimensional treatment of them is only an approximation. But as shown in [143], the deflection can be neglected. The propagation of photons require a special treatment in CRPropa to handle the calculation effort of the electromagnetic cascades. The redshift range of the simulation is binned and all photons and electron-positron pairs produced within one bin are collectively stored and propagate at once at the end of the simulation.

The most important low-energy photon background for the here regarded interactions is the CMB. But also the infrared background and the universal radio background influence the cosmic ray propagation. Because the density distribution of these two backgrounds are not exactly known, there are three different models of each of them implemented in CRPropa.

The simulation can be run in two different modes. In a 1d-mode all particles follow a straight path from the source to the observer. The individual effects of the expansion of the universe as described in Sec. 2.4.4 can be taken into account in this mode. For the evolution of the photon background in the infrared regime an additional scaling with z is possible that takes into account the creation of these photons during the galaxy formation processes. Here, a model from Kneiske et al. [2] is implemented. This is still an approximation as variation of the spectral shape of the photon background with z is not accounted for. Furthermore, an evolution of the source luminosity, as described in Sec. 2.1.6, can be specified in the 1d-mode. Obviously, in this 1d mode no deflections in magnetic field are considered.

In the 3d case particles propagate in a 'simulation box' with periodic boundary conditions. That means that whenever a particle reaches a boundary surface of the simulation box it re-enters again from the opposite surface. In this mode different magnetic fields can be implemented inside the box which are then used to calculate the deflections. Cosmological effects can not be taken into account in the 3d mode as the travel distance can not be determined beforehand. Cosmic rays in CRPropa can originate continuously in a region of space as well as from point sources. The energy can be set to a discrete value or follow a power law distribution.

Two different storage modes are provided where in 'full trajectories' coordinates and other properties of the nucleons are stored in every time step and in 'events' only the data for particles arriving at an observer is saved. In the 3d-mode, the surface of a sphere around the point of the observer is used as the detection area. This of course introduces an uncertainty in the arrival direction. Hence, the radius of this sphere has to be adjusted to ensure a required precision as well as a sufficient amount of detections. For secondaries only the event storing is available. In case of the electromagnetic cascade, the energy spectrum from 10^{24} eV down to 10^{7} eV is stored with a logarithmic energy binning.

4.2 Study of the Pion Production

The calculation of the pion production cross section as a superposition of nucleons is necessary as data on photo pion production cross sections are only available for some nuclei and only for a part of the energy range relevant for UHE cosmic ray propagation. Simulations of the cross section using nuclear transport models as for example done by [144] do not show good agreement with data for all cases.

Here, two approximations are compared with the simple nucleon superposition and the quality of this approximations is reviewed by comparing with data for the pion production cross section measured for nuclei. The simple superposition of the photo pion cross section for protons σ_{p} and neutrons σ_{n} is given by

$$\sigma_{A,Z}(E) = [Z\sigma_{\mathrm{p}}(E/A) + (A-Z)\sigma_{\mathrm{n}}(E/A)]. \tag{4.1}$$

To improve the accuracy in the first resonance region the following scaling of the above superposition is applied

$$\sigma_{A,Z}(E) = 0.85 \cdot [Z^{\xi}\sigma_{\mathrm{p}}(E/A) + (A-Z)^{\xi}\sigma_{\mathrm{n}}(E/A)], \tag{4.2}$$

with $\xi = 2/3$ for $A \leq 8$ and $\xi = 1$ for $A > 8$ as inspired by [145]. This approximation is used in the simulations throughout this thesis. In another ansatz a superposition of deuteron cross section (σ_d) is proposed for example by [146, 147] for a better description of the data in the resonance region as well. The cross section of a nucleus is given here by

$$\sigma_{A,Z}(E) = A/2 \cdot \sigma_{\mathrm{d}}(2E/A).$$

The two introduced nucleon superpositions are plotted for the nuclei He, Li, C and Al in the left column of Fig. 4.1 using the cross sections for nucleons from the SOPHIA code [139] which is in good agreement with data. The comparison of the data available for this nuclei from [148, 149, 150] shows a bad agreement especially for lighter nuclei. The simple nucleon superposition delivers an overestimation of the resonance region whereas the scaled one shows a better fit to the resonance region but in general underestimates the data.

In addition, the deuteron superposition is plotted for the nuclei He, Li, C and Al in the right column of Fig. 4.1 by taking the deuteron cross section from the data of [148]. Again, comparing with the data for the cross sections of the nuclei a better agreement is shown for the deuteron superposition in particular for the light nuclei Helium and Lithium. Hence, the deuteron superposition will be taken as the best approximation, although no perfect agreement is achieved.

To see the impact of the differences in the cross sections on the cosmic ray propagation the interaction rates have to be calculated. Therefore, a convolution of the cross section with the low energy photon background is needed. This is done by the following integral which is derived for example in [141]

$$\lambda^{-1} = \frac{1}{2\gamma^2\beta}\int_0^{\infty}\frac{n(E_\gamma)}{E_\gamma^2}\left\{\int_{\gamma E_\gamma(1-\beta)}^{\gamma E_\gamma(1+\beta)} E'_\gamma\sigma(E'_\gamma)\mathrm{d}E'_\gamma\right\}\mathrm{d}E_\gamma. \tag{4.3}$$

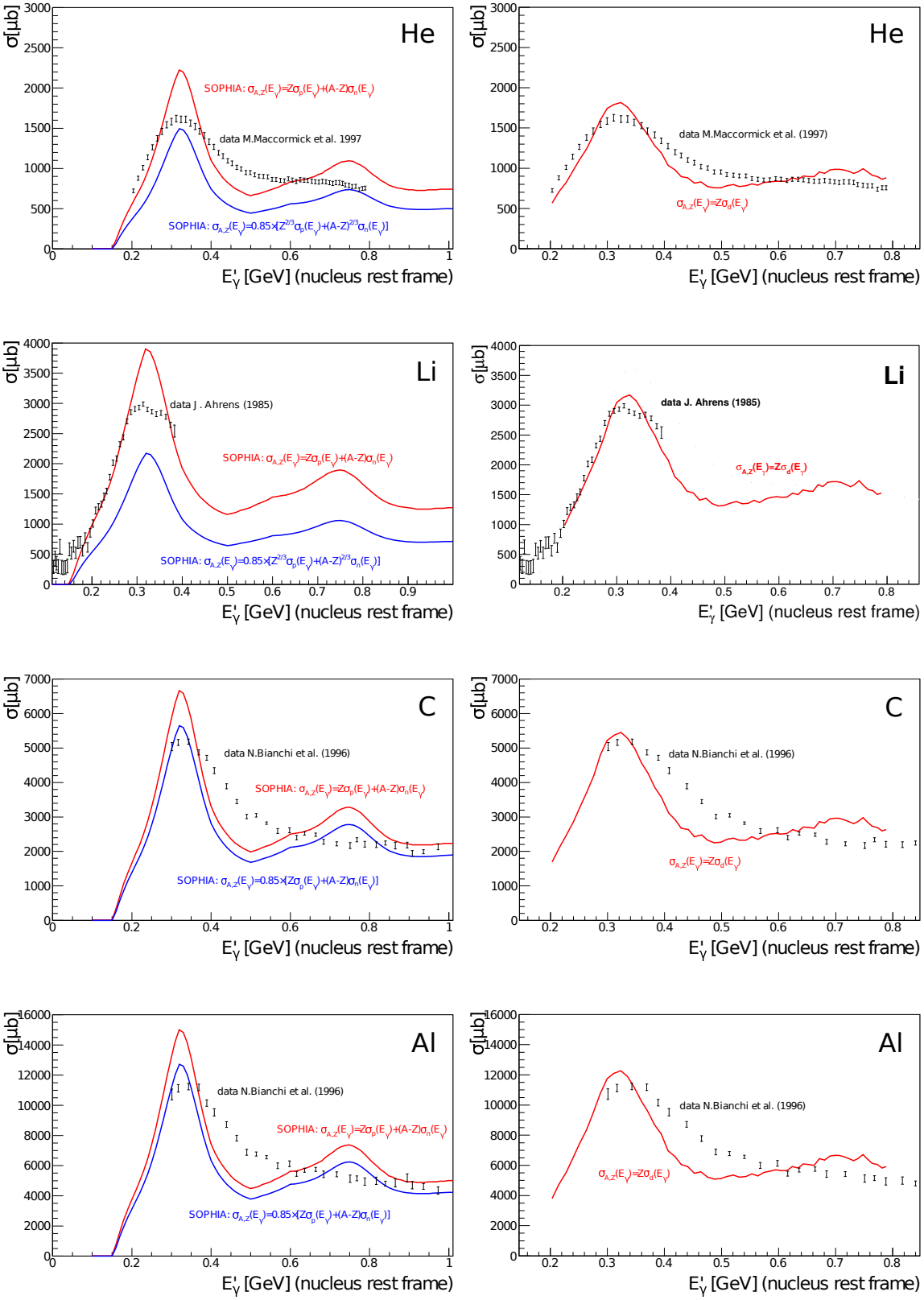

Figure 4.1: **Left column:** Cross section for photo pion production on nuclei from two different superpositions of nucleon cross sections as described in the text are displayed as red and blue lines along with data points by [148, 149, 150]. The nuclei of He, Li, C and Al are shown from top to bottom. **Right column:** Same as the left column but the red line shows the deuteron superposition as specified in the text.

Assuming $\beta = 1$ one obtains

$$\lambda^{-1} = \frac{1}{2\gamma^2} \int_0^\infty \frac{n(E_\gamma)\mathrm{d}x}{E_\gamma^2} \left\{ \int_0^{E'_\gamma = 2\gamma E_\gamma} E'_\gamma \sigma(E'_\gamma)\mathrm{d}E'_\gamma \right\} \mathrm{d}E_\gamma \tag{4.4}$$

Here, E_γ is the photon energy in the lab frame, E'_γ the photon energy in the nucleus rest frame, $\beta = v/c$ the velocity of the cosmic ray in units of the speed of light and $\gamma = E_{\mathrm{nucleus}}/M$ the Lorentz factor. The pion production cross section is needed for this calculation in the energy range $E'_\gamma \in [0.155, 2000]\,\mathrm{GeV}$. The lower border is motivated by the steep decrease of the cross section for the lowest energies allowing to neglect the cross section for lower energies. In addition, the photodisintegration will be dominant below this energy. The higher border can be derived from Eq. 4.4 assuming the relevant energy range of the photon background of $4 \cdot 10^{-10}$–$10^{-2}\,\mathrm{eV}$ for CMB and 10^{-3}–$10^{2}\,\mathrm{eV}$ for IR background the maximum gamma factor of $10^{14}\,\mathrm{eV}$ as used in CRPropa. This gamma factor allows to take into account for example cosmic ray proton with $\sim 10^{23}\,\mathrm{eV}$ in the lab frame. For deuterons, data are available for $E'_\gamma \in [0.204, 10.12]\,\mathrm{GeV}$ [148, 149]. The needed energy ranges below and above the data region are taken from the simple nucleon superposition and this combination will be taken for the calculation of the cross section denoted as deuteron superposition. Besides the resonance regions this superposition seems to be in good agreement with the deuteron cross section for the overlapping energy ranges as can be seen in the top plot in Fig. 4.2. In particular, at the higher energies the scaled nucleon superposition seems to deviate from the data. The interaction rate for the pion production for He and C nuclei are displayed in the top row of Fig. 4.3 calculated with the cross section from the deuteron superposition and the two nucleon superpositions. The plot in the bottom row of Fig. 4.3 show that compared to the interaction rate from the deuteron superposition the simple nucleon superposition causes an increase of up to $\sim 10\,\%$ whereas the scaled nucleon superposition causes an decrease of more than $30\,\%$ for He and up to $\sim 15\,\%$ for C nuclei. Hence, the simple nucleon superposition seems to introduce only a minor inaccuracy compared to the deuteron superposition, whereas the scaled nucleon superposition deviates stronger in particular for light nuclei. Regarding the minor importance of the the photo pion production in the nuclei propagation the small deviations found in this study can be neglected.

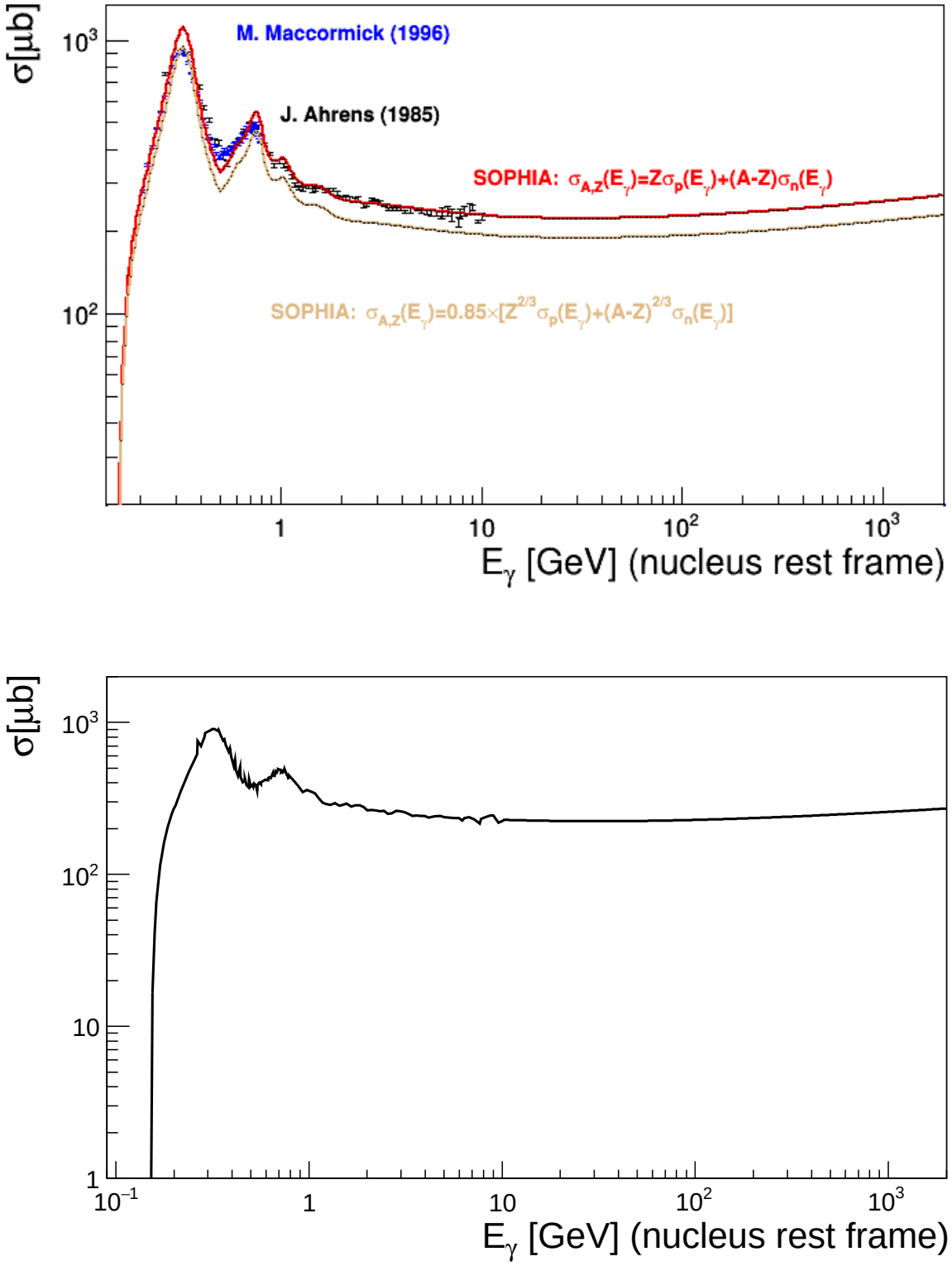

Figure 4.2: **Top:** Deuteron cross section from [148, 149] compared to two different approximations of the deuteron cross section by nucleon superpositions. The proton and neutron cross sections are taken from the SOPHIA generator [139]. **Bottom:** Combination of the cross section from the deuteron data and the nucleon superposition.

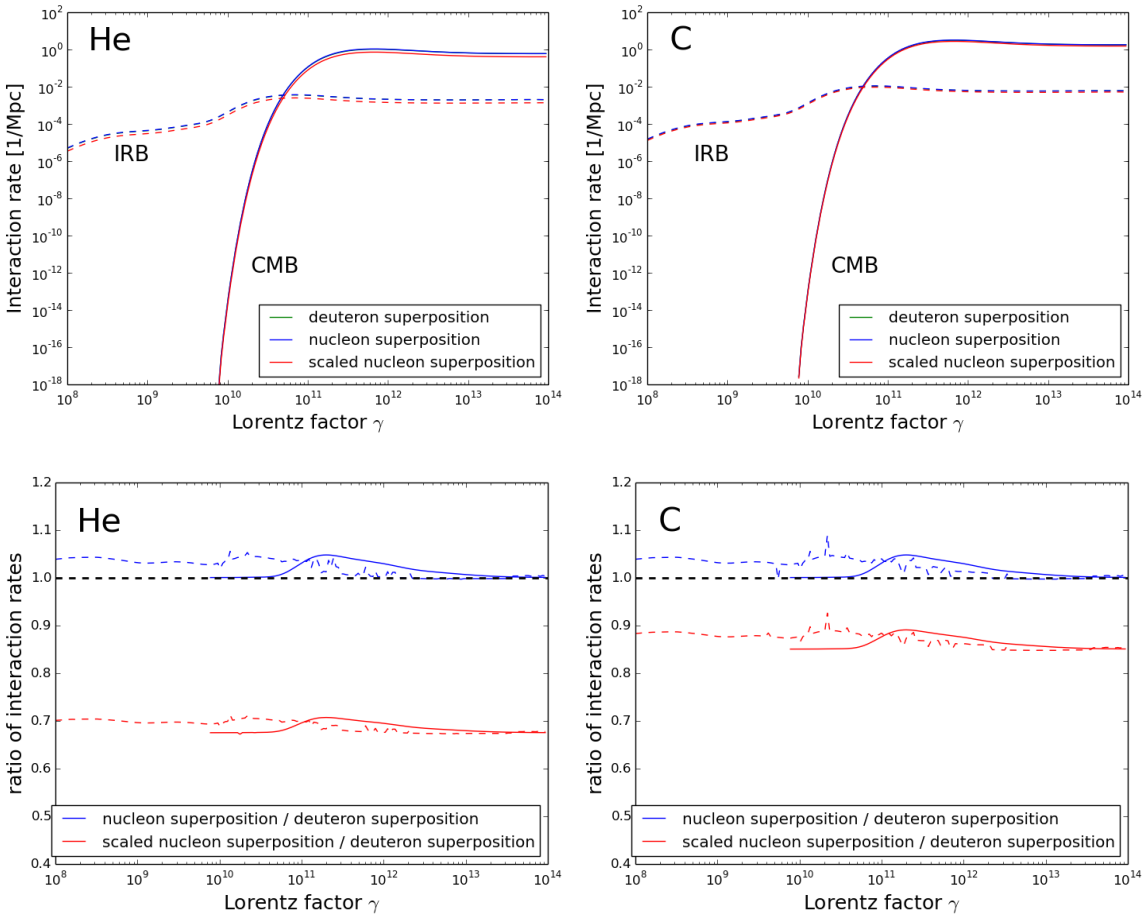

Figure 4.3: **Top row:** Interaction rate for the photo pion production calculated from the cross section derived by the deuteron superposition (green line) and the two nucleon superpositions (blue and red line) as described in the text. The interaction rates with the CMB (solid lines) and the IRB (dashed lines) are displayed. **Bottom row:** Ratio of the two interaction rate based on a nucleon superposition to the one based on the deuteron superposition. Again the interaction with CMB is indicated with solid lines and the one with the IRB with dashed lines. The plots are shown for He (left column) and C (right column) nuclei.

5 Combined Fit to the Energy Spectrum and the X_{max} Moments

In this chapter we concentrate on the predictions for the cosmic ray energy spectrum, the average depth of the shower maximum $\langle X_{\mathrm{max}} \rangle$ and the amplitude of the shower-to-shower fluctuation of the $\langle X_{\mathrm{max}} \rangle$ which are derived for different astrophysical scenarios from simulations with the CRPropa code. The main focus is to constrain these astrophysical scenarios from a combination of these predictions to the data from the Pierre Auger Observatory [95].

The aim is to determine the energy spectrum, the maximum energy and the mass composition at potential sources of UHECR. The limited knowledge available for cosmic ray sources and the properties of the extragalactic space as described in Sec. 2.1.5 and Sec. 2.2 adds further models assumptions. Several scenarios will be discussed in this context to estimate the influence of these assumptions on the fit results as well as to put constraints on them.

In the first section of this chapter the technical details of the CRPropa simulations, the calculation of observables from the simulation and the fit procedure are described. In the second section the results of the combined fit are presented starting with a standard scenario with a set of simplified model assumptions which is regarded for three source composition models. Here also the results from fitting solely the energy spectrum are shown. Then these first results are tested for the influence of a number of mainly technical assumptions. Based on the standard scenario the origin of the cosmic ray flux suppression at the highest energies is investigated. Subsequently, more realistic scenarios are studied by taking different source evolutions models and magnetic diffusion effects into account. Special features of the Auger data are not well described by a simple source model. Therefore, models with two source populations are studied. Finally, a spread of spectral indices is tested.

5.1 Introduction of General Scenario and Methods

5.1.1 General scenario

In the standard scenarios cosmic rays are injected at continuous sources distributed uniformly in comoving distance from 4 Mpc to 2600 Mpc. 4 Mpc is roughly the distance to Centaurus A [151] which is the nearest active galactic nucleus and often regarded as a promising candidate for the nearest UHECR source.

No sources more distant than 2600 Mpc are simulated as they lie beyond the cosmic ray horizon for the here relevant energy range of $E > 10^{18}\,\mathrm{eV}$. This can be seen in

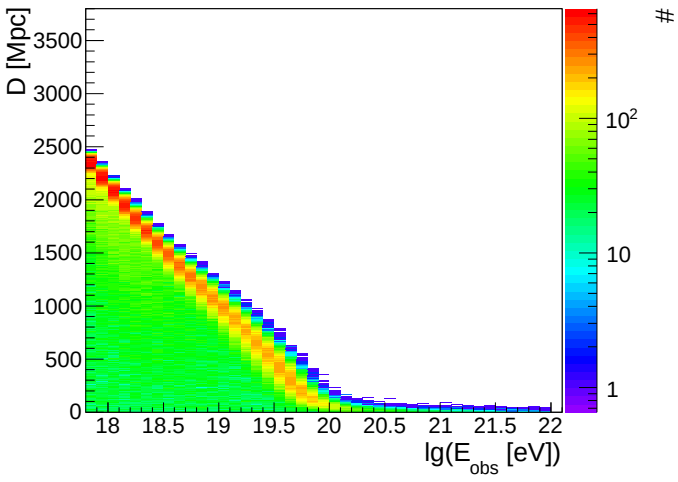

Figure 5.1: Number of cosmic ray protons which travelled the distance D and observed at energy E_{obs}. A power law spectrum with $\alpha = -1$ and maximum energies of $E_{\mathrm{max}} = 10^{22}\,\mathrm{eV}$ are assumed at the sources.

Fig. 5.1 where the number of observed cosmic rays in dependence of the travelled distance D and observed energy E_{obs} is shown assuming uniform proton sources with a spectral index $\alpha = -1$ and a maximum energy of $E_{\mathrm{max}} = 10^{22}\,\mathrm{eV}$. Nuclei have an even shorter horizon due to the shorter energy loss length.

Although a uniform distribution of UHECR sources is very unlikely as described in Sec. 2.1.6, this assumption is used in the standard scenario to allow a better comparison to similar studies as done by [93, 152, 153, 154, 155]. The influence of more realistic source distributions are discussed in Sec. 5.2.5. At each source, UHECRs are emitted with a power-law energy spectrum with a rigidity dependent cut-off

$$dN/dE(E_{\mathrm{src}}, Z) \propto E^{\alpha} \cdot 1/\cosh(E_{\mathrm{src}}/ZR_{\mathrm{max}}),$$

where α is the spectral index, $R_{\mathrm{max}} = E_{\mathrm{max}}/M$ the maximum rigidity and Z the charge of the nuclei.

In most scenarios of this chapter a four component source composition consisting of the nuclei hydrogen, helium, nitrogen and iron is used. These four nuclei are chosen as representatives of all nuclei up to iron as used in previous studies [152, 154, 156]. The four nuclei are varied individually, yielding three free parameters for the composition. This source composition scenario will be called HHeNFe from here on. Further, a second mixed composition model is assumed according to the galactic cosmic ray source composition (GCRSC) as derived by DuVernois et al. [157, 158]. In this case all nuclei from hydrogen to iron are assumed at the sources with abundances of galactic cosmic ray sources as used by [158]. For a better agreement the abundances for all particles with $Z \geq 3$ are simultaneously scaled with a factor k_{c} compared to protons and helium nuclei. With this approach only one parameter is needed to vary the composition. As an alternative to the mixed composition scenario pure proton sources are considered as suggested for example by Berezinsky et al. [27].

5.1.2 Deriving the Observables from Simulation Output

For all studies a reweighting of the simulated events is applied with respect to the source spectra, the maximum source energy and the relative abundances of the nuclei at the sources. This allows to perform the fit with one set of simulated events for each scenario without performing a new simulation for each parameter configuration. The simulation is done with a spectral index of $\alpha = -1$ and a maximum energy of $9 \cdot 10^{23}\,\mathrm{eV}$. For the HHeNFe composition, equal abundances at the source for all four nuclei at same energy per nuclei are simulated. For the GCRSC the nuclei are injected with the abundances given in DuVernois et al. [157] with a hundred times higher statistics for nuclei heavier than helium. The scaling with k_c as described above is done by a reweighting. The spectrum is derived from the simulation output by using data binned in source energy E_{src}, source charge Z_{src} and observed energy E_{obs} choosing for the energies an equidistant binning in the logarithm of 0.1. This is done instead of reweighting the whole simulated data for performance reasons. The simulated spectrum can be calculated according to

$$dN/dE(E_{\mathrm{obs}}) = \sum_{E_{\mathrm{src}}} \sum_{Z_{\mathrm{src}}} dN/dE(E_{\mathrm{obs}}, E_{\mathrm{src}}, Z_{\mathrm{src}}) \cdot E_{\mathrm{scr}}^{\alpha} \cdot 1/\cosh(E_{\mathrm{scr}}/Z \cdot R_{\mathrm{max}}).$$

$\langle X_{\mathrm{max}} \rangle$ and $\sigma(X_{\mathrm{max}})$ are calculated from the $\langle \ln(A) \rangle$ and $\sigma(\ln(A))$ values of the simulated data by using the parametrization from [105, 95] as described in Sec. 2.6. To calculate the reweighted $\langle \ln(A) \rangle$ and $\sigma(\ln(A))$ three dimensional matrices are generated with the sum of ln(A)

$$\Omega(E_{\mathrm{obs}}, E_{\mathrm{src}}, Z_{\mathrm{src}}) = \sum_{\mathrm{Bin}(E_{\mathrm{obs}}, E_{\mathrm{src}}, Z_{\mathrm{src}})} \ln(A_i),$$

the number of entries

$$\#(E_{\mathrm{obs}}, E_{\mathrm{src}}, Z_{\mathrm{src}}) = \sum_{\mathrm{Bin}(E_{\mathrm{obs}}, E_{\mathrm{src}}, Z_{\mathrm{src}})} 1$$

and the sum of $\ln(A)^2$

$$\Delta(E_{\mathrm{obs}}, E_{\mathrm{src}}, Z_{\mathrm{src}}) = \sum_{\mathrm{Bin}(E_{\mathrm{obs}}, E_{\mathrm{src}}, Z_{\mathrm{src}})} \ln(A_i)^2.$$

Here, $\sum_{\mathrm{Bin}(E_{\mathrm{obs}}, E_{\mathrm{src}}, Z_{\mathrm{src}})}$ refers to sum over all events within the bin defined by E_{obs}, E_{src}, Z_{src}. Hence the $\langle \ln(A) \rangle$ is calculated via

$$\langle \ln(A) \rangle (E_{\mathrm{obs}}) = \frac{\sum_{E_{\mathrm{src}}} \sum_{Z_{\mathrm{src}}} \Omega(E_{\mathrm{obs}}, E_{\mathrm{src}}, Z_{\mathrm{src}}) \cdot E^{\alpha} \cdot 1/\cosh(E/ZR_{\mathrm{max}})}{\sum_{E_{\mathrm{src}}} \sum_{Z_{\mathrm{src}}} \#(E_{\mathrm{obs}}, E_{\mathrm{src}}, Z_{\mathrm{src}}) \cdot E^{\alpha} \cdot 1/\cosh(E/ZR_{\mathrm{max}})}.$$

Once the $\langle \ln(A) \rangle$ is calculated the $\sigma(\ln(A))$ is obtained via

$$\sigma(\ln(A))(E_{\mathrm{obs}}) = \frac{\sum_{E_{\mathrm{src}}} \sum_{Z_{\mathrm{src}}} \xi(E_{\mathrm{obs}}, E_{\mathrm{src}}, Z_{\mathrm{src}}) \cdot E^{\alpha} \cdot 1/\cosh(E/ZR_{\mathrm{max}})}{\sum_{E_{\mathrm{src}}} \sum_{Z_{\mathrm{src}}} \#(E_{\mathrm{obs}}, E_{\mathrm{src}}, Z_{\mathrm{src}}) \cdot E^{\alpha} \cdot 1/\cosh(E/ZR_{\mathrm{max}})},$$

with

$$\begin{aligned}
\xi &= \sum_{\mathrm{Bin}(E_{\mathrm{obs}},E_{\mathrm{src}},Z_{\mathrm{src}})} (\ln(A_i) - \langle \ln(A) \rangle (E_{\mathrm{obs}}))^2 && (5.1)\\
&= \sum_{\mathrm{Bin}(E_{\mathrm{obs}},E_{\mathrm{src}},Z_{\mathrm{src}})} ((\ln(A_i))^2 - 2\ln(A_i)\langle \ln(A) \rangle + \langle \ln(A) \rangle^2) && (5.2)\\
&= \sum_{\mathrm{Bin}(E_{\mathrm{obs}},E_{\mathrm{src}},Z_{\mathrm{src}})} (\ln(A_i))^2 - 2\langle \ln(A) \rangle (E_{\mathrm{obs}}) \sum_{\mathrm{Bin}(E_{\mathrm{obs}},E_{\mathrm{src}},Z_{\mathrm{src}})} \ln(A_i) && (5.3)\\
&\quad +\#(E_{\mathrm{obs}}, E_{\mathrm{src}}, Z_{\mathrm{src}}) \langle \ln(A) \rangle^2 && (5.4)\\
&= \Delta(E_{\mathrm{obs}}, E_{\mathrm{src}}, Z_{\mathrm{src}}) - 2\langle \ln(A) \rangle (E_{\mathrm{obs}}) \Omega(E_{\mathrm{obs}}, E_{\mathrm{src}}, Z_{\mathrm{src}}) && (5.5)\\
&\quad +\#(E_{\mathrm{obs}}, E_{\mathrm{src}}, Z_{\mathrm{src}}) \langle \ln(A) \rangle^2. && (5.6)
\end{aligned}$$

This using of binned source energies obviously introduces an uncertainty. The result of this procedure is compared with a reweighting of all simulated events for different parameter constellations to estimate this effect. Only deviations of less than 1 % are found for the energy spectrum, $\langle X_{\mathrm{max}} \rangle$ and $\sigma(X_{\mathrm{max}})$. Fig. 5.2 displays an example of the deviation from the unbinned result for the HHeNFe standard scenario with parameters fixed by the combined fit as will be introduced in Sec. 5.2.2.

5.1.3 Fit Procedure

The comparison of energy spectrum as well as the energy dependent $\langle X_{\mathrm{max}} \rangle$ and $\sigma(X_{\mathrm{max}})$ measurements from the Pierre Auger Observatory [95] with the predictions from propagation simulations is done by a χ^2 fit. For minimizing the χ^2-function the numerical minimization program MINUIT [159] implemented in the data analysis program ROOT [160] is used. MINUIT uses the MIGRAD minimization algorithm based on a variable metric method [161].

The parameter range for the source spectral index is $\alpha \in [-3, 0]$ and for the maximum rigidity is $\lg(R_{\mathrm{max}}/\mathrm{eV}) \in [18.4, 22.4]$. The absolute flux scaling is also included in the fit. In the galactic cosmic ray source composition scenario k_{c} is varied between 0 and 100. For the HHeNFE scenario every possible relative abundances of these four elements are allowed. Statistical uncertainties of the data are considered in the fit procedure. To take into account the systematic uncertainties of the data the fit is redone with the energy scale shifted by the systematic uncertainty in the energy scale of 14 % [95]. The resulting deviations in the parameters are taken as the systematic uncertainties of the fit parameters.

Only data with $E \geq 10^{18.7}\,\mathrm{eV}$ are regarded here to reduce the influence of galactic cosmic rays which are not included in the simulation. The threshold energy corresponds to the ankle in the energy spectrum as mentioned in Sec. 3.3.1 and is usually considered as the transition from galactic to extragalactic cosmic rays as described in Sec. 2.1.2. Hence, 15 data points for the energy spectrum and nine data points for each of $\langle X_{\mathrm{max}} \rangle$ and $\sigma(X_{\mathrm{max}})$ are considered, leading to a total of 33 data points.

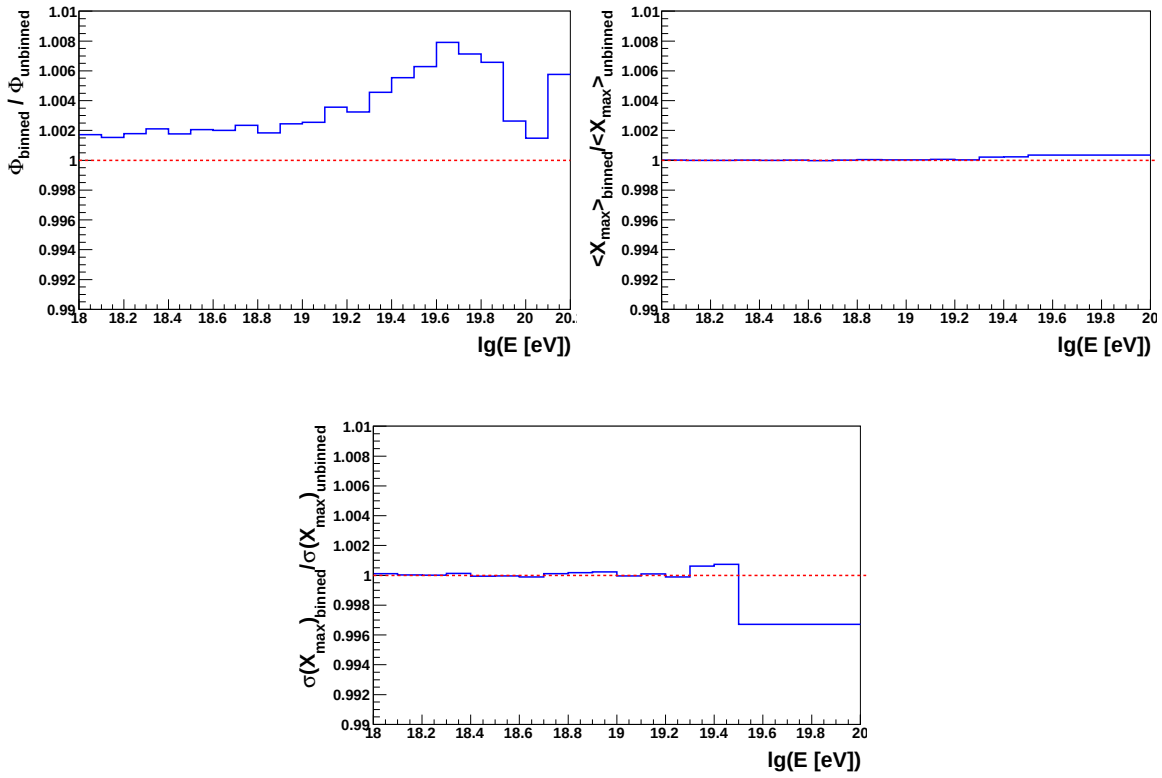

Figure 5.2: Estimation of the influence from the calculation using binned energies at the sources as described in the text. The ratio of the binned calculation to the unbinned one is shown for the following observables. **Top left:** Energy spectrum **Top right:** $\langle X_{\max} \rangle$ distribution **Bottom:** $\sigma(X_{\max})$ distributions. The standard HHeNFe scenario with the parameters derived from the combined fit to the energy spectrum and the $X_{\max}$ moments is used.

Continuous vs Point Sources Besides Sec. 5.2.7, in all scenarios in this chapter and chapter 6 a continuous source distribution is assumed. This is a simplification, as most source candidates like AGN or pulsars as introduced in Sec. 2.1.5 are assumed to be point sources. Furthermore, we will use point sources in the three dimensional simulations in chapter 7 where the results of this chapter will be used. To test the assumption of a uniform continuous source distribution the result from sources distributed continuously between 10 Mpc and 2600 Mpc are compared with the one from a certain amount of sources at different equidistant positions in the same distance range. The plots in Fig. 5.3 show the ratio of the flux of continuous and point sources for different elements at the source. In case of 100 point sources, a large increase of the flux from continuous sources for energies above 10^{20} eV is seen which increases with the nuclei charge number yielding a 200 times increase for iron nuclei at $10^{20.5}$ eV as a peak value. Increasing the number of point sources to 1000 in the same distance range

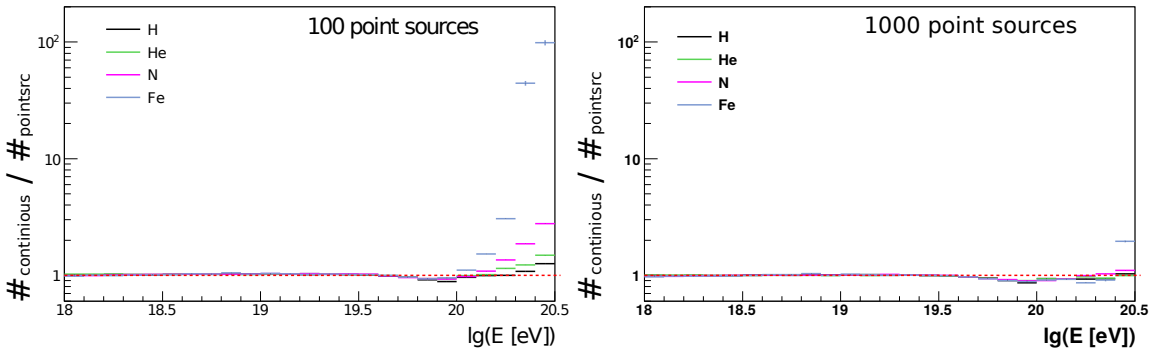

Figure 5.3: Comparison of a continuous source distribution to discrete sources distributed equidistant between 10 Mpc and 2600 Mpc. The ratio of the energy spectrum from continuous sources to the one from point sources for four individual masses at the source are displayed. **Left:** Comparison with 100 point sources. **Right:** Comparison with 1000 point sources

show a strong decrease of the effect yielding only a significant flux increase up to a factor of two again for iron nuclei at $10^{20.5}$ eV. The impact of the energy spectrum and the first two $\langle X_{\mathrm{max}} \rangle$ moments is also very moderate. Regarding these small differences the simplification of a continuous source distribution should not introduce significant alteration of the results. A spectral index of $\alpha = -1$ and $E_{\mathrm{max}} = 10^{22}$ eV is used in this comparison.

5.1.4 Choice of Further Assumptions

While studying different parameters of the astrophysical scenarios by their influence on the fit result in Sec. 5.2 some additional assumptions will be made in this thesis.

- For all sources the cut-off of the energy spectrum is realized by a $1/\cosh(E_{\mathrm{src}}/(Z_{\mathrm{src}} \cdot R_{\mathrm{max}}))$ cut-off.
- The redshift evolution of the infrared background is done according to measurements by Kneiske et al. [2].
- Epos LHC [162] is taken as high energy extrapolations of the nuclei interaction rates to calculate $\langle X_{\mathrm{max}} \rangle$ in the atmosphere.
- TALYS 1.6 is used for the calculation of photodisintegration cross sections used in the intergalactic propagation.

The influence of alternative assumptions on the fit results will be shown in Sec. 5.2.3 to give an idea of the sensitivity to these assumptions.

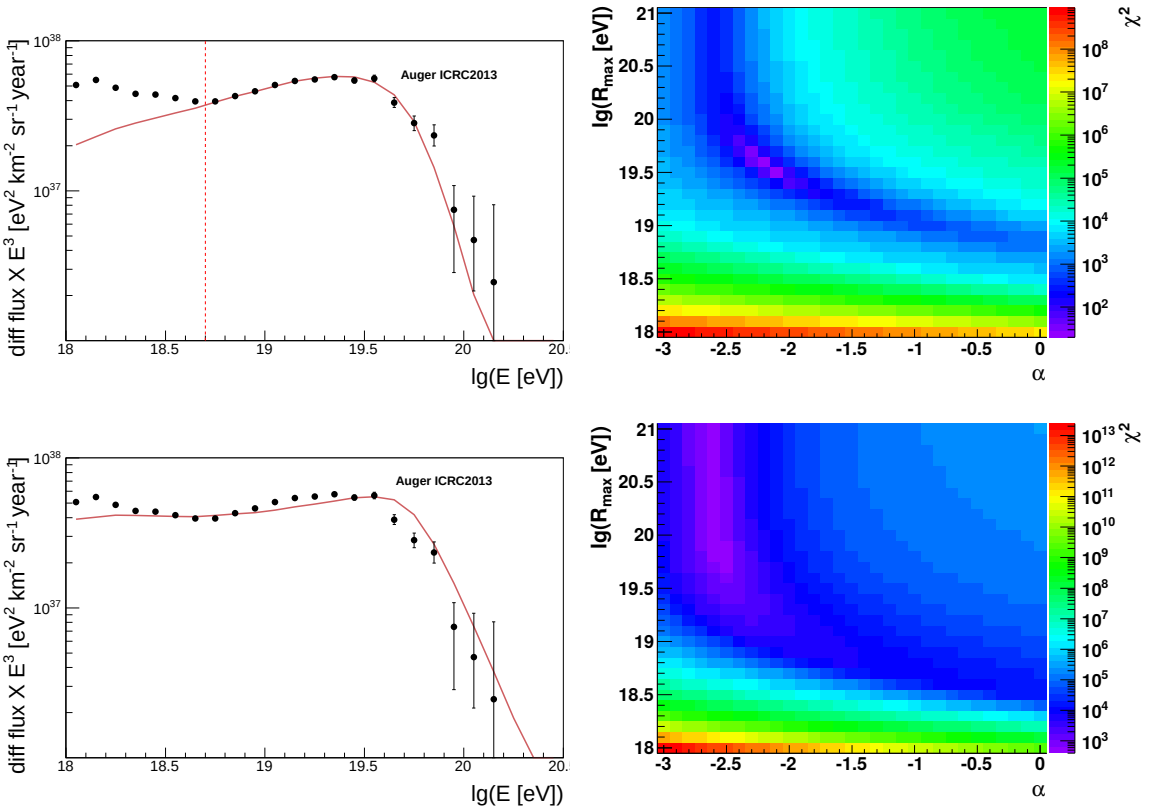

Figure 5.4: **Top left:** The energy spectrum from simulation assuming pure proton sources plotted along with the measured combined energy spectrum from the Pierre Auger Observatory [95]. The parameters for the simulation are received from a fit to the energy spectrum for the energies range $E > 10^{18.7}\,\mathrm{eV}$ as indicated by the dotted red vertical line. **Top right:** The fit quality χ^2 for a scan of the spectral index and maximum rigidity at the sources for the same scenario as in the top left plot. **Bottom:** Same as the top row but for a fit range of $E > 10^{18}\,\mathrm{eV}$.

5.2 Results

5.2.1 Fit to the Energy Spectrum

In the first approach a mere fit to the energy spectrum is executed for the three composition scenarios introduced above. Starting with a pure proton composition at the sources the upper left plot in Fig. 5.4 displays the good agreement of the energy spectrum from the simulation with the data. The fit results in a $\chi^2/ndf = 1.4$ for a spectral index of $\alpha = -2.2$, consistent with Fermi acceleration [47, 48] and a maximum rigidity of $R_{\mathrm{max}} = 10^{19.6}\,\mathrm{eV}$ as also listed in Tab. 5.1. The upper right plot of Fig. 5.4 shows the χ^2 of the fit for different combinations of α and R_{max} in a scan of these parameter spaces. This scan is given to supply an overview whereas the fit itself

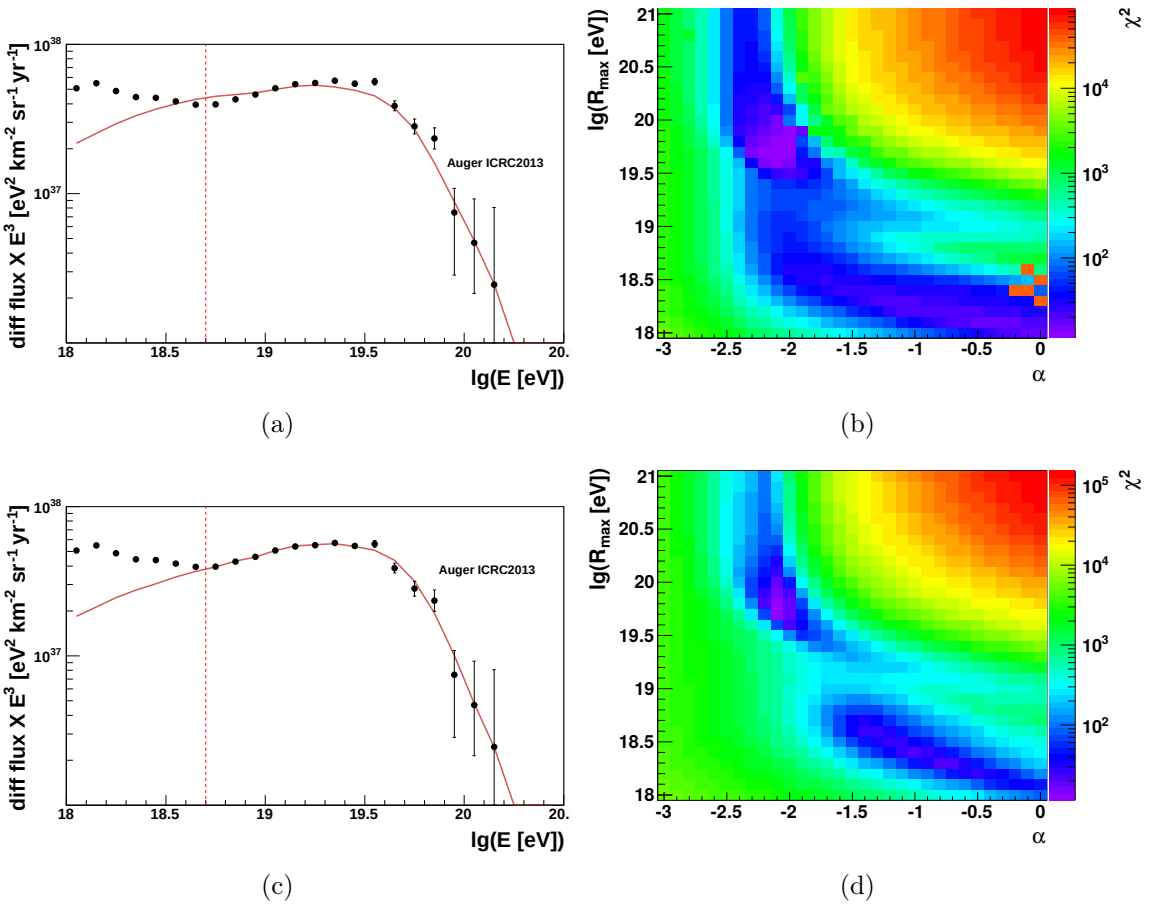

Figure 5.5: **Top row:** Same as the top row of Fig. 5.4 but assuming the HHeNFe composition at the sources. **Bottom row:** Same as the top row but using the GCRSC composition scenario.

is performed using simultaneous minimization procedure as described in Sec. 5.1.3. Here, one minimum is found. As already mentioned in Sec. 2.1.2 the Berezinsky dip model allows a transition from galactic to extra-galactic CR flux at energies below 10^{18} eV in case of strongly proton dominated sources. But extending the fit range down to 10^{18} eV it is not possible to describe the energy spectrum properly. This is indicated by a bad fit quality of $\chi^2/ndf = 20.9$ and also visible in the comparison of the simulated energy spectrum with data in the bottom left plot in Fig. 5.4. In the simulation the flux suppression at the highest energies sets in too late and the accumulation of protons above the pair production threshold is too weak. It seems that the standard assumption chosen in this chapter disfavours the Berezinsky dip model. However, this will be restudied in Sec. 5.2.5 taking an alternative assumptions for the source evolution into account.

From Tab. 5.1 and Fig. 5.5 one can read that both mixed composition scenarios show a similar α and R_{max} compared to the fit to proton sources for $E > 10^{18.7}$ eV. The fit quality is even better with $\chi^2/ndf = 0.9$ for the GCRSC and $\chi^2/ndf = 1.3$

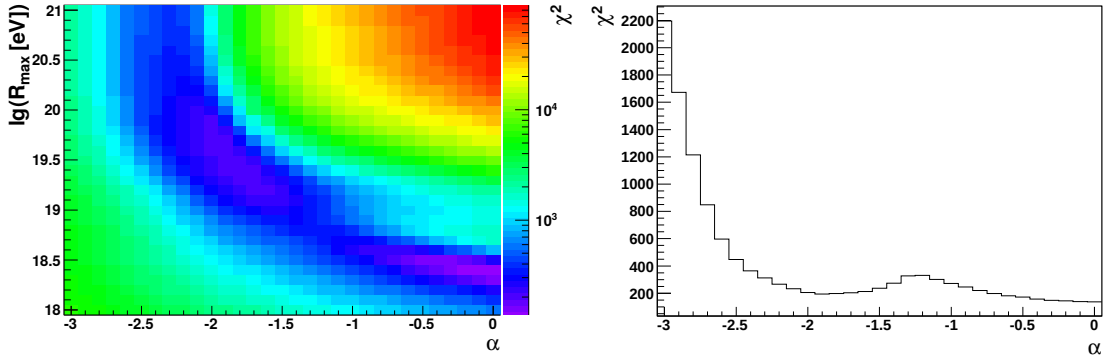

Figure 5.6: **Left:** χ^2 for the combined fit of the energy spectrum, $\langle X_{\max} \rangle$ and $\sigma(X_{\max})$ displayed for a scan in α and $R_{\max}$ assuming the HHeNFe scenario in the simulation.**Right:** Same as the left plot but only scanning α whereas $R_{\max}$ is determined by the fit procedure.

for the HHeNFe scenario. All three source mass compositions are able to fit the energy spectrum with parameters which are in agreement to common source candidate models.

Comparison with other Studies Similar studies are done for the proton dip model by Kotera et al. [65], for the GCRSC done by Allard et al. [93] and the HHeNFe model done by Boncioli et al. [153]. In most of these cases not a complete fit is performed or older data is used. Even though the spectral indices found for the pure proton spectrum fit agree with our work.

5.2.2 Standard Scenarios

After fitting only the energy spectrum in the previous section, in this section also the first two momenta of $X_{\max}$ are simultaneously fitted together with the energy spectrum.

Proton In case of the pure proton composition scenario the $\langle X_{\max} \rangle$ and $\sigma(X_{\max})$ predictions are obviously always in disagreement with the proton expectations and therefore do not agree with the data from the Pierre Auger Collaboration. Hence, the fit parameters do not change but the fit quality decreases from $\chi^2/ndf \approx 1.4$ to $\chi^2/ndf \approx 114.4$. Conclusively, a pure proton composition is not in agreement with data from the Pierre Auger Observatory.

HHeNFe Fitting the four component composition two minima are found as can be seen in Fig. 5.6, where the fit quality is given for a scan in α and $R_{\max}$. The first minimum is found for an extreme spectral index of $\alpha = 0$ with a maximum rigidity of

	α	$\lg(R_{\max}/\mathrm{eV})$	H	He	N	Fe	χ^2/ndf
1)	$-2.2^{+0.0\ +0.1}_{0.0\ -0.1}$	$19.6^{+0.0\ +0.1}_{0.0\ -0.1}$	1	0	0	0	16.7 / 12
2)	$-2.6^{+0.0\ +0.0}_{0.0\ -0.0}$	$20.1^{+0.0\ +0.4}_{0.0\ -0.2}$	1	0	0	0	397.7 / 19
	α	$\lg(R_{\max}/\mathrm{eV})$	H	He	N	Fe	χ^2/ndf
3)	$-2.1^{+0.1\ +0.0}_{0.1\ -0.1}$	$19.9^{+0.5\ +0.2}_{0.5\ -0.4}$	$8.5^{+91.8\ +68.5}_{91.8\ -8.5}$	$43.8^{+27.9\ +0.0}_{27.9\ -24.6}$	$41.5^{+70.7\ +8.5}_{70.7\ -41.5}$	$6.2^{+0.0\ +4.4}_{0.0\ -2.4}$	11.8 / 9
	α	$\lg(R_{\max}/\mathrm{eV})$	k_{c}				χ^2/ndf
4)	$-2.1^{+0.0\ +0.1}_{0.0\ -0.0}$	$19.7^{+0.1\ +0.2}_{0.1\ -0.1}$	$0.9^{+0.9\ +2.3}_{0.9\ -0.3}$				10.3 / 11

Table 5.1: Results derived by a fit of the energy spectrum from simulations to the data from the Pierre Auger Observatory [95]. The scenarios assume pure proton sources **(1)** **(2)**, HHeNFe source **(3)** and GCRSC sources **(4)** and otherwise the standard scenario as specified in the text. The fit is done for energies $E > 10^{18}\,\mathrm{eV}$ for **(2)** and for $E > 10^{18.7}\,\mathrm{eV}$ in the other scenarios.

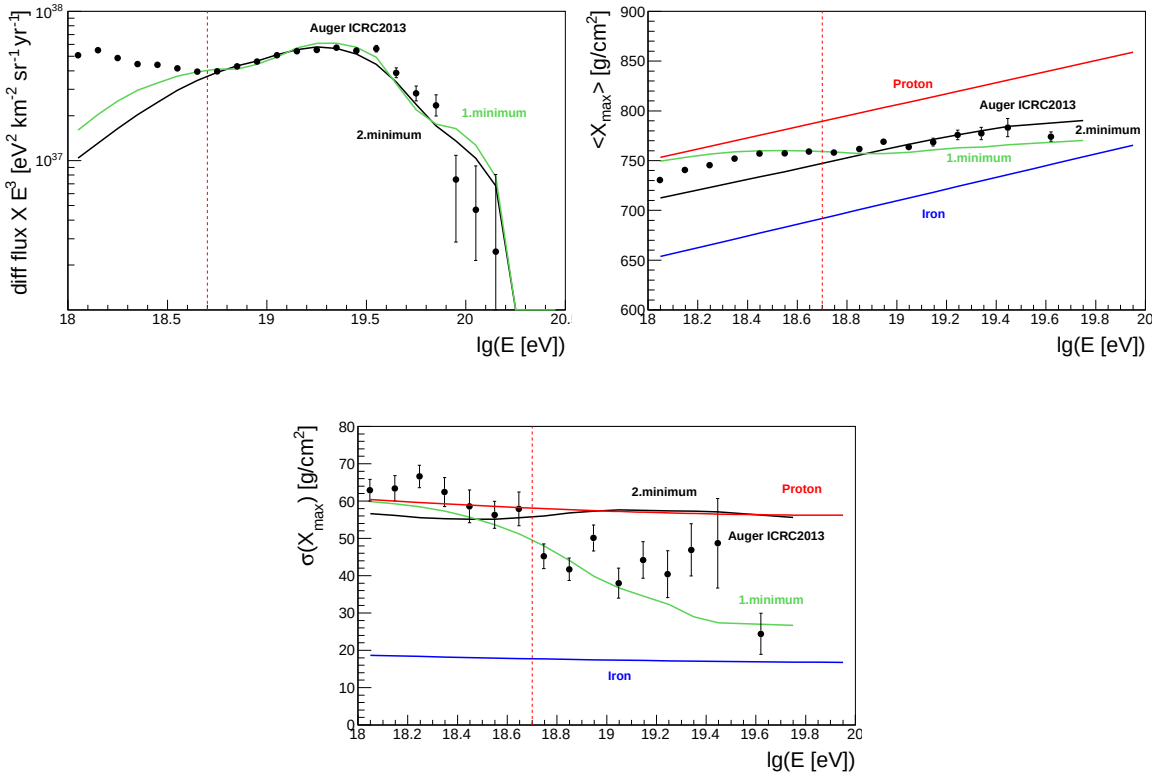

Figure 5.7: Energy spectrum (top left) $\langle X_{\max} \rangle$ (top right) and $\sigma(X_{\max})$ (bottom row) from simulations assuming the HHeNFe composition scenario and with parameters derived from a combined fit for the energy range $E > 10^{18.7}\,\mathrm{eV}$. The simulated entities are plotted for both minima of the fit results as described in the text. The data from the Pierre Auger Observatory [95] and for the $X_{\max}$ moments the expectation lines for protons and iron at the observer are additionally plotted.

$R_{\max} = 10^{18.4}\,\mathrm{eV}$ and a source composition dominated by hydrogen and nitrogen nuclei. In addition to the energy spectrum also the $\langle X_{\max} \rangle$ and the $\sigma(X_{\max})$ development are roughly described as seen in Fig. 5.7. With a cut-off energy which lies below the GZK threshold the scaling of the maximum energy with the charge of the nuclei is also preserved for the observed cosmic rays as shown in the left plot of Fig. 5.8. The resulting transition from light to heavy mass composition at the observer causes the transition of $\langle X_{\max} \rangle$ and $\sigma(X_{\max})$ to lower values with energy as seen in the data. The main concern of this result is that no theoretical prediction exist for such a hard spectral index.

The second minimum is found at reasonable spectral index of $\alpha = -1.9$, $R_{\max} = 10^{19.7}\,\mathrm{eV}$ and a source composition dominated by a heavy component. The disadvantage is a poor description of the $\sigma(X_{\max})$ distribution which leads to a higher $\chi^2/ndf \approx 7.1$ compared to $\chi^2/ndf \approx 5.0$ for the first minimum. The observed maxi-

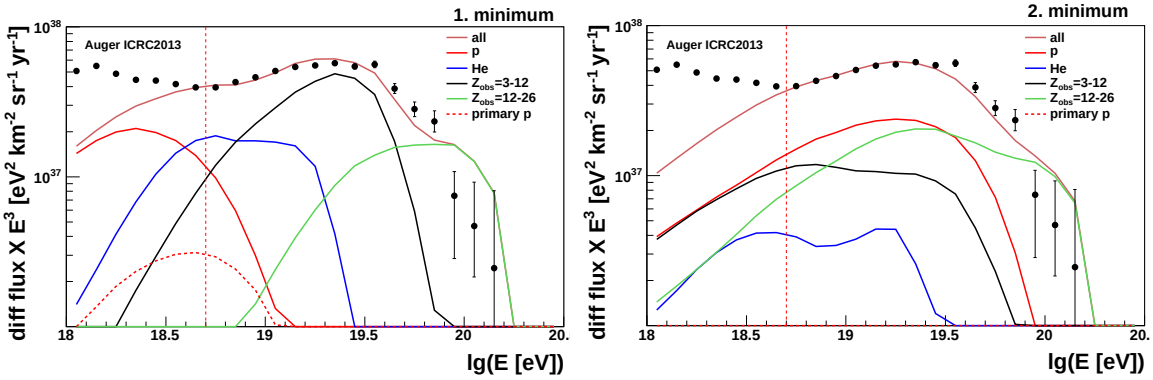

Figure 5.8: Same as the top left plot of Fig. 5.7 but with the energy spectra of different individual mass groups at the observer. **Left:** 1. minimum **Right:** 2. minimum

mum energy is heavily influenced by the energy losses during the propagation leading to a dominant secondary proton fraction up to $\sim 10^{19.5}$ eV as shown in the right plot of Fig. 5.8. Hence no transition to heavier nuclei is observed at the energies relevant for the X_{max} comparison with data. Despite this differences both minima show a worse description than in the mere spectrum fit.

GCRSC Corresponding to the results of the first mixed composition model also in the the GCRSC model two minima are found as seen in Fig. 5.9. The first one is at $\alpha = -1.9$, $R_{\mathrm{max}} = 10^{19.7}$ eV with very heavy composition of $k_c = 100$ and the second one at $\alpha = -1$, $R_{\mathrm{max}} = 10^{18.7}$ eV and $k_c = 37$. In contrast to the HHeNFe case both minima show similar fit quality whereby the minimum with the softer spectral index is with $\chi^2/ndf \approx 7$ even better than the minimum with the hard spectral index with $\chi^2/ndf \approx 7.2$. Although having again a very hard source spectrum in the latter case the value is moderate compared to the previous composition assumption and in Sec. 2.1.5 some theoretical predictions are also presented for this result. For the second minimum the $\langle X_{\mathrm{max}} \rangle$ and $\sigma(X_{\mathrm{max}})$ development show a tendency of a transition from a light to a heavy composition with rising energy, which is also seen in the data. Despite this feature especially the $\langle X_{\mathrm{max}} \rangle$ predictions do not match the data resulting in a bad fit quality. For the parameter set of the first minimum the $\langle X_{\mathrm{max}} \rangle$ shows a constant intermediate value between proton and iron and $\sigma(X_{\mathrm{max}})$ a very high value near the proton expectation for the whole energy range. As mentioned, both minima show again a worse fit quality than in the fit which considers only the energy spectrum. Although the HHeNFe scenario shows a slightly better fit for the first minimum the overall bad fit quality does not allow to discriminate between the HHeNFe and GCRSC scenarios.

Comparison with other Studies The result of the fit for the HHeNFe scenario corresponds with the two archetypal models fit to the Auger 2009 data [163, 164] by

	α	$\lg(R_{\max}/eV)$	H	He	N	Fe	χ^2/ndf
1)	$-0.0^{+0.0\ +0.0}_{-0.0\ -0.0}$	$18.4^{+0.0\ +0.0}_{-0.0\ -0.0}$	$76.9^{+2.4\ +0.0}_{-2.4\ -12.1}$	$3.6^{+0.7\ +15.8}_{-0.7\ 0.0}$	$19.4^{+3.1\ +0.9}_{-3.1\ -3.8}$	$0.1^{+0.0\ +0.0}_{-0.0\ -0.0}$	137.3 / 27
2)	$-1.9^{+0.0\ +0.3}_{0.0\ 0.0}$	$19.7^{+0.1\ +0.0}_{0.1\ -0.4}$	$0.0^{+6.2\ +47.6}_{6.2\ -0.0}$	$0.0^{+2.9\ +0.0}_{2.9\ -0.0}$	$74.5^{+1.9\ +3.1}_{1.9\ -47.2}$	$25.5^{+0.0\ +0.0}_{0.0\ -3.1}$	193.9 / 27

Table 5.2: Results derived by a combined fit of the energy spectrum, $\langle X_{\max}\rangle$ and $\sigma(X_{\max})$ from simulations to the data from the Pierre Auger Observatory [95]. The results for the first **(1)** and the second minimum **(2)** are given assuming the standard scenario as specified in the text with the HHeNFe composition.

	α	$\lg(E^{Fe}_{\max}/eV)$	kc	χ^2/ndf
1)	$-1.9^{+0.0\ +0.1}_{0.0\ -0.1}$	$19.7^{+0.0\ +0.2}_{0.0\ -0.2}$	$100.0^{+90.1\ +0.0}_{90.1\ -38.1}$	204.0 / 29
2)	$-1.0^{+0.1\ +0.3}_{0.1\ -0.8}$	$18.7^{+0.0\ +0.8}_{0.0\ -0.1}$	$37.1^{+10.0\ +24.8}_{10.0\ -1.8}$	209.7 / 29

Table 5.3: Same as Tab. 5.2 but for the GCRSC source composition

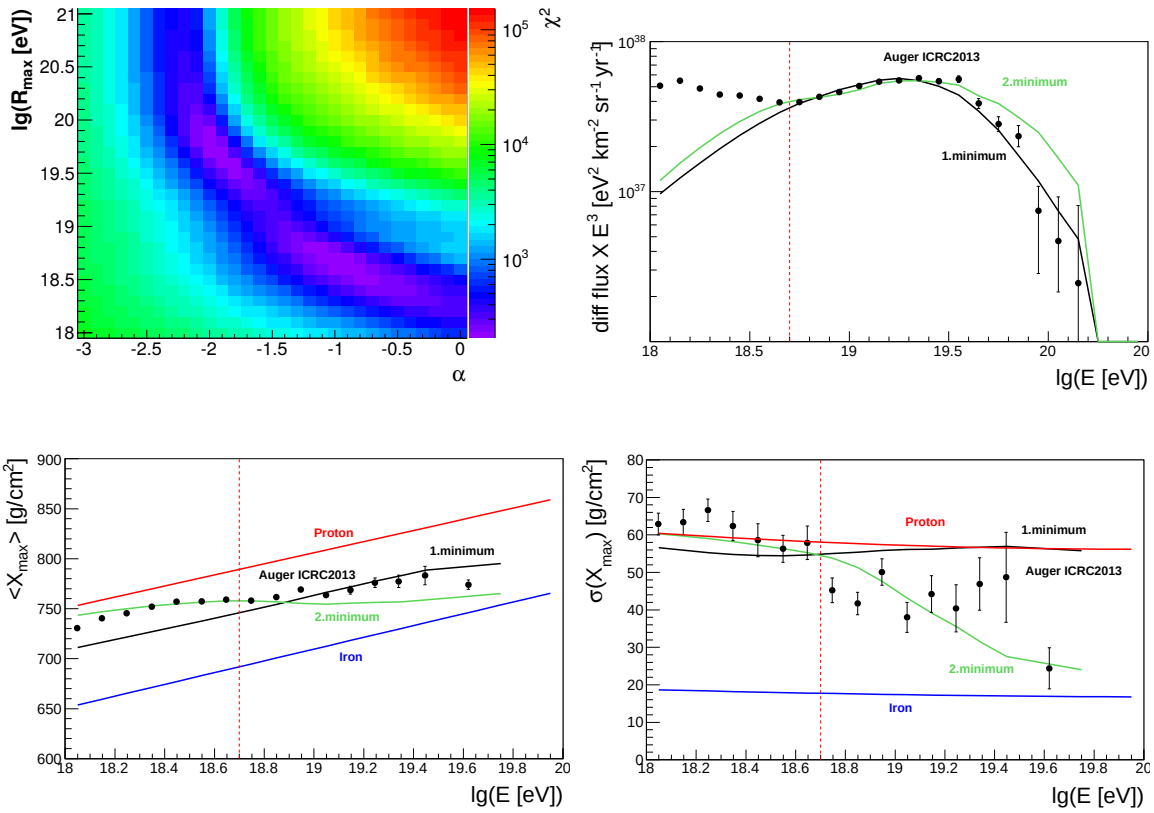

Figure 5.9: Same as Fig. 5.7 but for the GCRSC composition scenario.

Taylor [165]. The first assuming low maximum energy and dominant proton abundance yielding hard spectral index $\alpha = -1$ as no harder spectra are considered in that work. The second scenario presumes higher cut-off energies and an enhanced heavy nuclei component leading to spectral indices near $\alpha = -2$ claiming that both scenarios supply an adequate description of the data. Two very similar studies were done by Boncioli et al. [153, 166] and Walz et al. [155, 167] where also a full combined fit is performed very similar to the one in this work. A very good agreement for the second maximum is found using similar assumptions. As in these studies also spectral indices harder than 0 are considered, a first minimum at $\alpha = 1.5$ is found. Constraining the range of the spectral index to that of this work yields the same results. Also some earlier work by Riggi et al. [156] showed the preference of the data of a hard spectral index below $\alpha = -1$. Furthermore, Boncioli et al. [166] and Walz et al. [167] repeated the propagation simulations with a photodisintegration cross section that match better to data. This shows very small influence on the second minima in the fit but yields a softer spectral index in case of the first minima ranging from $\alpha = -0.4$ by Walz et al. to $\alpha = -1$ in case of Boncioli et al.

The desire for a hard spectral index or a high abundance of heavier nuclei for a good fit for the GCRSC scenario agrees with the studies of Allard et al. [93]. In that work a spectral index of $\alpha = -1.6$ is said to be necessary to fit the data. As no combined

fit is performed and no parameter range of the study is given this result can not be compared directly with this work.

5.2.3 Influence of Technical Assumptions on the Fit Results

In the following the fit on the second minimum of the standard HHeNFe scenario is used to give an idea of the influence of some assumptions which are made in this thesis and which are introduced in Sec. 5.1.4. These assumptions are the shape of the cut-off, the time evolution of the infrared background, the different high energy extrapolations of the hadronic interactions to calculate $\langle X_{\max} \rangle$ in the atmosphere and the photodisintegration cross sections used in the intergalactic propagation. The standard scenario used here slightly departs from the one specified in Sec. 5.1.1 by using the photodisintegration cross sections from TALYS in the version 1.0 instead of the version 1.6.

For these sensitivity tests all assumptions despite the studied one are set to the standard used in this thesis.

Choice of Cut-Off Function In all source models a maximum energy at the sources scaled by the charge Z of the nuclei is assumed. This corresponds to the fact that in the most theories of acceleration processes [51] as described in Sec. 2.1.5 a higher charge causes a higher Lorentz force which allows a longer containment in the acceleration area and hence a higher resulting energy. The shape of the cut-off of the energy spectrum is not well known. Usually an exponential flux suppression with the factor $e^{-E_{\mathrm{src}}/(Z \cdot R_{\max})}$ is assumed. As can be seen in the top left plot of Fig. 5.10, this cut-off influences the cosmic ray flux well below the maximum energy which also leads to a change of the spectral index at the source in the fit results. An alternative suppression factor of $1/\cosh(E_{\mathrm{src}}/(Z_{\mathrm{src}} \cdot R_{\max}))$ is suggested in [168] and significantly reduces the effect on the spectrum below the cut-off energy. The combined fit for the above defined standard scenario shows mainly a change in the spectral index when changing the 1/cosh cut-off to an exponential cut-off as can be seen in Tab. 5.4. To avoid this effect the cosh cut-off is used in this thesis.

	α	$\lg(R_{\max}/\mathrm{eV})$	H	He	N	Fe	χ^2/ndf
exp cut-off	-1.7	19.6	0	0	74	26	216/27
cosh cut-off	-1.9	19.6	0	0	71	29	243/27

Table 5.4: Results derived by a combined fit of the energy spectrum, $\langle X_{\max} \rangle$ and $\sigma(X_{\max})$ from simulations to the data from the Pierre Auger Observatory [95]. A standard scenario with the HHeNFe source composition as specified in the text is used. The range of spectra indices is limited to $\alpha < -1$. Different functions to realize the cut-off of the energy spectrum are used.

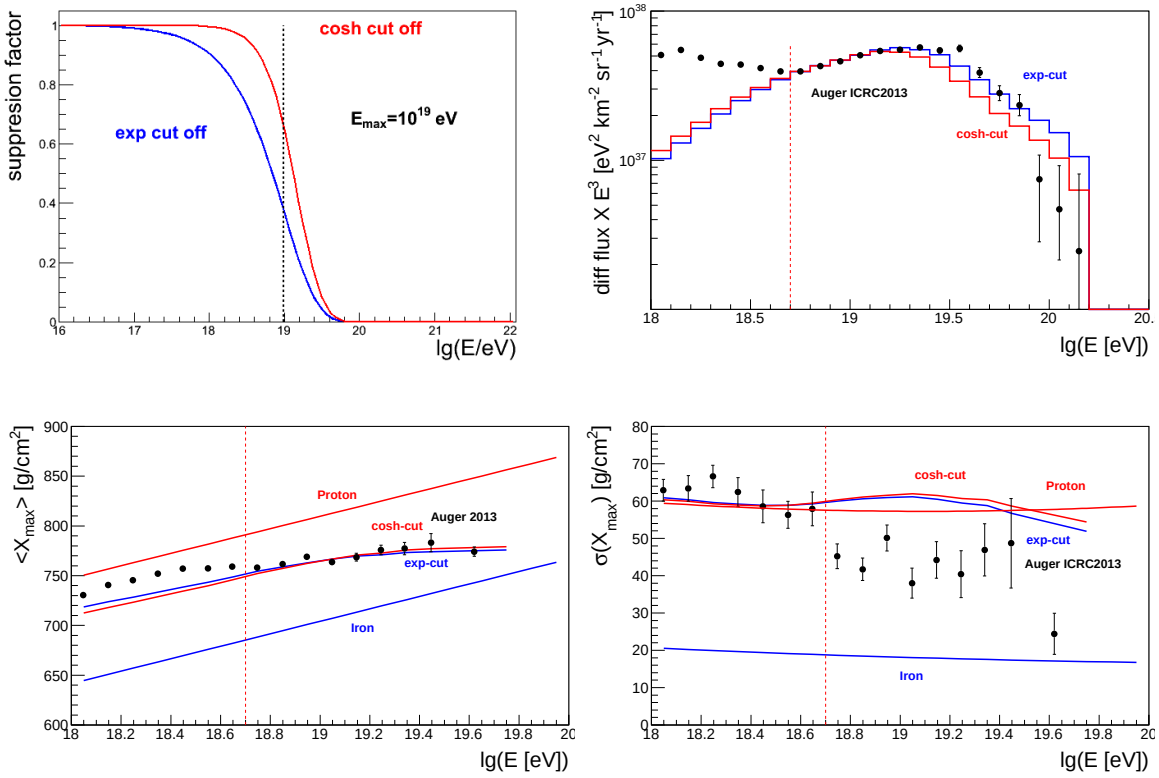

Figure 5.10: **Top left**: Comparison of the different suppression functions as introduced in the text for $E_{\max} = 10^{19}\,\mathrm{eV}$. **Top right and bottom row**: Observed energy spectrum $\langle X_{\max}\rangle$ and $\sigma(X_{\max})$ from simulations using the HHeNFe composition and parameters derived by a combined fit using the two different cut-off functions for the energy spectrum at the sources.

Evolution of the Infrared Background For the infrared background the version of Kneiske et al. [2] is used. The development of the infrared photon density with redshift z is done with an individual scaling interfered from a fit to according data [2] as introduced in Sec. 2.4.4. A comparison with the simplified assumption of a CMB-like scaling of the infrared background shows only minor differences in the fit results as listed in Tab. 5.5.

	α	$\lg(R_{\max}/\mathrm{eV})$	H	He	N	Fe	χ^2/ndf
Kneiske CMB scaling	-1.9	19.6	0	0	71	29	243/27
Kneiseke best fit	-1.9	19.6	0	0	73	27	256/27

Table 5.5: Same as shown in Tab. 5.4 but using two different evolution of the infrared background as described in the text.

Different Interaction Models for Calculating the $X_{\max}$ Moments As mentioned before, the calculation of the first two moments of $X_{\max}$ is done by air shower simulations which uses extrapolations of hadronic interaction features to the cosmic ray energies. Different models exist and their variety can be seen as the uncertainty existing for these extrapolations. With the knowledge of the recent LHC data [169] it was possible to improve these models to the two new versions Epos LHC [162], QGSJetII04 [170]. Epos LHC shows the best agreement with LHC data [169] and will be therefore used in this work. The influence of these two models and the three older models Epos 1.99 [171], Sibyll 2.1 [172] and QGSJetII [173] which can be seen as the most used ones in astroparticle physics on the fit results is tested. Table 5.6 shows mostly small variations of the fit parameters. Only in case of QGSJetII a change to a helium dominated source composition in contrast to the nitrogen dominated composition of the other interaction models is observed. The biggest impact can be seen in the fit quality, which ranges from $\chi^2/ndf = 6.6$ in case of QGSJetII to $\chi^2/ndf = 10.6$ for QGSJetII04. For the recent two models, Epos LHC shows the better fit.

	α	$\lg(R_{\max}/\mathrm{eV})$	H	He	N	Fe	χ^2/ndf
Epos 1.99	-1.9	19.6	0	0	73	27	256/27
Sibyll 2.1	-1.9	19.7	20	0	69	11	227/27
QGSJetII	-2.0	19.9	6	62	29	3	177/27
Epos LHC	-1.9	19.7	0	0	74	26	202/27
QGSJetII 04	-1.9	19.8	7	0	85	8	287/27

Table 5.6: Same as shown in Tab. 5.4 but using different extrapolations of the interaction models to calculate $\langle X_{\max}\rangle$ and $\sigma(X_{\max})$ from the simulated composition as described in the text.

TAYLS As already mentioned in Sec. 4.1 the calculation of the photodisintegration cross sections with the TALYS [140] framework is improved. The change from TALYS 1.0 to TALYS 1.6 causes nearly no change in the fit parameters but an increase in the fit quality as can be seen in in Tab. 5.7. This improvement is due to larger energy loss length caused by lower photodisintegration cross section from TALYS 1.6 that reduces the secondaries at low energies. It should be mentioned here that recent comparison of this cross sections with data [166, 167] show no good agreement. Although the TALYS 1.6 cross sections will be used in this work, the potential influence

	α	$\lg(R_{\max}/\mathrm{eV})$	H	He	N	Fe	χ^2/ndf
Talys 1.0	-1.9	19.7	0	0	74	26	202/27
Talys 1.6	-1.9	19.7	0	0	74	27	194/27

Table 5.7: Same as shown in Tab. 5.4 but using different models for the cross section of the photodisintegration for the propagation simulations as described in the text.

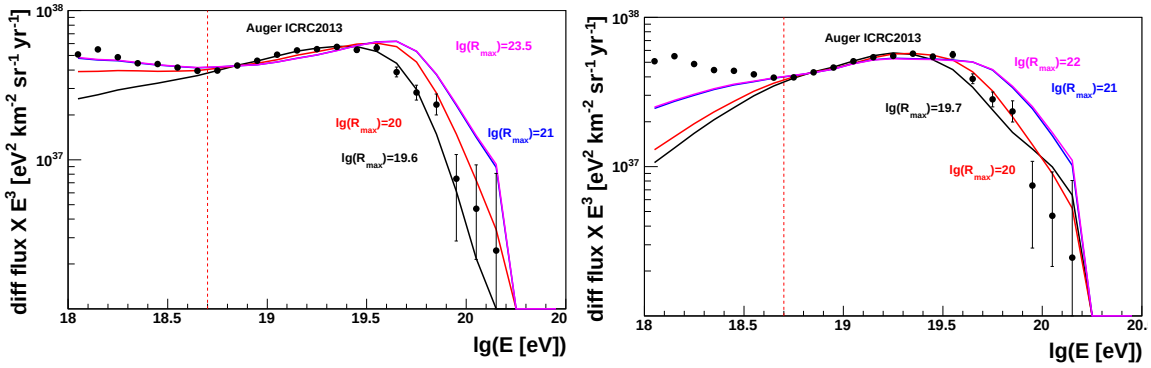

Figure 5.11: Energy spectrum from simulations with different fixed $R_{\max}$ and other parameters derived from a combined fit. **Left:** Assuming a pure proton scenario and a fit for energies $E > 10^{18}$ eV. **Right:** Assuming the HHeNFe scenario with a fit for $E > 10^{18.7}$ eV and using the minimum with $\alpha < -1$.

on the result is mentioned in Sec. 5.2 by a comparison to other studies.

5.2.4 GZK vs. Exhausted Sources

As already mentioned in Sec. 2.1.2 the suppression of the cosmic ray flux above $10^{19.6}$ eV is confirmed by the data [95]. The question arises whether this behavior is due to propagation effects, namely the GZK-effect, or because of the end of the energy spectrum at the sources. As seen in Sec. 5.2.2 the fit prefers a source spectrum which is cut-off at a maximum rigidity in the range $[10^{18.4}, 10^{20.1}]$ eV, depending on the source mass composition. In Fig. 5.11 the fit results for increasing fixed $R_{\max}$ show that the mere flux suppression due to the energy loss during the propagation causes a cut-off above the one observed by the Pierre Auger Observatory [95] which leads to a significantly reduced fit quality for a source accelerating cosmic rays to very high maximum rigidity as can be seen in the Tab. 5.8 and Tab. 5.9. This is observed in case of mixed composition as well as for pure proton sources. Again, a sole energy spectrum fit is performed for proton sources and a combined fit for the HHeNFe sources. Conclusively, the energy spectrum and the $X_{\max}$ moments of the Pierre Auger Observatory disfavours the GZK effect as the only reason for the flux suppression which can be seen at highest energies.

5.2.5 Alternative Source Evolution Scenarios

Up to now, uniform source distributions are assumed. As already mentioned in Sec. 2.1.6, most candidates for cosmic ray sources are more likely to show an increase in source density with redshift. In this section the combined fit is performed with sources distributed according to the star formation rate (SFR) and to quasars as introduced in Sec. 2.1.6. For the here relevant redshift below $z = 1$ the density ρ

$\lg(R_{\max}/\mathrm{eV})$	α	χ^2/ndf
19.6	-2.2	17.1 / 13
20.0	-2.5	144.5 / 13
21.0	-2.6	322.3 / 13
23.5	-2.6	332.3 / 13

Table 5.8: Results derived for a fit of the energy spectrum from simulations to the data from the Pierre Auger Observatory [95]. The standard scenario with proton sources is used where different fixed maximum rigidities are assumed. The fit is done for energies $E > 10^{18.7}\,\mathrm{eV}$.

$\lg(R_{\max}/\mathrm{eV})$	α	H	He	N	Fe	χ^2/ndf
19.7	-1.9	0.0	0.0	74.5	25.5	193.9 / 28
20.0	-2.0	0.0	0.5	77.7	21.7	236.6 / 28
21.0	-2.3	0.0	73.9	0.0	26.1	418.9 / 28
22.0	-2.3	0.0	73.6	0.0	26.4	442.0 / 28

Table 5.9: Same as Tab. 5.8 but for a combined fit of the spectrum, $\langle X_{\max}\rangle$ and $\sigma(X_{\max})$ and the HHeNFe mass composition scenario.

increases for SFR sources with $\rho(z) \propto (1+z)^{3.4}$ whereas quasars show an even steeper increase. The pure proton scenarios for an early and a late galactic to extragalactic transition as well as the four component scenario are chosen for this study. Note that again only a fit to the energy spectrum is performed in case of proton sources. The results in Tab. 5.10–5.12 and Fig. 5.12–5.13 show a hardening of the spectral index with increasing steepness of the source evolution for all three mass scenarios. In case

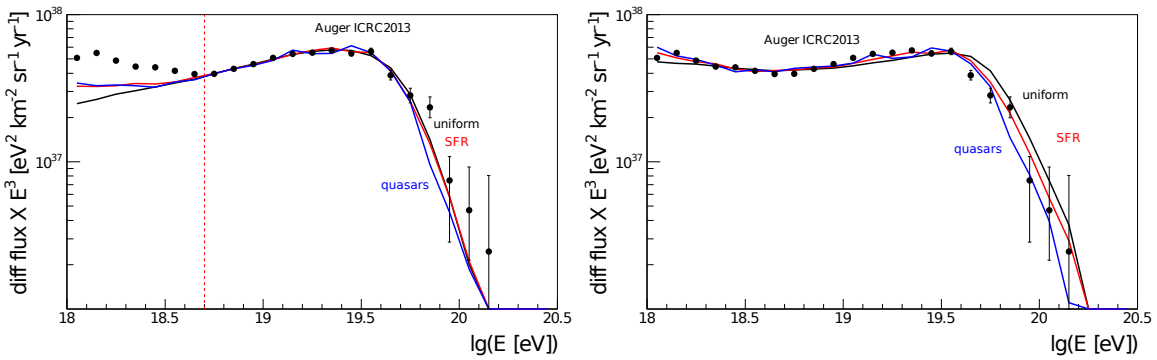

Figure 5.12: Predicted energy spectrum with parameters derived by a fit of the energy spectrum assuming three different source evolutions scenarios as described in the text assuming further pure proton sources. **Left:** Fit done for the energy range $E_{\min} = 10^{18.7}\,\mathrm{eV}$. **Right:** Fit done for the energy range $E_{\min} = 10^{18}\,\mathrm{eV}$.

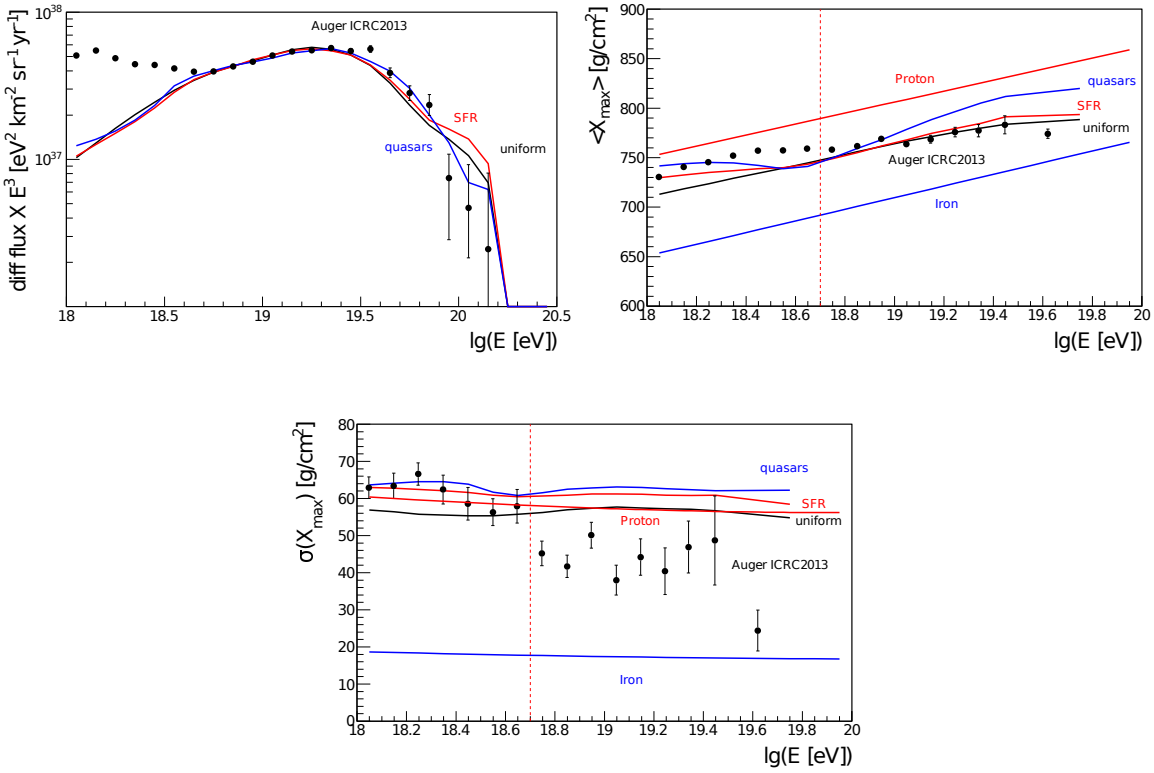

Figure 5.13: Predicted energy spectrum, $\langle X_{\mathrm{max}} \rangle$ and $\sigma(X_{\mathrm{max}})$ energy evolution with parameters derived by a combined fit assuming three different source evolutions scenarios as described in the text assuming further the HHeNFe composition scenario.

of the mixed mass and proton composition with a fit above $E = 10^{18.7}\,\mathrm{eV}$ the maximum rigidity shows no significant change. For the HHeNFe scenario the heaviness of the mass composition also increases with steeper source evolution. Cosmic rays from more distant sources undergo more interactions and hence mainly contribute the flux at low energies. The increase of more distant sources in case of SFR and quasars leads to an higher abundance at low energies. Both, a harder source spectrum and a heavier composition can compensate this overabundance. Due to the rigidity dependent cut-off lighter nuclei at the source also contribute to lower observed energies. Hence, lower abundances of lighter cosmic rays leads to lower fluxes at lower energies. In both late galactic to extragalactic transition scenarios SFR and quasars source evolution assumptions lead to a significantly worse fit compared to uniform sources.

Regarding again a fit for $E > 10^{18}\,\mathrm{eV}$ for proton sources, as suggested by Beresinzky et al. [27], the fit improves for SFR sources. As already seen in Sec. 5.2.1 the increased abundance of cosmic rays above the threshold energy for proton pair production was not strong enough to mimic the ankle in the Auger data for a uniform source distribution. An increased source evolution as in case of SFR leads to more secondary

	α	$\lg(R_{\max}/\mathrm{eV})$	χ^2/ndf
uniform	-2.2	19.6	16.7 / 12
SFR	-2.1	19.6	20.0 / 12
quasars	-1.7	19.5	50.1 / 12

Table 5.10: Results derived for a fit of the energy spectrum from simulations to the data from the Pierre Auger Observatory [95]. Proton sources are used and different evolutions of the source density are tested assuming otherwise the standard scenario as specified in the text. The fit is done for energies $E > 10^{18.7}\,\mathrm{eV}$.

	α	$\lg(R_{\max}/\mathrm{eV})$	χ^2/ndf
uniform	-2.6	20.1	397.7 / 19
SFR	-2.4	20.0	282.8 / 19
quasars	-2.2	19.8	531.0 / 19

Table 5.11: Same as Tab. 5.10 but with a fit done for $E > 10^{18}\,\mathrm{eV}$.

	α	$\lg(R_{\max}/\mathrm{eV})$	H	He	N	Fe	χ^2/ndf
uniform	-1.9	19.7	0.0	0.0	74.5	25.5	193.4 / 26
SFR	-1.6	19.6	0.0	0.0	46.8	53.2	272.6 / 26
quasars	-1.3	19.8	0.2	0.0	0.0	99.8	439.6 / 26

Table 5.12: Same as Tab. 5.10 but with a combined fit of the spectrum, $\langle X_{\max}\rangle$ and $\sigma(X_{\max})$ and the HHeNFe source composition scenario used for the simulations.

protons from pair production and hence a more prominent pair production dip which fits better the data. But still a high maximum rigidity is needed to ensure enough low energy cosmic rays which still leads to a worse fit than in case of only considering cosmic rays above the ankle in the fit. In case of source distribution according to quasars the fit is even worse. Conclusively, also for more realistic source evolution scenarios the Beresinzky dip model seems to be disfavoured by the Auger data regarding the bad fit quality.

Related to this result, in Sec. 5.2.7 an additional nearby source population is introduced to an otherwise uniform source population which can be seen as a negative source evolution.

Comparison with other Studies The spectral indices agree with similar studies done by [93, 65], although $R_{\max}$ is not included in the fit performed in these works.

5.2.6 Magnetic Suppression

So far no influence of magnetic fields are considered in the propagation of the cosmic rays. As described in Sec. 2.3, extragalactic magnetic fields are already measured for some regions in the universe and predictions for the remaining space exist. These

	α	$\lg(R_{\mathrm{max}}/\mathrm{eV})$	H	He	N	Fe	χ^2/ndf
1)	$-0.2^{+0.1\ +0.0}_{0.1\ -0.0}$	$18.4^{+0.0\ +0.0}_{0.0\ -0.0}$	$63.9^{+5.9\ +5.7}_{5.9\ \ 0.0}$	$13.1^{+2.6\ +0.0}_{2.6\ -1.2}$	$22.8^{+4.4\ +0.0}_{4.4\ -4.5}$	$0.2^{+0.0\ +0.1}_{0.0\ -0.1}$	110.4 / 27
2)	$-1.7^{+0.1\ +0.0}_{0.1\ -0.4}$	$19.2^{+0.1\ +0.8}_{0.1\ \ 0.0}$	$29.1^{+8.1\ +0.0}_{8.1\ -29.1}$	$0.0^{+1.4\ +5.4}_{1.4\ \ 0.0}$	$52.5^{+7.1\ +26.6}_{7.1\ \ 0.0}$	$18.4^{+0.0\ +2.3}_{0.0\ \ 0.0}$	177.8 / 27

Table 5.13: Same as Tab. 5.2 but considering the effects of IGMF on the cosmic ray propagation as parameterized by [168] with $E_c = 10^{18}\,\mathrm{eV}$ and $X_s = 1$ as introduced in the text.

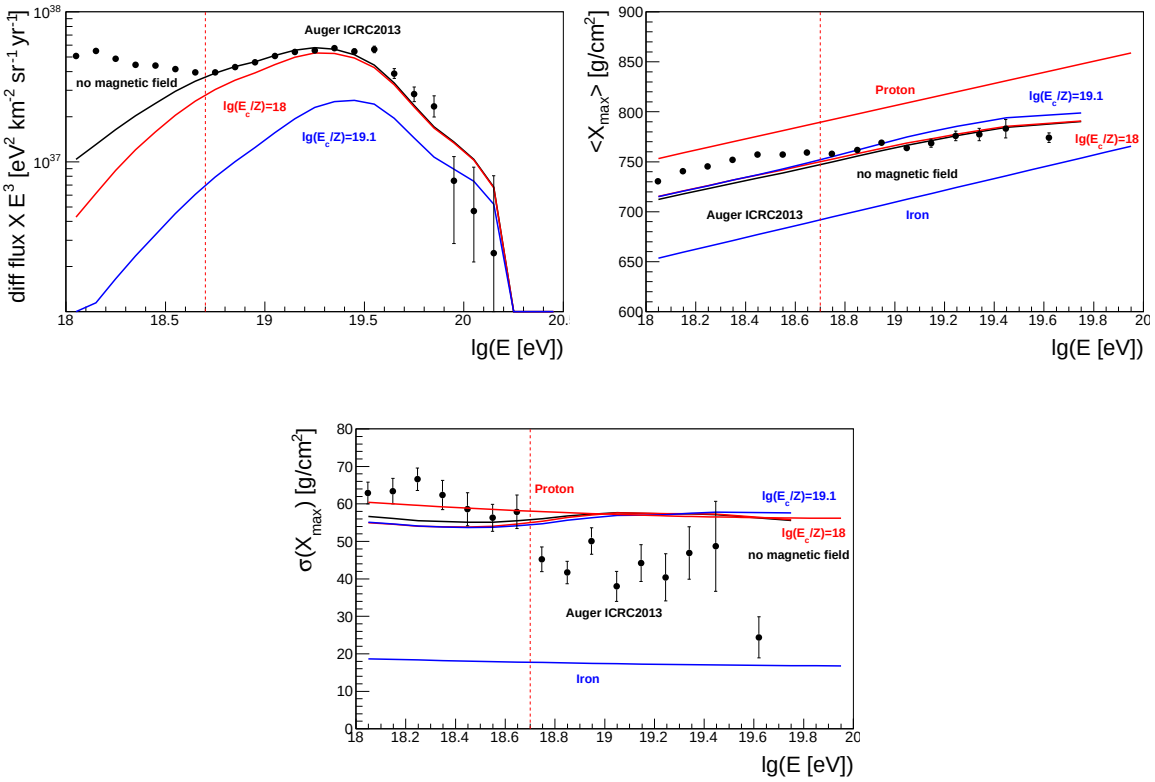

Figure 5.14: Energy spectrum, $\langle X_{\max} \rangle$ and $\sigma(X_{\max})$ for different strength of the magnetic suppression as described in the text assuming a HHeNFe source composition. Parameters are taken from the combined fit with the simulation without magnetic field and with $\alpha < -1$.

fields lead to a prolongation of the propagation time. This magnetic diffusion effect causes a suppression of the cosmic ray flux which increases for decreasing energies. In the one dimensional mode of CRPropa magnetic diffusion is not considered. To study this effect the following parametrization of the suppression factor

$$G(x) = \exp\left[-\frac{(aX_{\mathrm{s}})^{\alpha}}{x^{\alpha} + bx^{\beta}}\right]$$

with

$$X_s \equiv \frac{d_{\mathrm{s}}}{\sqrt{R_H l_{\mathrm{c}}}} \simeq \frac{d_{\mathrm{s}}}{65\,\mathrm{Mpc}} \sqrt{\frac{\mathrm{Mpc}}{l_{\mathrm{c}}}}$$

derived by Mollerach at al. [168] is used. Here $x = E/(Z \cdot E_{\mathrm{c}})$ contains the critical energy E_{c} at which the coherence length l_{c} of the magnetic field is equal to the Larmor radius. d_{s} is the average distance between sources and a, b, α and β are parameters derived in [168]. This result is only derived assuming $R_{\max} = 4 - 10\,\mathrm{EeV}$. This is valid for the first minimum in the HHeNFe scenario. For the second one the maximum

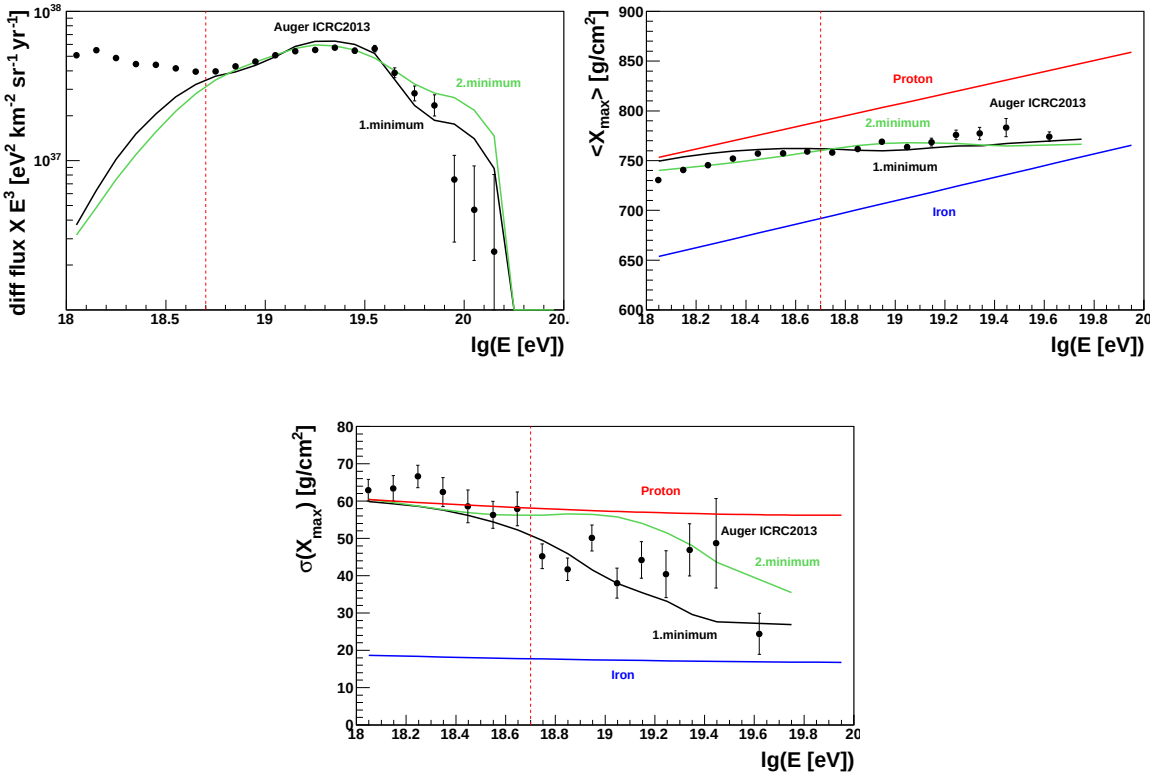

Figure 5.15: Same as in Fig. 5.7 but with considering flux suppression effects due to EGMF as described in the text with suppression parameters $E_\mathrm{c} = 10^{18}\,\mathrm{eV}$ and $X_\mathrm{s} = 1$.

rigidity is slightly above this value. Here this analytic result has to be seen as an approximation.

Throughout this section $X_\mathrm{s} = 1$ will be used which is given as a reasonable assumption in [168]. Further, $l_\mathrm{c} = 1\,\mathrm{Mpc}$ which is an often used assumption [168], leads to a source density of $3.6 \cdot 10^{-6}/\mathrm{Mpc}^{-3}$. In Fig. 5.14 the impact of varying E_c/Z within $10^{17.5}$–$10^{19.1}\,\mathrm{eV}$ is studied. These values correspond to a magnetic field of 0.34–15 nG, which are the mean magnetic field values from different LSS simulations as already mentioned in Sec. 2.2. These values lie well below the upper limits of $0.3\,\mu\mathrm{G}$ found for intergalactic magnetic fields [77]. The effect on the X_max moments are moderate compared to the effect on the spectrum that range from nearly no suppression for the lowest magnetic fields up to an attenuation of one order of magnitude at low energies for the strongest magnetic fields.

Fit with Medium Magnetic Diffusion Effect The fit is now redone assuming an intermediate critical energy of $Z \cdot E_\mathrm{c} = 10^{18}\,\mathrm{eV}$ which also is used in [168] and corresponds to a magnetic field strength of 1.1 nG. According to the results without magnetic field consideration shown in Sec. 5.2.2 two minima are found which are listed

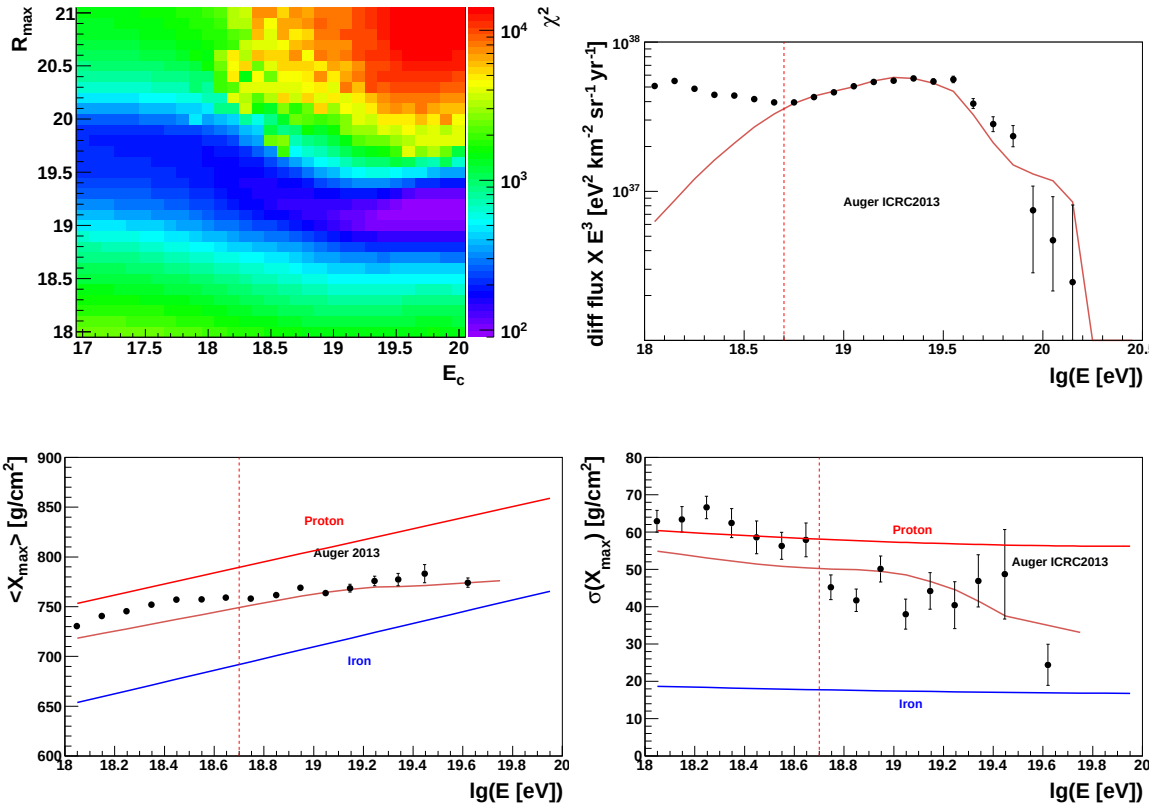

Figure 5.16: Same as in Fig. 5.15 but with a fixed spectral index of $\alpha = -2$ and E_c included in the combined fit. **Top left:** The fit quality χ^2 for a scan of the maximum rigidity at the sources and the critical energy E_c which controls the strength of the magnetic flux suppression as described in the text.

in Tab. 5.13. Compared to the fit without magnetic fields the first minimum, which is now at $\alpha = -0.2$, shows a softer source spectrum whereas the second minimum at $\alpha = -1.7$ has a harder spectrum and an increased proton component. The softer source spectrum for the first minimum increases the low energetic particle with respect to the high energetic and hence the suppression from magnetic fields can be compensated. In case of the second minimum the flux decrease at low energies is compensated by increasing the proton fraction at source which also allows a harder spectral index and lower maximum rigidity. The latter change allows a better description of the $X_{\max}$ moments which can be seen in Fig. 5.15. For both maxima an improvement of the fit quality can be observed.

Fitting the Strength of the Magnetic Diffusion Finally a spectral index of $\alpha = -2$ is forced as expected by the classic Fermi acceleration and the strength of the magnetic suppression is fitted by regarding E_c as a fit parameter. The result as shown in Tab. 5.14 and Fig. 5.16 is an even better fit with $\chi^2/ndf \approx 3.4$ compared

	$\lg(E_c/\mathrm{eV})$	$\lg(R_{\max}/\mathrm{eV})$	H	He	N	Fe	χ^2/ndf
	19.7	19.1	9.8	0.0	81.4	8.8	91.8 / 27
$Z \cdot E_c < 10^{19.1}$	19.1	19.1	17.6	0.0	70.1	12.3	115.2 / 27

Table 5.14: Same as Tab. 5.13 but for fixed $\alpha = -2$ and including E_c in the fit.

to the first minimum without considering magnetic fields with $\chi^2/ndf \approx 5$ as shown in Sec. 5.2.2. For this result the critical energy of $E_c = 10^{19.7}\,\mathrm{eV}$ is needed which translates to a very high magnetic field of $B = 55\,\mathrm{nG}$ exceeding the higher bound from LSS simulation of 15 nG. Constraining the fit to this upper bound for magnetic field by choosing $E_c = 10^{19.1}\,\mathrm{eV}$ leads to $\chi^2/ndf \approx 4.2$ which is still an improvement to the first minimum of Sec. 5.2.2. In general the influence of the magnetic field due to this analytic expression are stronger as for example expected from 3d simulations including cosmological effects as done by [174]. For this reason the results of this section are not considered in chapter 7.

Comparison with other Studies The improvement of fit quality due to magnetic diffusion effect shown here is also concluded by Mollerach et al. [168] and Taylor et al. [152, 165] although not a systematic fit is performed in these publications.

5.2.7 Study with Additional Source Populations

Up to now one population of sources with equal properties is assumed. Some features in the data of the Pierre Auger Observatory cannot be described with this assumption. In this section, additional source populations are introduced to achieve a better agreement with the data. Two different motivations for this procedure are discussed. These scenarios are based on the standard scenario with the HHeNFe composition as introduced in Sec. 5.2.2 with uniform sources and no consideration of magnetic fields.

Additional Proton Component The first motivation arises from the fact that the data from the Pierre Auger Collaboration indicates a special feature of the $\langle X_{\max}\rangle$ and $\sigma(X_{\max})$ evolution with energy. Despite an overall decreasing of this two observables with increasing energy above $\sim 10^{18.2}\,\mathrm{eV}$ a weakening of this decrease is seen around $\sim 10^{19.3}\,\mathrm{eV}$. This feature is caused due to some deeply penetrating showers around $10^{19.5}\,\mathrm{eV}$. As seen in Sec. 5.2.2 the first minimum in the fit for the four component scenario can roughly reproduce the $X_{\max}$ momenta, but omitting this special feature. This feature is not possible to be reproduced by one source population where all sources have the same properties.

As the observed feature indicates a lightening of the composition for intermediate energies, an additional proton component seems to be a natural choice to approximate this behavior. At first, this proton sources are assumed uniform corresponding to the mixed sources. As energy losses due to propagation effects would reduce the proton component at energies above the GZK cut-off also a scenario with near proton source

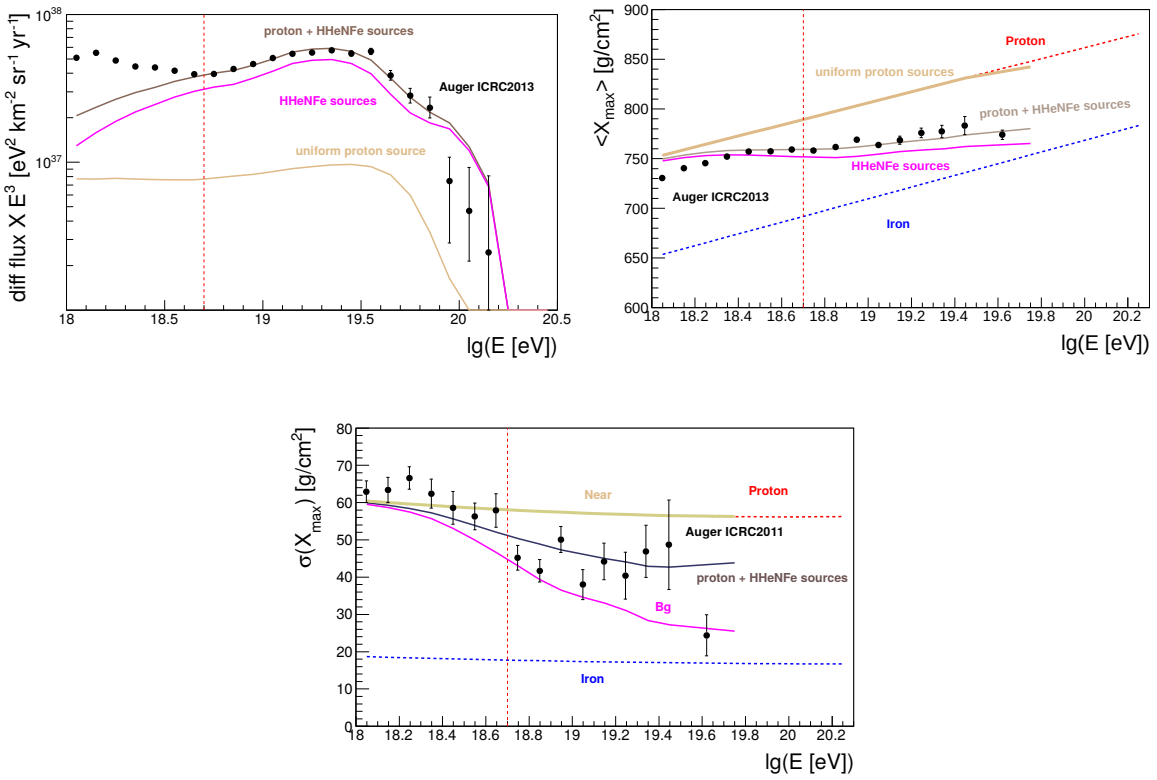

Figure 5.17: Same as in Fig. 5.7 but assuming an additional uniform proton source population in the simulation. The energy spectrum, $\langle X_{\mathrm{max}} \rangle$ and $\sigma(X_{\mathrm{max}})$ are displayed individually for the proton and HHeNFe sources as well as for the sum of these two populations. The source parameters are according to the first minima of the combined fit.

at 4 Mpc is tested allowing a more targeted lightening of the observed composition. The latter scenario obviously can also be interpreted as a number of near sources instead of one single source. The proton source population in both scenarios have an individual spectral index and maximum rigidity. This is necessary to achieve an increased proton component at higher energy.

For the additional uniform proton sources the relative abundance is scaled with s_{proton}. A value of $s_{\mathrm{proton}} = 1$ corresponds to same amount of emitted primaries at the mixed sources and the additional proton sources at a reference energy of 10^{18} eV. The scaling factor s_{proton} along with the spectral index α_{proton} and maximum rigidity $R_{\mathrm{max}}^{\mathrm{proton}}$ at the additional proton sources are additional fit parameters. The ranges for the new parameters are $\alpha_{\mathrm{proton}} \in [-3, 0.4]$, for $\lg(R_{\mathrm{max}}^{\mathrm{proton}}/\mathrm{eV}) \in [18.4, 22.4]$ and for $s_{\mathrm{proton}} \in [0, 100]$. The resulting parameters from the fit are listed in Tab. 5.15. As one can see in Fig. 5.17 the $\langle X_{\mathrm{max}} \rangle$ and $\sigma(X_{\mathrm{max}})$ evolution are better described now. As a result the quality of the fit improves in comparison to the four component scenario without additional proton component from $\chi^2_{\mathrm{min}}/ndf = 5.1$ to $\chi^2_{\mathrm{min}}/ndf = 3.2$. For

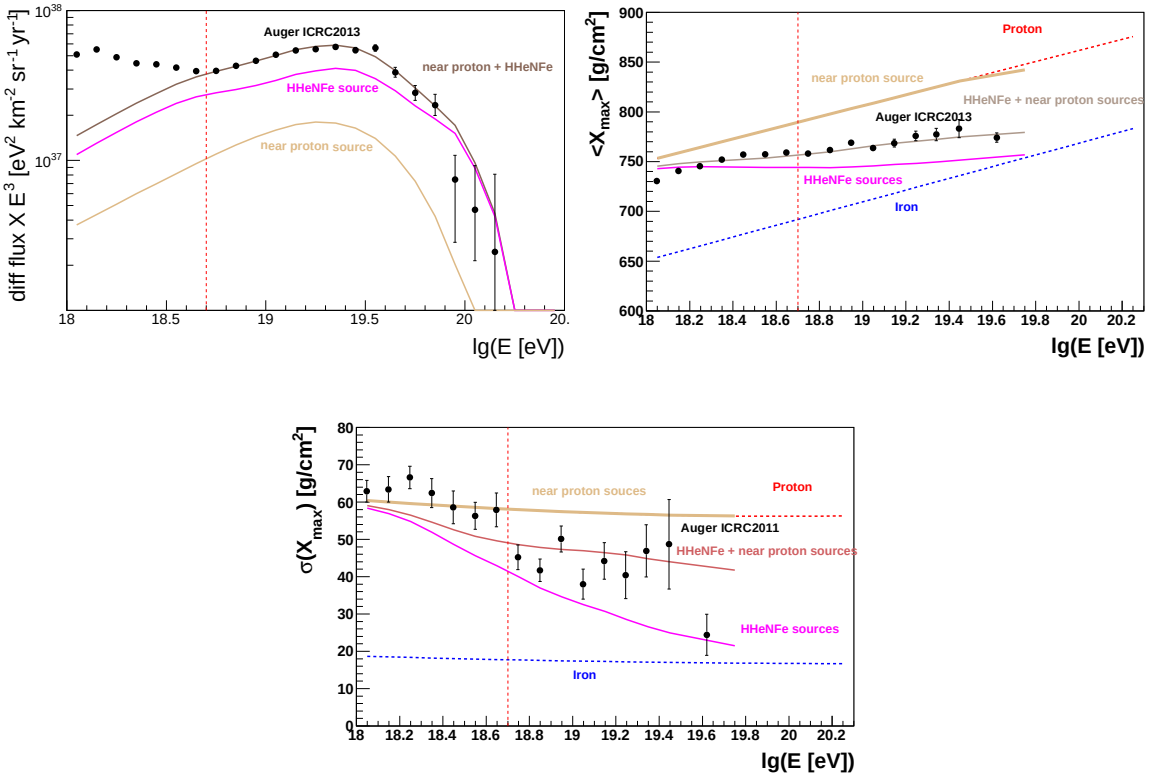

Figure 5.18: Same as in Fig. 5.7 but assuming an additional near proton source population at a disatnce of 4 Mpc in the simulation. The energy spectrum, $\langle X_{\mathrm{max}} \rangle$ and $\sigma(X_{\mathrm{max}})$ are displayed individually for the near proton and HHeNFe sources as well as for the sum of these two populations. The source parameters are according to the first minima of the combined fit.

the best fit the background sources have still an extreme spectral index of $\alpha = 0.0$, a very low maximum rigidity of $R_{\mathrm{max}} = 10^{18.3}$ eV and a light source composition as already seen for the best fit without the near source. One should note that with $\alpha_{\mathrm{near}} = -2.2$ the spectral index for the proton source is in good agreement to spectral index predicted from Fermi acceleration. As expected, $R_{\mathrm{max}}^{\mathrm{proton}} > R_{\mathrm{max}}$ is found for the fit. For the best fit a high luminosity of the proton sources with $s_{\mathrm{proton}} = 29.6$ is needed.

The flux of the nearby source is scaled for all energies relatively to the mixed sources with the scale factor $s_{\mathrm{near}}^{\mathrm{proton}}$ in a way such that $s_{\mathrm{near}}^{\mathrm{proton}} = 1$ corresponds to the near source emitting the same amount of particles at the energy of 10^{18} eV as one of the background sources. Here a source density of $\rho_{\mathrm{src}} = 2.69 \cdot 10^{-4}\,\mathrm{Mpc}^{-3}$ is assumed for the background sources. This density corresponds to the AGN given in the Véron-Cetty and Véron Catalog [122] within 75 Mpc to the Earth and will be used in chapter 7 for studies referring to arrival directions. The results in Fig. 5.18 and Tab. 5.16 show that with $\chi^2_{\mathrm{min}}/ndf = 2.1$ the best result is achieved for this scenario. Even in the second

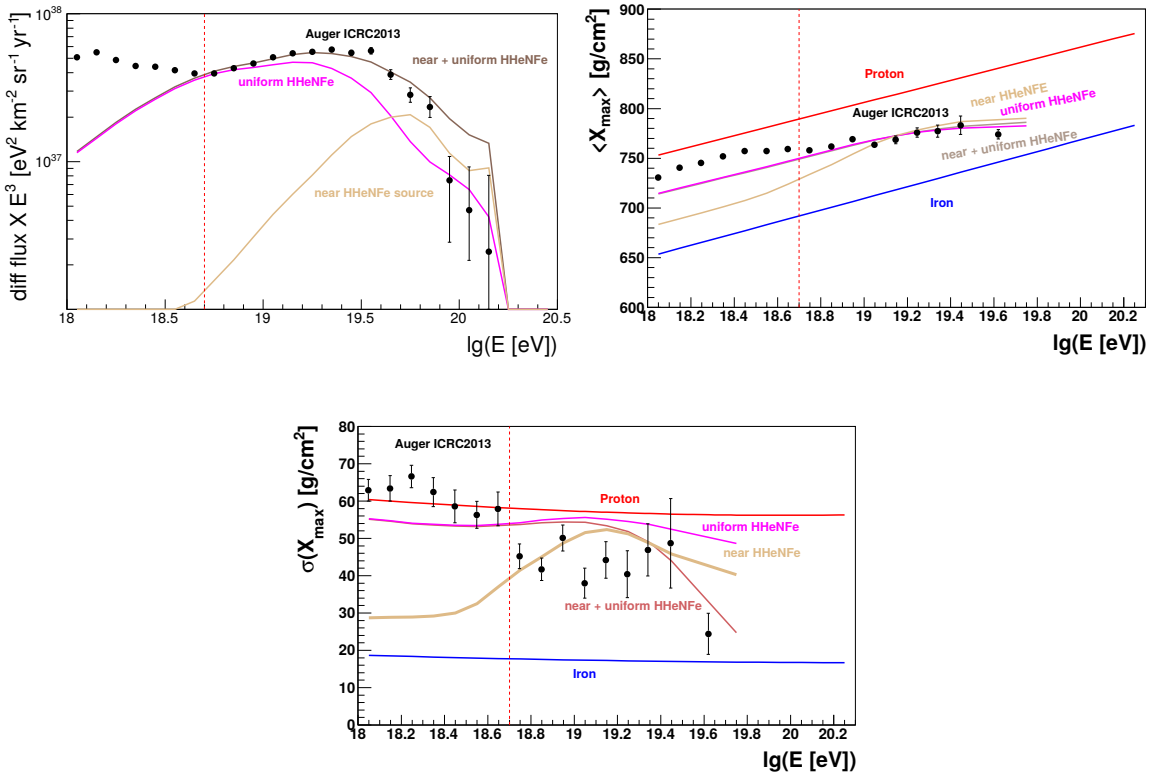

Figure 5.19: Same as in Fig. 5.7 but assuming an additional near HHeNFe source population at a distance of 4 Mpc in the simulation. The energy spectrum, $\langle X_{\mathrm{max}} \rangle$ and $\sigma(X_{\mathrm{max}})$ are displayed individually for the near and uniform HHeNFe sources as well as for the sum of these two populations. The source parameters are according to the first minima of the combined fit.

minimum a good fit is achieved compared to the four component scenario without additional proton sources which can not be achieved with an additional uniform proton population.

Additional Nearby Mixed Sources A second motivation for an additional source is the bad $\sigma(X_{\mathrm{max}})$ agreement seen in the fit in Sec. 5.2.2 demanding an α compatible with Fermi acceleration. A lighter mass composition is seen compared to the Auger data. As mainly heavy particles are injected these lighter nuclei are produced in interactions during the propagation. One way to reduce this secondary cosmic rays is to introduce a nearby source at 4 Mpc distance. The source composition, spectral index and maximum rigidity are chosen according to the uniform HHeNFe scenario. The relative flux of the near source is scaled to the uniform sources with the parameter $s_{\mathrm{near}}^{\mathrm{HHeNFe}}$. As in the previous study $s_{\mathrm{near}}^{\mathrm{HHeNFe}} = 1$ corresponds to the same amount of cosmic rays being emitted at the energy of 10^{18} eV from the near source as from one of the uniform sources at the same energy. The fit results as listed in Tab. 5.17 are

very similar to the results for the second minimum assuming uniform sources despite that the fit quality improves to $\chi^2_{\mathrm{min}}/ndf = 4.7$ from $\chi^2_{\mathrm{min}}/ndf = 7.1$. The presence of a near source with $s^{\mathrm{HHeNFe}}_{\mathrm{near}} = 1.4$ contributes mainly to the flux at the highest energies and is able to reduce the $\sigma(X_{\mathrm{max}})$ values to enable a better agreement with Auger data as seen in Fig. 5.19. A minimum at very hard spectral indices is not found for this scenario.

In general the results for these additional nearby sources can be seen as an indication of a local source over-density and can also be related to an negative evolution of sources in contrast to the positive evolution studied in Sec. 5.2.5.

Comparison with other Studies This result agrees with those in [175] where it is shown that hard spectral indices can be avoided for a mixed composition scenarios by using a negative cosmological evolution. A physical motivation for such a source evolution could be given by measurements of low-luminosity BL Lac objects [176].

α	$\lg(R_{\max}/\mathrm{eV})$	H	He	N	Fe	α^{proton}	$\lg({}^{\mathrm{proton}}R_{\max}/\mathrm{eV})$	s^{proton}	χ^2/ndf
$-0.0^{+0.0\ +0.0}_{0.0\ -0.0}$	$18.3^{+0.0\ +0.0}_{0.0\ -0.0}$	$31.0^{+2.8\ +19.0}_{2.8\ -0.0}$	$43.0^{+4.2\ +0.0}_{4.2\ -14.2}$	$25.7^{+2.6\ +8.6}_{2.6\ -11.8}$	$0.3^{+0.0\ +0.0}_{0.0\ -0.1}$	$-2.5^{+0.1\ +0.0}_{0.1\ -0.1}$	$19.8^{+0.1\ +0.3}_{0.1\ -0.1}$	$29.6^{+7.3\ +9.6}_{7.3\ -7.5}$	77.8 / 24
$-1.8^{+0.1\ +1.8}_{0.1\ -0.1}$	$19.4^{+0.2\ +0.1}_{0.2\ -1.1}$	$4.3^{+71.8\ +0.0}_{71.8\ -4.3}$	$0.0^{+2.1\ +83.0}_{2.1\ -0.0}$	$67.1^{+17.8\ +10.2}_{17.8\ -51.8}$	$28.6^{+0.0\ +0.0}_{0.0\ -28.3}$	$-2.2^{+0.3\ +0.2}_{0.3\ -0.1}$	$20.1^{+0.5\ +0.0}_{0.5\ -1.2}$	$0.4^{+0.4\ +11.8}_{0.4\ -0.4}$	193.6 / 24

Table 5.15: Same as Tab. 5.2 but with an additional uniform proton source population which also introduces additional parameters as specified in the text.

α	$\lg(R_{\max}/\mathrm{eV})$	H	He	N	Fe	$\alpha^{\mathrm{proton}}_{\mathrm{near}}$	$\lg({}^{\mathrm{proton}}R^{\mathrm{near}}_{\max}/\mathrm{eV})$	$s^{\mathrm{proton}}_{\mathrm{near}}$	χ^2/ndf
$0.1^{+0.1\ +0.1}_{0.1\ -0.1}$	$18.1^{+0.0\ +0.1}_{0.0\ -0.0}$	$62.5^{+0.3\ +0.7}_{0.3\ -2.1}$	$31.3^{+0.2\ +3.6}_{0.2\ -4.1}$	$6.1^{+0.4\ +3.4}_{0.4\ -1.4}$	$0.1^{+0.0\ +0.0}_{0.0\ -0.0}$	$-2.3^{+0.1\ +0.0}_{0.1\ -0.1}$	$19.3^{+0.0\ +0.1}_{0.0\ -0.0}$	$32.3^{+3.4\ +4.9}_{3.4\ -0.0}$	49.3 / 24
$-1.2^{+0.0\ +0.0}_{0.0\ -0.0}$	$18.5^{+0.1\ +0.0}_{0.1\ -0.0}$	$1.8^{+3.5\ +0.3}_{3.5\ -1.8}$	$28.4^{+20.1\ +54.5}_{20.1\ -23.1}$	$62.3^{+19.1\ +23.1}_{19.1\ -49.5}$	$7.5^{+0.0\ +0.0}_{0.0\ -3.2}$	$-2.4^{+0.1\ +0.1}_{0.1\ -0.0}$	$19.3^{+0.0\ +0.1}_{0.0\ -0.1}$	$37.1^{+24.2\ +0.0}_{24.2\ -25.3}$	71.5 / 24

Table 5.16: Same as Tab. 5.15 but with additional nearby proton sources at 4 Mpc instead of uniform proton sources.

α	$\lg(R_{\max}/\mathrm{eV})$	H	He	N	Fe	$s^{\mathrm{HHeNFe}}_{\mathrm{near}}$	χ^2/ndf
$-1.9^{+0.0\ +0.0}_{0.0\ -0.2}$	$19.5^{+0.0\ +0.0}_{0.0\ -0.2}$	$0.0^{+1.3\ +22.1}_{1.3\ -0.0}$	$0.0^{+10.0\ +55.6}_{10.0\ -0.0}$	$85.6^{+1.9\ +0.0}_{1.9\ -58.2}$	$14.4^{+0.0\ +0.0}_{0.0\ -8.9}$	$0.5^{+0.1\ +1.7}_{0.1\ -0.0}$	123.3 / 26

Table 5.17: Same as Tab. 5.15 but with a nearby HHeNFe source instead of near proton sources.

5.2.8 Scenario Variable Source Spectral Index

In the previous sections mostly the simple assumption of equal spectral indices for all sources is made. Different possible candidates like AGNs, GRBs or pulsars are assumed which prefer different spectral indices as already described in Sec. 2.1.5. Additionally, the properties of possible acceleration sites from one source candidate should alter the spectral index. In the last section we already used proton sources with different source spectra than for mixed composition sources. In this section a scenario with non uniform spectral index distribution is studied. For this purpose cosmic rays are emitted at 100 equidistant source distances from 4 Mpc to 2600 Mpc. The spectral index of each source distance is taken from a Gauss distribution with a mean value of μ_α and a spread of σ_α.

μ_α is used in the fit instead of α and three scenarios with σ_α =0.2, 0.4 and 0.6 are tested.

The assignment of the spectral indices to the different source distances has an impact on the results. To take this into account 60 realizations are performed for each of the three scenarios. The average and the RMS for the best fit scenarios from the 60 realizations are shown in Tab. 5.18.

For $\sigma_\alpha = 0.2$ no significant change in the fit results can be seen when comparing with the mean of the results of the 60 realizations. For the scenarios with higher variations of the spectral index the fit gets worse for most realizations. Also an increasing variation between the single realizations can be observed. This behavior is obvious as larger differences in the spectral index are possible. Note that for this study simulations with the old Talys 1.0 are performed and the $\langle X_{\mathrm{max}} \rangle$ and $\sigma(X_{\mathrm{max}})$ parametrization with Epos 1.99 instead of Epos LHC is used.

5.3 Summary and Conclusion

In this chapter a variety of astrophysical scenarios are studied on their ability to mimic the energy spectrum and X_{max} moments measured by the Pierre Auger Collaboration. For each scenario predictions for these cosmic ray properties obtained with the Monte Carlo code CRPropa are fitted to the data above the ankle of the cosmic ray spectrum at $10^{18.7}$ eV. This procedure constraints the potential sources with respect to the spectral index of the energy spectrum, the maximum rigidity and the relative abundances of elements. In the beginning three composition scenarios are tested for a set of standard assumptions which are continuous uniform sources, no magnetic field and an infrared photon background from Kneiske et al. [2]. Pure proton sources are only able to predict a reasonable energy spectrum but are not able to reproduce the measurements of the X_{max} moments. Furthermore the reproduction of the energy spectrum down to 10^{18} eV as assumed by the pair production dip model for proton dominated sources is not possible with the current high precision measurements of the energy spectrum.

The two mixed composition scenarios HHeNFe and GCRSC allow also a descrip-

	μ_α	$\lg(R_{\max}/\mathrm{eV})$	H [%]	He [%]	N [%]	Fe [%]	χ^2/ndf
$\sigma_\alpha = 0.2$	-2.0 ± 0.1	19.2 ± 0.2	7.9 ± 13.1	0.5 ± 2.8	70.6 ± 13.0	17.9 ± 4.6	$165 \pm 22/27$
$\sigma_\alpha = 0.4$	-2.0 ± 0.4	19.1 ± 0.4	2.3 ± 4.3	5.7 ± 15	75.5 ± 24.2	13.8 ± 9.4	$249 \pm 110/27$
$\sigma_\alpha = 0.6$	-2.0 ± 0.5	18.9 ± 0.4	3.6 ± 6.4	2.5 ± 9.1	81.6 ± 18.9	11.1 ± 10	$311 \pm 157/27$
no variation	-1.9	19.2	12.2	0	68.5	19.3	179 /27

Table 5.18: Results derived by a combined fit of the energy spectrum, $\langle X_{\max} \rangle$ and $\sigma(X_{\max})$ from simulations to the data from the Pierre Auger Observatory [95]. 100 point sources each with an own spectral index which are in total Gaussian distributed are simulated. Different fixed spreads σ_α are used and the mean spectral index μ_α is fitted. 60 realizations are done for each σ_α scenario where the mean and the RMS of the results are shown in the table. The results are compared to the corresponding scenario without variation of α.

tion of the X_{max} data although the fit quality is still not convincing. In both mixed composition cases two minima are found in the fit according to a hard spectral index $\alpha \in [-1, 0]$ and low maximum rigidities $R_{\mathrm{max}} \in [10^{18.4}, 10^{18.6}]$ eV for the one minimum and a 'Fermi-like' spectral index $\alpha = -1.9$ and a higher maximum rigidity $R_{\mathrm{max}} = 10^{19.7}$ eV for the other. These two mixed composition scenarios can not be distinguished by the quality of the fit to the data. Furthermore, it is shown that for the proton composition as well as for the mixed HHeNFe composition scenario a high energy flux suppression only caused by the energy losses during the extragalactic propagation is not sufficient to describe the data.

Subsequently, the impact of the source evolution and of the magnetic field are studied. Assuming a source evolution according to the star formation rate and quasars show in most cases a worse description of the data. Only for the disfavoured proton sources in the dip model scenario an improvement of the fit for a SFR scenario is seen. Taking into account effects of magnetic fields by corrections from analytic calculations by Molerach et al. [168] show a clear improvement of the fit to data. It was also possible to fix the spectral index to $\alpha = -2$ as predicted by shock acceleration scenarios and fit the magnetic field strength. Although this yields very high magnetic field strength an even better fit quality can be achieved as in the first maximum without magnetic field. However, compared to a more sophisticated treatment of the effect of magnetic fields, as possible in 3d-simulations that consider the expansion of the universe, the here used analytic results seem to yield a too strong flux suppression.

Furthermore, also some additional source populations are introduced to the standard HHeNFe scenario. This is motivated by theoretical predictions of cosmic ray source candidates as well as some special features of the X_{max} data. Here, proton sources at a distance of 4 Mpc improve the fit quality allowing a better description of special features of the X_{max} moments. Also an improvement is achieved with an additional population of mixed HHeNFe sources at 4 Mpc distance that improves the fit to the X_{max} data. This improvement can be explained due to the fact, that for the contribution of the near source a lower production of secondaries is yield. In this scenario also a result with a extreme hard spectral index can be avoided.

Finally, a distribution of spectral indices among the sources is tested which is not favoured by the combined fit.

Summarised, pure proton sources are disfavoured in general. Mixed compositions allow a better description of the data, whereas effects from extragalactic magnetic fields and near source population provide the best predictions from astrophysical scenarios to the data.

6 Secondary Photons and Neutrinos

In this chapter UHE photon and neutrino fluxes are discussed which are produced as secondaries during cosmic ray propagation. Although not detected yet, the observation of cosmic rays above 10^{20} eV demands the existence of these secondaries and the search for these particles is an important part of current astroparticle physics. CRPropa [2] is an excellent tool to predict the expected fluxes for these additional messengers as well as to conclude on sources of cosmic rays due to the absence of these secondary fluxes. Both cases will be addressed in this chapter and the discrimination power of UHE photons and neutrinos referred to parameters of the astrophysical scenarios will be compared to each other.

6.1 Study on Photon Flux

As described in Sec. 3.3.3 the non-observation of photons already leads to the exclusion of many top-down cosmic ray source models. The observation of photons would provide better directional information on the sources, as photons point back to their sources. As UHE photons have only a small energy loss length compared to cosmic ray nuclei or neutrinos the flux of photons would supply an information on the source distribution in the nearby universe. In this section the photon flux will be discussed starting with a general study of the importance of different parameters of the potential cosmic ray sources and the astrophysical environment. After explaining the basic dependencies, a prediction is made assuming reasonable parameter ranges defined by astrophysical considerations and experimental data. Furthermore, the possibility is tested to constrain the parameters of the scenarios with current experimental limits on the UHE photon flux and fraction as well as with future sensitivities. The contribution of the secondary photon flux to the observed fluxes of GeV photons as well as the consideration of dominant nearby sources are studied. At the end of the section the impact of an additional photon flux produced directly in the vicinity of the sources is studied.

6.1.1 Simulation Setup

As in chapter 5, 1d cosmic ray simulations are performed assuming continuous sources up to 2800 Mpc. More distant sources do not contribute to the photon flux as showed in Sec. 6.1.2. A pure proton and a pure iron composition with a power-law energy spectrum and a rigidity dependent cosh cut-off as used in chapter 5 are assumed. The absolute normalization of the photon flux is taken from the normalization of the cosmic ray flux to the Auger data [95] at 10^{19} eV. As described in Sec. 4.1 the electromagnetic

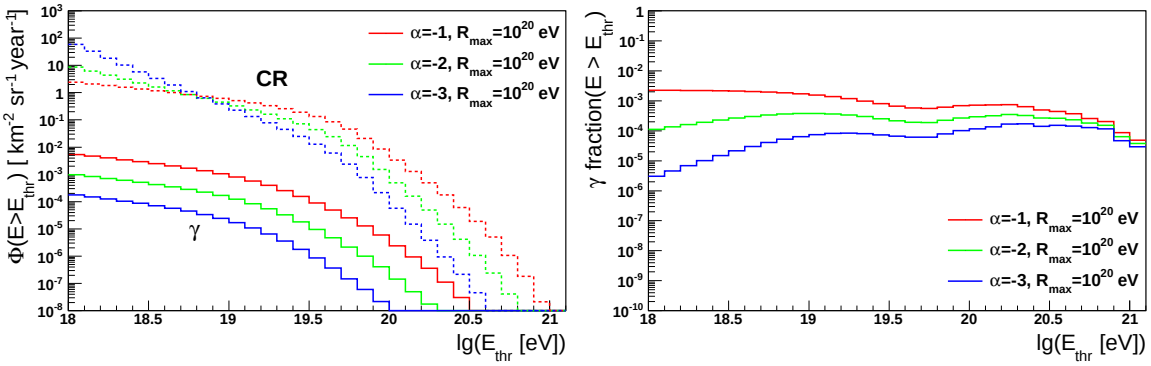

Figure 6.1: Integral photon flux and cosmic ray flux (left) as well as the integral photon fraction (right) as function of the energy threshold E_{thr}. The influence of α is displayed for a standard scenario assuming pure proton sources as specified in the text.

cascades in 1d simulation are collectively propagated. Hence, no information on the mother particle is stored in the simulation. To do a reweighting of the photon energy spectrum, as done in the previous chapter, cosmic rays are simulated at discrete energies with step size of $\Delta \log E_{\mathrm{src}} = 0.1$. The comparison to simulations without this discretization of source energies do not show a significant deviation of the photon flux with respect to the discrete procedure.

6.1.2 Parameter Studies

The production of UHE photons as well as their extragalactic propagation are influenced by a wide range of parameters. In the following, the dependence of the photon flux and fraction on the succeeding source properties is studied:

- energy spectrum,
- maximum rigidity,
- maximum distance of the sources to Earth,
- the evolution of the sources with redshift,

as well as attributes of the intergalactic space:

- radio background and
- magnetic fields.

For this purpose a benchmark scenario with proton sources uniformly distributed up to 2800 Mpc, an energy spectrum with $\alpha = -2$ up to a rigidity of $R_{\mathrm{max}} = 10^{20}$ eV, the infrared background photon field by Kneiske et al. [2], a weak radio background field

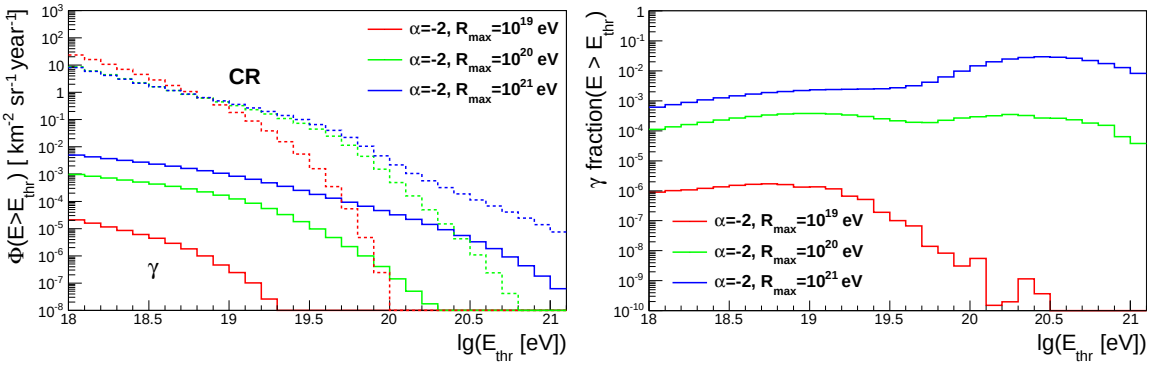

Figure 6.2: As in Fig. 6.1 but displaying the influence of $R_{\max}$

by Protheroe et al. [177] and no magnetic fields are chosen. Based on this benchmark scenario one parameter of the astrophysical scenario will be altered at once to study it's specific impact on the photon flux. Note that the benchmark scenario is selected to help comparing the influence of different parameters of the scenario rather than considered to be the most realistic one.

Spectral Index Increasing the source spectral index from $\alpha = -3$ to $\alpha = -1$ shows an increase in the integral photon flux of nearly two orders of magnitude which is uniform for the whole energy range above 10^{18} eV as shown in the left plot in Fig. 6.1. A power law energy spectrum with a higher spectral index causes an increase of the contribution of high energy source protons which are the main origin of the photons flux. This results in an increase in the overall photon flux for all energies as protons with $E < 10^{19.7}$ eV do not significantly contribute to the photon flux. A harder spectral index at source causes also a higher observed cosmic ray flux at higher energies but a decreased flux at low energies. Conclusively, the integral photon fraction has a large increase with a hardening spectrum at lower energies and a weaker increase at higher energies.

Maximum Rigidity The increase in the the maximum rigidity from 10^{19} eV to 10^{21} eV causes an increase in photon flux and in photon fraction as seen in Fig. 6.2. This increase is seen at most for higher observed energies in case of the photon flux as well as for the cosmic ray flux. The development of the photon fraction with energy indicates an even stronger effect on the photon flux at the highest energies. This can be explained as for the highest relevant energies the energy loss length for photons increases while those for protons decreases as seen in Fig. 2.9.

Maximum Distance of Sources To study the source distance dependence of the photon flux uniformly distributed sources from 4 Mpc up to different maximum source distances $D_{\max}$ between 4 Mpc and 3600 Mpc are compared. In Fig. 6.3 it can be seen

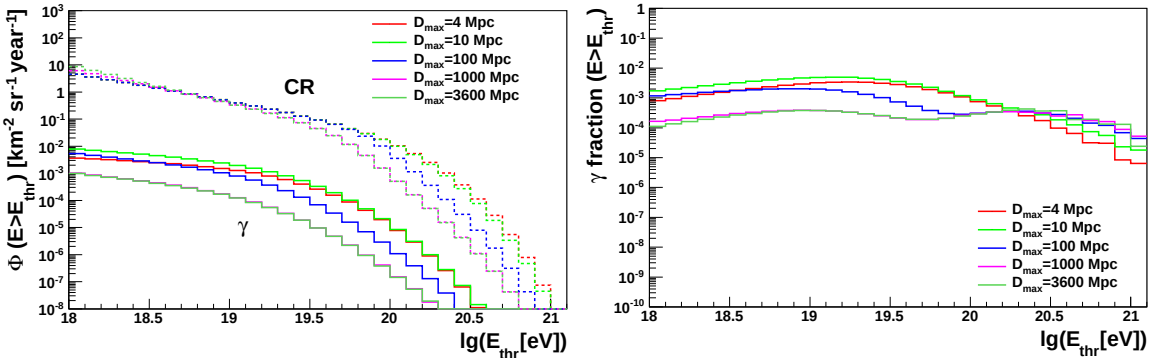

Figure 6.3: As in Fig. 6.1 but displaying the influence of the maximum distance $D_{\max}$ of the sources.

that the photon flux increases from 4 Mpc to 10 Mpc and subsequently decreases with increasing $D_{\max}$ up to $D_{\max} = 1000$ Mpc and remains unchanged for higher $D_{\max}$. As described in Sec. 2.4.2 the energy loss length for UHE photons is in the order of 10 Mpc for the energies studied here. Hence, the most photons come from nearby sources resulting in an increase of the photon flux for the two nearest $D_{\max}$. Cosmic rays from more distant sources increase mainly the observed cosmic ray flux which lead to a decrease of the photon flux due to the normalization procedure. Sources with a distance higher than 1000 Mpc do not contribute to the cosmic ray flux at the normalisation energy of 10^{19} eV and hence the photon flux remains unchanged for $D_{\max} > 1000$ Mpc. The energy loss length for nucleons is in the order of 10 Mpc above $\sim 10^{19.8}$ eV and strongly increases at lower energies up to the order of 1000 Mpc. Conclusively, the observed high energy protons arise from nearby sources whereas low energy protons also survive long travel distances. Because of this the cosmic ray spectrum shows with decreasing $D_{\max}$ a decrease for $E > 10^{19}$ eV and an increase for $E < 10^{18.5}$ eV. The photon fraction for energies up to $\sim 10^{20.3}$ eV increases from $D_{\max} = 4$ Mpc to $D_{\max} = 10$ Mpc and then decreases with increasing $D_{\max}$. At higher energies, where the decreasing cosmic ray flux over-compensates the decrease in the photon flux an increasing photon fraction is seen with $D_{\max}$.

Evolution of Sources Density As already described in Sec. 2.1.6, the evolution of the comoving source density with redshift z depends on the assumed cosmic ray source candidates. Different source evolution scenarios will be used to cover a reasonable physical range. The steepness of the increase of the source density with z increases from uniform sources over SFR [67] to quasars [69] for the here relevant propagated distances. The density evolution of other cosmic ray source candidates like gamma ray bursts show an intermediate increase with z relative to the latter two models as shown by Kotera et al. [65]. The uniform source evolution is considered, as it is frequently used for example by Taylor et al. [152] or Boncioli et al. [154] and is used in several sections in this thesis for example in Sec. 5.2.2. Hence, the uniform, the SFR and the

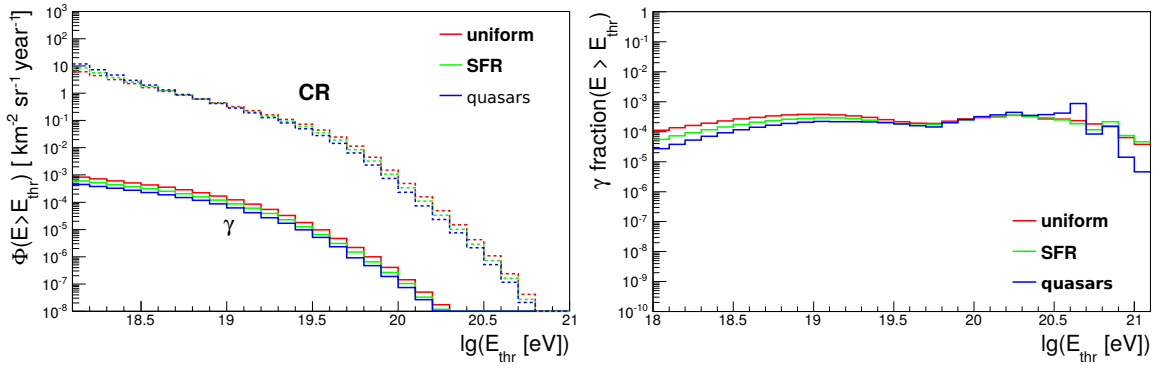

Figure 6.4: As in Fig. 6.1 but displaying the influence of the source evolution.

quasar evolution will be used.

Figure 6.4 displays a decrease of the photon flux with increasing steepness of the source evolution as it gives an increased weight to more distant sources which decreases the photon flux as already seen in the previous $D_{\max}$ study. According to the $D_{\max}$ study an increasing steepness of the source evolution yields a decrease of the cosmic ray spectrum at the highest energies and an increase at lower energies. Consequently the photon fraction increases for lower energies and is barely influenced at the highest energies by the source evolution. The difference is rather small compared to the influence of the source spectrum or maximum rigidity.

Radio Background For the study of the influence of the radio background on the photon flux a lower and a higher radio background from Protheroe et al. [177] is compared with the scenario with no radio background. In Fig. 6.5 a clear decrease of the photon flux and fraction is seen for an increasing radio background as photons with $E > 10^{19}\,\mathrm{eV}$ mainly lose energy in interaction with the radio background. It should be mentioned that the influence of the radio background increases with increasing maximum energy or harder source spectrum. No influence on the cosmic ray spectrum is seen as expected.

Magnetic Field Considering different magnetic fields the mean value from the two large scale structure simulations as introduced in 2.2 are taken: weak field of 0.34 nG from [81] and strong field of 15 nG from [84, 79]. Figure 6.6 shows that the impact of these two magnetic fields compared to a zero magnetic field is mainly visible at $E < 10^{19}\,\mathrm{eV}$. Magnetic fields cause energy losses due to synchrotron radiation of electrons and positrons emerging from pair production in the electromagnetic cascades. The energy loss due to synchrotron radiation increases with the magnetic field strength and kinetic energy of the electron, as shown for example in [178]. For the lower energies shown in Fig. 6.6 the energy loss length is still large enough to allow several inverse Compton scattering and pair production processes in the electromagnetic cascade and

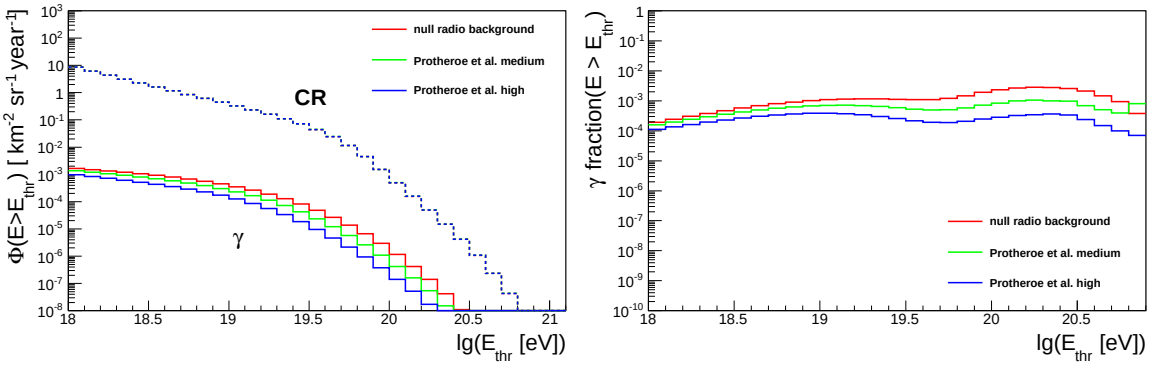

Figure 6.5: As in Fig. 6.1 but displaying the influence of the radio background light.

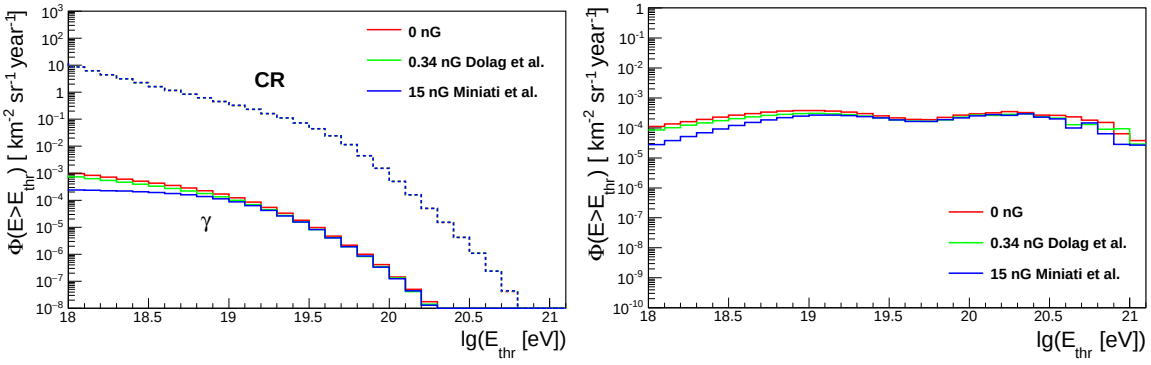

Figure 6.6: As in Fig. 6.1 but displaying the influence of the magnetic field.

hence the effect is more pronounced for a stronger magnetic field. At higher energies the electron-positron pairs immediately loose all their energy leading to a decrease of the effect. Regarding the maximum rigidity of 10^{20} eV, photons with $E > 10^{19}$ eV mostly arise directly from the first production and do not undergo an electromagnetic cascade at all. Conclusively, no effect from the magnetic field is seen. In this study no influence of the magnetic field on the cosmic ray propagation is considered in the simulation.

Source Mass Composition The choice of the mass of the primary particle has a significant influence on the photon flux as can be seen in Fig. 6.7. The photon flux from protons is more than one order of magnitude higher than that of iron primaries. The primary nuclei can only produce photons by photo-pion production which is only dominant at the highest energies and has thereby a minor contribution to the overall photon flux. The dominant interaction of nuclei in the here relevant energy regime is the photodisintegration as described in Sec.2.4, leading to secondary nucleons. These nucleons are able to undergo pion production and are the dominant source of secondary

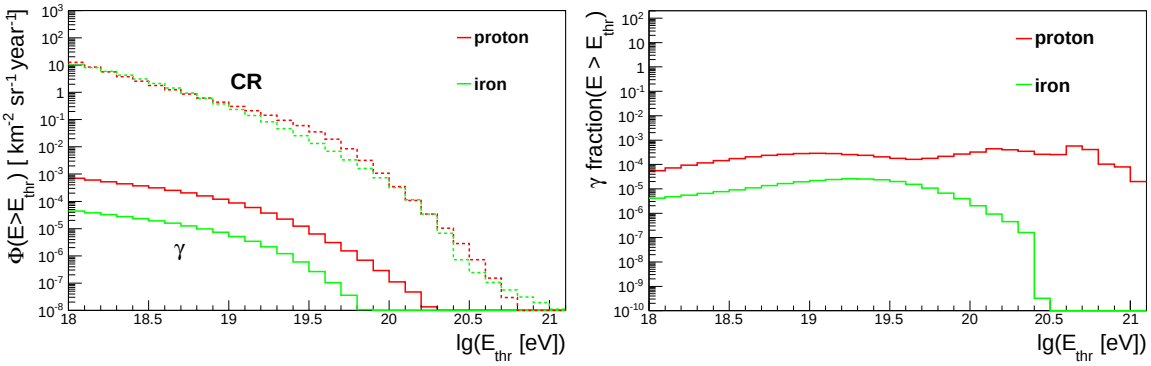

Figure 6.7: As in Fig. 6.1 but displaying the influence of the source mass.

photons. In case of iron not all nuclei undergo this interaction which is one of the reasons of the suppressed photon flux. Although the same maximum rigidity means a 26 times higher maximum energy for the iron nuclei ($E = R \cdot Z$) the energy per nucleon is still higher for protons which is the second reason of the higher photon flux.

6.1.3 Photon Flux Prediction for Reasonable Scenarios

In this section a prediction of the expected photon flux and fraction is derived for astrophysical scenarios with reasonable parameter ranges. The spectral index and maximum rigidity at the sources are fixed by a combined fit to the cosmic ray energy spectrum and the mass composition for a pure proton and a pure iron composition as described in Sec. 5.1.1. The variation of the source evolution, the magnetic field and the radio background are considered in two scenarios named *photon 1* and *photon 2*:

- *photon 1*: Low radio background from [177], IGMF of 0.34 nG perpendicular to the path of the particles and source evolution following the star formation rate [67] ($\rho(z) \propto (1+z)^{3.4}$ for $z < 1$).
- *photon 2*: A high radio background [177], IGMF of 15 nG, and a steeper source evolution as indicated for quasars [69].

Photon 1 contains parameters leading to low photon fluxes whereas *photon 2* includes parameters which cause high photon fluxes in the studies in Sec. 6.1.2. Within these scenarios the consideration of sources up to $D_{\mathrm{max}} = 2800$ Mpc is sufficient, as more distant sources do not contribute neither to the nucleon- nor the photon-fluxes as showed in Sec. 6.1.2 and Sec. 5.1.1. Again, the infrared background from Kneiske et al. [2] is used for all scenarios in this section. The parameters used for the source energy spectrum and the maximum rigidity are shown in Tab. 6.1. As discuses in Chapter 5 in case of proton primaries no change in the fit results is seen including the X_{max} measurements.

	α	$\lg(R_{\max}/\mathrm{eV})$	χ^2/ndf
proton photon 1	-1.7	19.5	50.1 / 12
proton photon 2	-2.1	19.6	20.0 / 12
iron photon 1	-1.3	19.8	447.1/ 30
iron photon 2	-1.4	19.5	279.5 / 30

Table 6.1: Spectral index α and maximum rigidity $R_{\max}$ from the fit to the energy spectrum and the $X_{\max}$ moments [95] for the individual photon scenarios as specified in the text.

The resulting photon flux and fraction predictions are shown in Fig. 6.8. Both proton sources scenarios give higher flux predictions than in the case of the iron sources. For iron sources the *photon 1* scenario is above the *photon 2* scenario as the effect of harder spectral index and higher maximum rigidity outweight the effect of the other parameters. All photon predictions are well below the upper limits for the photon flux as reported by [179, 44, 180, 181, 182] and the photon fraction as reported by [183, 184]. In addition, the photon sensitivities expected in the Pierre Auger Observatory [185] are shown where the same efficiencies and number of candidates are used as given in the last publication on the photon hybrid limits [44] and the SD limits [179]. These sensitivities can not be reached by any of the chosen scenarios.

Conclusively, photon upper limits in the ultra high energy regime can not put additional constraints on parameters of the astrophysical scenarios compared to the one from the combined fit to the Auger energy spectrum and the $X_{\max}$ moments as derived in chapter 5.

Comparison with other Studies A comparison with the predictions of the photon fluxes from Decerprit et al. [186] and Gelmini et al. [187] shows that the prediction from this work is below the other predictions as can be seen in Fig. 6.9. In the case of Decerprit et al. the main difference in the photon flux results from different choices of the source spectral index and maximum rigidity. Decerprit et al. determine the source spectra from a fit to the energy spectrum from the Pierre Auger Observatory [164] published in the year 2010 fitting energies down to 10^{18} eV and a fixed maximum energy of $10^{20.5}$ eV. The photon flux calculated with the same model parameters as in Decerprit et al. is in a much better agreement though still a factor of two lower. This difference is reasonable as different calculation methods are used for the electromagnetic cascades. Decerprit et al. uses a Monte Carlo technique whereas the CRPropa code used in this work deploys a parametrization obtained from analytic calculations. In the comparison to the prediction from Gelmini et al. [187] the main difference comes from the choice of the source parameters. In that work a fit to the AGASA data [188] is performed for $E > 4 \cdot 10^{19}$ eV yielding nine energy bins. In this fit $E_{\max} = 1.28 \cdot 10^{21}$ eV is fixed and the spectral index and the minimum distance of sources are varied within a range that allow a goodness of fit with a p-value above 0.05. This allows very hard spectral indices because of the small energy range and high statistical uncertainties of the AGASA

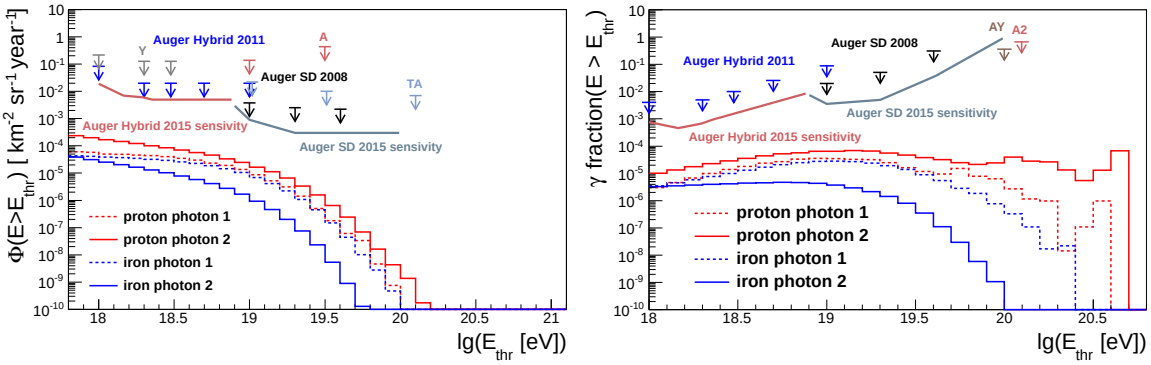

Figure 6.8: Integral photon flux (left) and the integral photon fraction (right) from simulations assuming the *photon 1* and the *photon 2* scenario as introduced in the text for pure proton and pure iron sources. The experimental upper limits for the photon flux from Pierre Auger Observatory (Auger) [179, 44], Akeno (A) [180], Yakutsk (Y) [181] and Telescope Array (TA) [182] as well as for the photon fraction from Agasa and Yakusk (AY) [183] and AGASA (A2) [184] are added. In addition the expected sensitivities for the year 2015 [185] are shown.

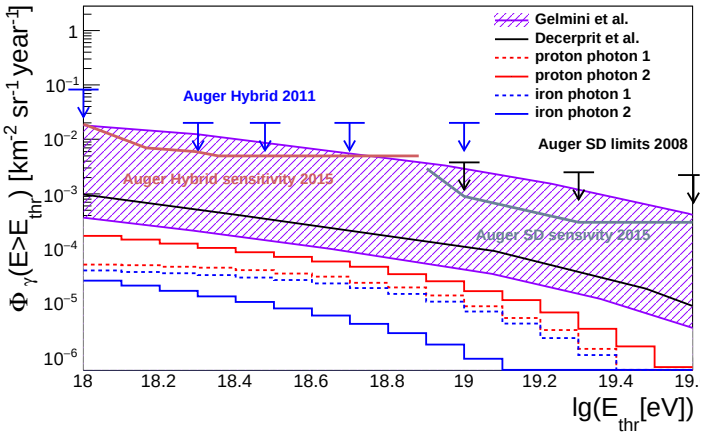

Figure 6.9: Comparison of the predictions for the integral photon flux as shown in Fig. 6.8 to the predictions from Decerprit et al. [186] and Gelmini et al. [187].

data. Comparing predictions from this work with the one from Gelmini et al. assuming the same parameter set shows a very good agreement. This is reasonable as the method used to calculate the photon fluxes is a numerical calculation of the according transport equations [189] and hence corresponds to method used in CRPropa. Gelmini et al. shows in addition other predictions for an example assuming a fit to HiRes [94] data leading to photon flux predictions which are an order of magnitude lower than the

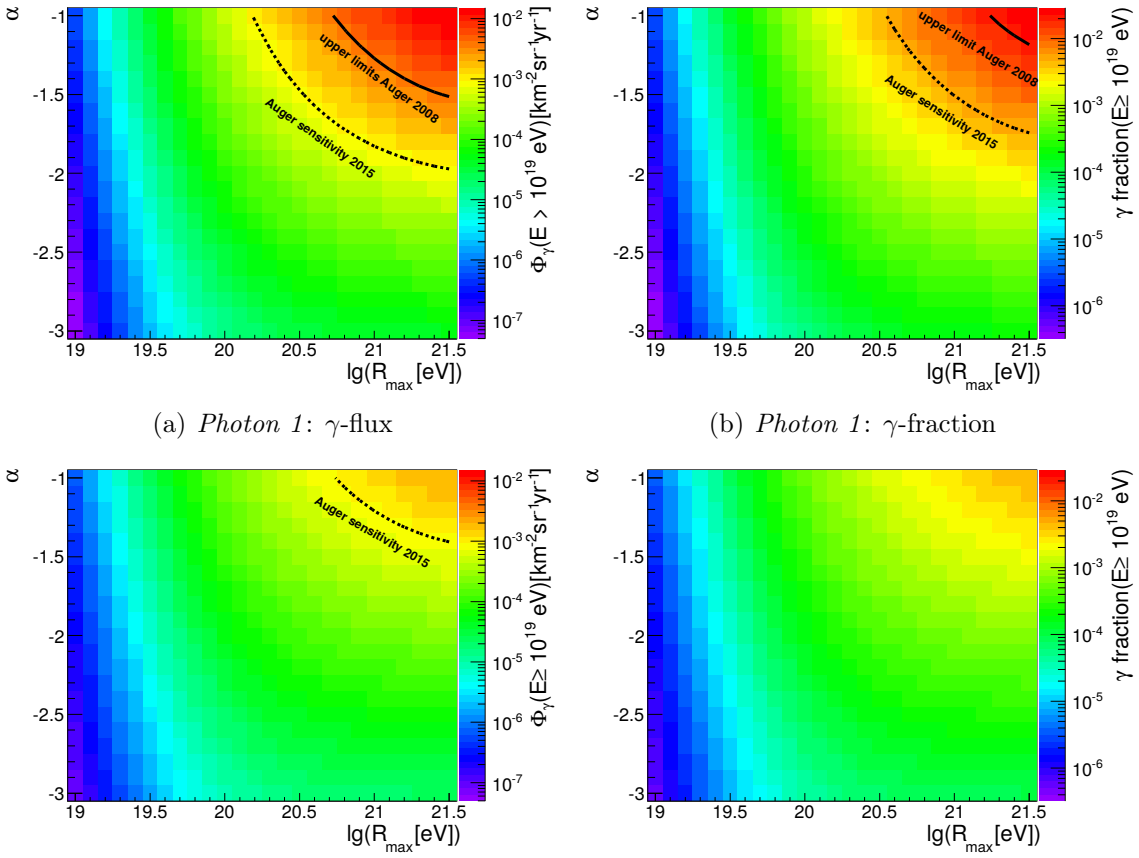

(a) *Photon 1*: γ-flux

(b) *Photon 1*: γ-fraction

(c) *Photon 2*: γ-flux

(d) *Photon 2*: γ-fraction

Figure 6.10: Predictions for the integral photon flux (left column) and integral photon fraction (right column) above 10^{19} eV in dependence of α and $R_{\max}$. The lines show the current upper limits by the Pierre Auger Collaboration [179] and the sensitivities for the year 2015 [185]. Parameter combinations predicting higher neutrino fluxes can be excluded by these limits. The top row shows the *Photon 1* the bottom row the *Photon 2* scenario.

photon flux from the fit to the AGASA data. Nevertheless, the version with a fit to the AGASA data is used here for comparison as this is also the theoretical expectation shown in publications containing the Auger data [179, 44].

6.1.4 Constraints on Source Spectra and Maximum Energy

In this section the possibility to put constraints on the parameter space of astrophysical scenarios only by considering the non-observation of UHE photons is shown. The exclusion of ranges of source spectral index α and the maximum rigidity $R_{\max}$ are considered here as these two parameters highly influence the photon flux predictions as shown in Sec. 6.1.2. To demonstrate the maximum possible constraining power pure proton sources and the *photon 1* scenarios are chosen. Assuming the same spectral

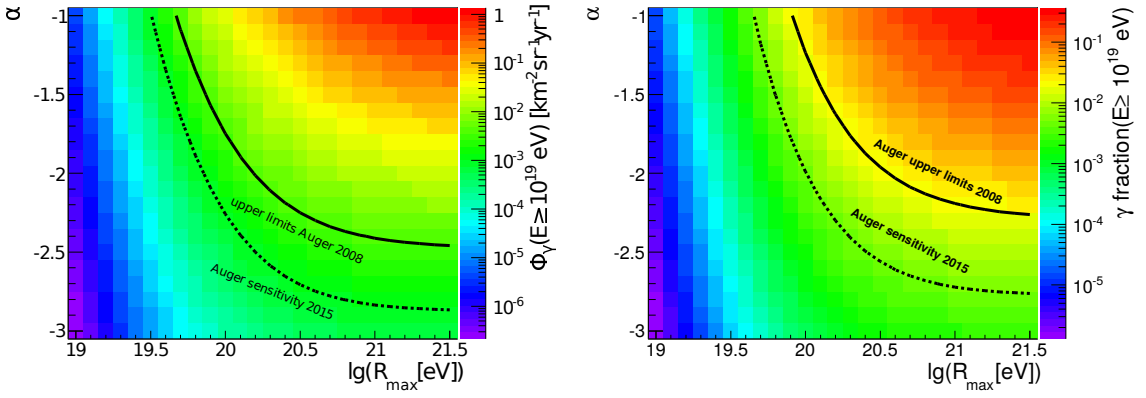

(a) flux (b) fraction

Figure 6.11: Same as in the top row of Fig. 6.10 but with sources up to $D_{\mathrm{max}} < 10\,\mathrm{Mpc}$.

index and maximum rigidity the *photon 1* scenario should produce the highest photon flux as seen in the single parameter studies in Sec. 6.1.2. The photon flux and the photon fraction are obtained by scanning the source spectrum and maximum rigidity in the ranges $\alpha \in [-1, -3]$ and $R_{\mathrm{max}} \in [10^{19}\,\mathrm{eV}, 10^{21.5}\,\mathrm{eV}]$ and the predictions for the threshold energy $E_{\mathrm{tres}} = 10^{19}\,\mathrm{eV}$ are compared to the upper limits and the expected future sensitivities as seen in Fig. 6.10. The range of spectral indices α used here are motivated by theoretical predictions for source candidates as introduced in Sec. 2.1.5. The range for the maximum rigidity at source is motivated from the capability of potential acceleration sites as also introduced in Sec. 2.1.5.

The plots show already an exclusion of combinations of very hard spectral index and high maximum rigidity given by current upper limits assuming the *photon 2* scenario. The predictions for the photon flux are able to constrain a larger parameter space than in the case of photon fraction. This is due the fact that the simulated cosmic ray flux for the α and R_{max} combination regarded here is higher than the one from data. As already mentioned in Sec. 3.3.3 the photon flux limits from the data are more reliable than the photon fraction limits and so are the exclusions from the photon flux. With the expected sensitivity of the Pierre Auger Observatory for data up to 2015 a wider range of the parameter space can be excluded. The low photon scenario does only allow exclusions with future sensitivities. These exclusions are in the extent of those from the current upper limits for the high photon scenario.

6.1.5 Sensitivity to Local Sources

As seen in Sec. 5.2.7 an over-density of nearby sources show an improvement in the fit to the energy spectrum and X_{max} moments. The main contribution to the photon flux is expected from nearby sources as can be seen in Fig. 6.3. Hence, for such a scenario the photon flux limits could put additional constraints. The exclusion power for the α and R_{max} space in case of *proton 1* sources with D_{max} up to 10 Mpc is studied for this purpose. As displayed in Fig. 6.11 this poses higher constraints on the parameter

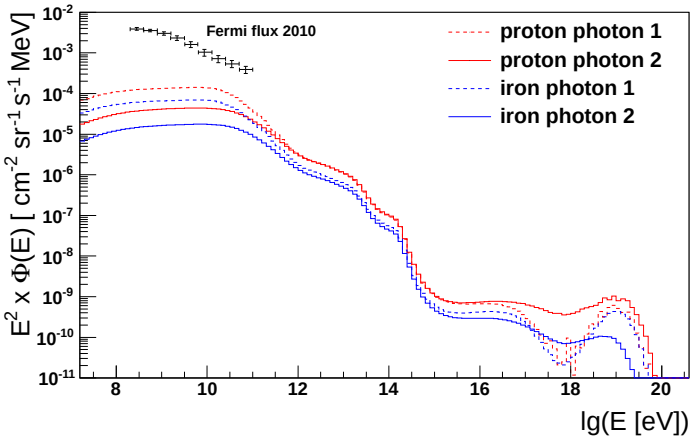

Figure 6.12: Differential photon flux for *photon 1* and *photon 2* scenario displayed down to GeV energies along with the photon flux measured by the FERMI Collaboration [190].

space as seen for the *proton 1* scenario from Sec. 6.1.4. But still parameters yield from the combined fit from Sec. 6.1.3 can't be excluded.

6.1.6 Implications on GeV Photon Fluxes

In addition to the expected photon observation in the ultra high energy region photon measurements exist from the FERMI satellite [190] at GeV energies. In this section the photon fluxes down to these energies are shown and it is discussed whether the measured flux in the GeV to PeV region can put additional constraints to cosmic ray scenarios. As the universe is transparent for photons at these energies, also distances up to 3880 Mpc which corresponds to $z = 8$ are considered here. Again, the *photon 2* and *photon 1* scenarios for proton and iron sources are assumed with the same source spectrum and maximum rigidity as used in Sec. 6.1.3.

Figure 6.12 displays the differential photon fluxes propagated down to 10^8 eV along with the photon flux measured by FERMI [190]. Starting from the highest energies which are already described above a decrease is seen down to below 10^{18} eV which is more prominent for the *photon 1* scenario. This first dip is caused by the decreased interaction length for photons and the losses due to magnetic fields. The flux increases for energies below 10^{15} eV where the minimum of the photon interaction length is reached. For photons with lower energy the energy loss length increases down to 10^{12} eV where the universe is transparent for photons. Between 10^{12} eV and 10^{14} eV the infrared background also contributes to the photon interaction and is imprinted in the photon flux. The photon flux is accumulated at GeV energies also from the highest distances and is hence highly influenced by the source evolution. As mentioned in Sec. 2.4.4, the photon background density is increased at higher redshift yielding more interaction of the cosmic rays. However, the energy of the photon background is higher

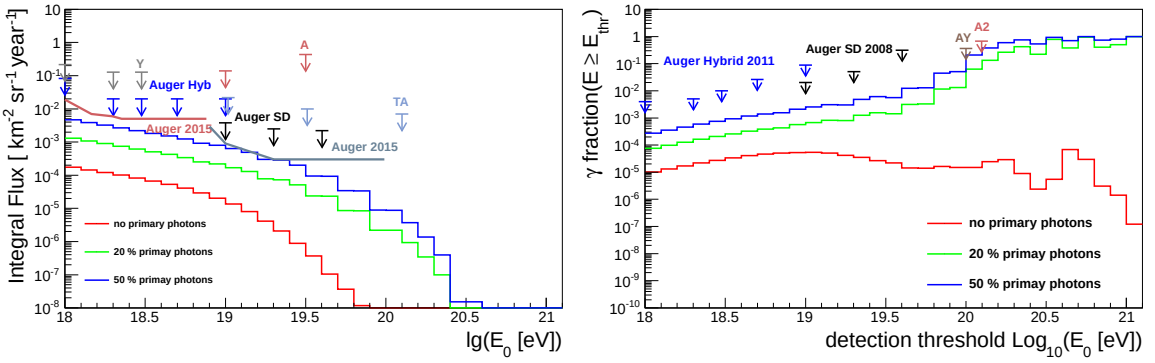

Figure 6.13: Integral photon flux (left) and photon fraction (right) from pure proton sources according to the *photon 1* lines in Fig. 6.8 but with 20% and 50% photons produced at the source of cosmic rays.

allowing cosmic rays with lower energies to undergo interactions. Hence, the *photon 1* scenario with the steeper source evolution has also a higher flux at GeV compared to the *photon 2* scenario. For the proton scenario, this is the opposite behavior to the one observed in the UHE regime. Again, the iron sources produce lower photon fluxes than in the proton case. All four scenarios stay well below the flux measured by the FERMI experiment posing no additional constraints to the scenario from the observed low energy photons. The simulations do not contradict the FERMI data as the main sources of photons in the GeV regime are not descended from UHECR.

6.1.7 Assuming a Photon Component at Source

In case of interactions of cosmic rays with matter and radiation at the source itself, photons should also be emitted directly at the sources of UHE cosmic rays due to the production of π^0 [98]. A brief study for this case is done by directly introducing of a photon component emitted at otherwise pure proton sources. The photon component follows the same energy spectrum as the proton component except for a variation of the absolute flux at the sources. Fig. 6.13 shows the photon flux and photon fraction for the case of no, 20 % and 50 % photons at the source. Here 50 % would correspond to equal fluxes of photons and protons. The parameters are chosen according to the *photon 1* scenario. A clear increase in the photon flux can be observed in comparison to a pure proton composition at the sources.

Although an energy spectrum with the same spectral shape is predicted [98] for the photon component produced at the sources the absolute flux and maximum energy should be lower as in case of cosmic rays [191]. Hence, the shown study can be seen as an optimistic scenario.

6.2 Study of Neutrino Flux

In analogy to the previous photon studies, in this section predictions for UHE neutrinos are calculated. There is evidence for extraterrestrial neutrinos of energies up to $2 \cdot 10^{15}$ eV from recent measurements by the IceCube Collaboration [192]. The detection of UHE neutrinos would be a unique opportunity to point-back to the sources of cosmic rays. Because of their small interaction rate, neutrinos can reach us from their point of production without nearly an alteration.

The neutrino studies are structured similarly as the photon studies. At the beginning, a study of the influence of single parameters of the astrophysical scenario on the neutrino flux is done. The neutrino flux for individual astrophysical scenarios assuming the source spectra and maximum rigidity derived from a combined fit as done in Sec. 5.2.2 and individual source distributions is simulated to obtain realistic predictions. Comparing to the current experimental upper limits for the UHE neutrino flux the ability to constrain the astrophysical parameters is tested. Finally, the power to constrain this parameter space is compared to the constraints from the photon upper limits.

6.2.1 Simulation Setup

The setup for the simulation is chosen according to the previous section concerning photons. As the production and propagation of neutrinos are not effected by the radio background and the intergalactic magnetic fields both are not considered in the simulations. Neutrinos produced by the GZK effect or neutron decay are propagated without interactions. The normalization of the neutrino flux is derived from the normalization of the cosmic ray flux. In this work the all flavour fluxes are shown. The upper limits published by the Pierre Auger Observatory [193] are referring only to single flavour fluxes. Due to neutrino oscillation the flux ratio of 1:1:1 is expected for the three neutrino flavours. Conclusively, the all flavour limits can be translated into single flavour limits by a simple multiplication with a factor of three as used in this chapter.

6.2.2 General Parameter Studies

In this section the impact of single parameters of the astrophysical scenario on the predicted neutrino flux is studied. For this purpose a standard scenario is defined with continuous proton sources distributed according to quasars [69] at distances from 4 Mpc up to 3880 Mpc ($z \approx 8$), source spectra with $\alpha = -2$ and $R_{\mathrm{max}} = 10^{20}$ eV, and the Kneiske et al. infrared background. The flux is normalized at 10^{19} eV for these studies. One should note here that the neutrino flux in the following plots are multiplied by E^2 to pronounce the deviations from an E^{-2} spectrum as also done in the publication of the upper limits, for example in [193].

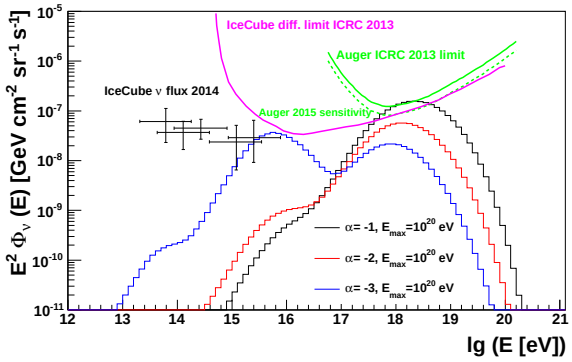

(a) spectral index

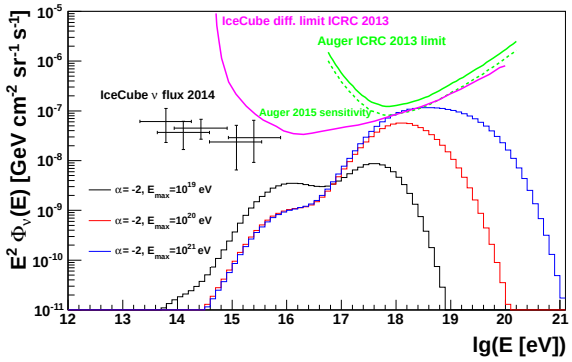

(b) maximum rigidity

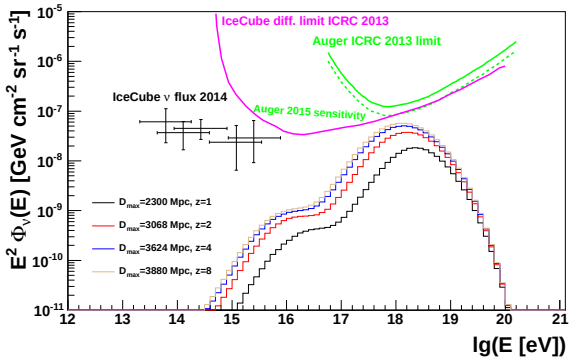

(c) maximum source distance

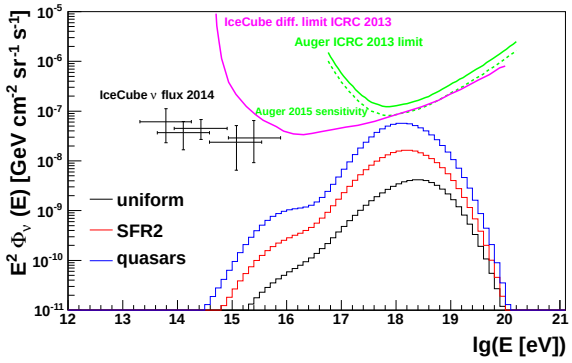

(d) source evolution

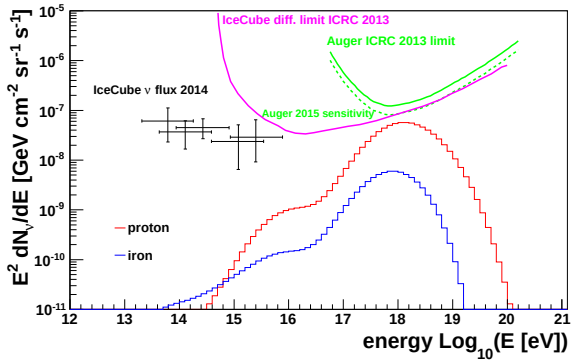

(e) mass composition

Figure 6.14: Differential neutrino flux multiplied with the energy E^2 displayed for a standard scenario as specified in the text. The influence of individual parameters spectral index **(a)**, maximum rigidity **(b)**, maximum source distance **(c)**, the evolution of the sources **(d)** and the primary mass **(e)** are displayed. The experimental upper limits for the neutrino flux from the Pierre Auger Observatory (Auger) [193] and the IceCube experiment [194] as well as the sensitivity for the Pierre Auger Observatory in 2015 are displayed. The neutrino flux measured by the IceCube experiment [192] is also added.

Spectral Index The first study shows that the variation of the spectral index in the range [-3, -1] changes the shape and the strength of the ν flux as displayed in Fig. 6.14(a). For $\alpha = -1$ a high energy bump is seen between the 10^{18} eV and 10^{19} eV which decreases more than one order of magnitude by changing the spectral index to $\alpha = -3$. A second low energy bump appears between 10^{15} eV and 10^{16} eV which is dominant for the soft spectra $\alpha = -3$ and already appears for $\alpha = -2$. The high energetic neutrinos are produced in the interactions of the highest energy cosmic ray protons with the CMB whereas the low energetic neutrinos are produced by interactions of lower energetic protons with the infrared background, as described in [65]. Hardening the source spectra leads to more high energy source protons which explains the increase in the high energy bump and decrease in the low energy bump. A third bump at even lower energies is visible for $\alpha = -3$ which originates from the decay of neutrons.

Maximum Rigidity Enhancing the maximum rigidity from 10^{19} eV to 10^{21} eV as shown in Fig. 6.14(b) causes an increase in the neutrino flux especially towards higher energies. This is obvious as protons with higher energies allow the production of more energetic neutrinos and increase also the amount of low energetic neutrinos. Only at energies below 10^{17} eV the highest flux is produced from the $R_{\mathrm{max}} = 10^{19}$ eV sources. This is due to the normalization to the Auger energy spectrum at 10^{19} eV.

Maximum Distance of Sources The contribution of different source distances to the neutrino spectrum is studied in Fig. 6.14(c) by varying the maximum propagation distance D_{max} from 2300 Mpc ($z \approx 1$) to 3880 Mpc ($z \approx 8$). A continuous increase of the flux with D_{max} is observed even beyond $z = 1$. This is possible as neutrinos are influenced only by weak interactions and therefore can reach us even from the early universe without attenuation. Sources more distant than $z = 4$ seems to have only small influence on the overall flux due to redshift dilution as described for example in [65]. A simulation of the cosmic ray propagation up to $z = 8$ is here sufficient as the source density decreases for higher z as described in Sec. 2.1.6. It should also be mentioned, that the neutrino fluxes from nearby sources give only a small contribution.

Evolution of Sources For the three source evolution scenarios introduced in Sec.2.1.6 the neutrino flux varies more than one order of magnitude as seen in Fig. 6.14(d). The steepness of the source evolution increases from uniform over SFR to quasars. With increasing redshift the density of the photon background increases which results in a higher GZK interaction rate and conclusively in a larger neutrino flux.

Source Mass Composition Assuming iron primaries instead of proton ones reduces the flux significantly for most energies as can be seen in Fig. 6.14(e). Here, the same explanation as for the photon case in Sec. 6.1.2 holds. In addition, for lower energies the difference gets smaller yielding a higher neutrino flux from iron sources below 10^{14} eV.

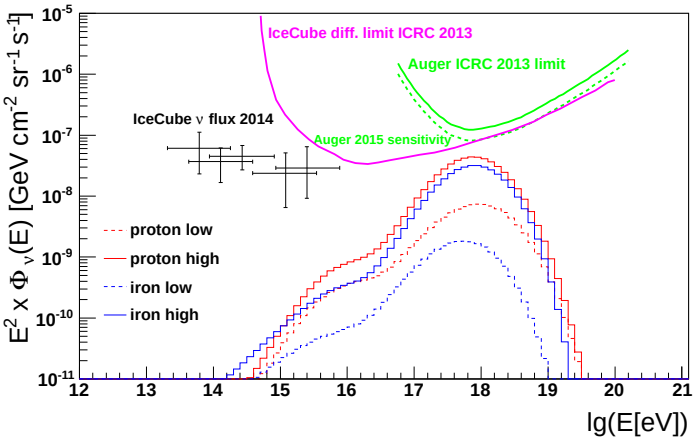

Figure 6.15: Differential neutrino flux multiplied with the energy E^2 from simulations for the *neutrino low* and *neutrino high* scenario as specified in the text each for pure proton and pure iron sources. The spectral index and maximum rigidity are fixed by the combined fit to data. The experimental upper limits for the neutrino flux from the Pierre Auger Observatory (Auger) [193] and the IceCube experiment [194] as well as the sensitivity for the Pierre Auger Observatory in 2015 are displayed. The neutrino flux measured by the IceCube experiment [192] is also added.

6.2.3 Neutrino Flux Prediction for Reasonable Scenarios

As done in the case of the photon flux in Sec. 6.1.3, the neutrino flux predictions are obtained using reasonable parameter ranges for the astrophysical scenarios. The source spectral index and maximum rigidity are again taken from the combined fit as shown in Tab. 6.2. For the neutrino fluxes the main influence beside the source spectrum, the maximum rigidity and the mass composition at source is the source evolution. Hence, two scenarios are chosen differing only in the source evolution:

- **neutrino low:** Source evolution follows the star formation rate [67].
- **neutrino high:** A steeper source evolution as indicated for quasars [69].

Note that the dependency on the source evolution is reversed for the neutrino flux compared to the photon behavior discussed in Sec. 6.1. For each scenario again proton and iron sources are considered. The maximum distance of the sources is enlarged to 3880 Mpc compared to the photon scenario as a relevant contribution from these sources has been seen in Sec. 6.14. In Fig. 6.15 the resulting neutrino fluxes can be seen. The *neutrino high* and *neutrino low* scenarios show a significant difference for both types of source nuclei. The neutrino fluxes from the iron sources are below the corresponding predictions from proton sources for most energies. Only neutrinos with energies below 10^{15} eV from iron sources in the *neutrino high* scenario exceed

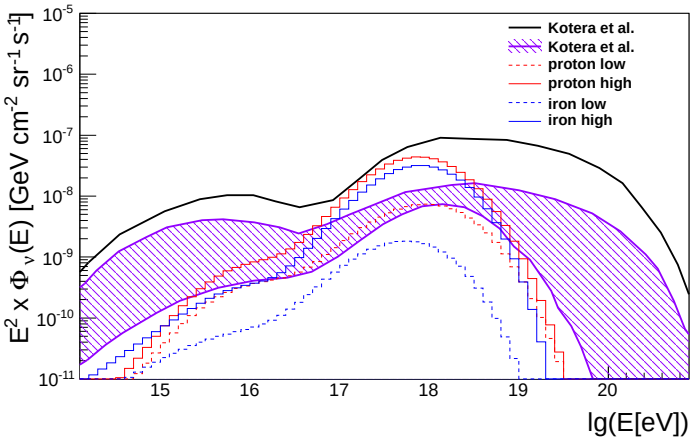

Figure 6.16: Same as in Fig. 6.15 with an additional comparison to predictions done by Kotera et al. [65].

the corresponding neutrino fluxes from the proton sources. All predictions are well below the upper limits from the Pierre Auger Collaboration [193] and from IceCube Collaboration [194] and do not put additional constrains to the best fit derived in chapter 5. These fluxes also seems hardly be responsible for the neutrino flux measured by the IceCube Collaboration [192] as already pointed out in [195].

Comparison with other Studies In Fig. 6.16 the predictions from the *neutrino low* and the *neutrino high* scenario are compared to the optimistic line and the wide range of standard scenarios from Kotera et al. [65]. In the energy range $10^{17}\,\mathrm{eV} < E < 10^{19}\,\mathrm{eV}$ the neutrino predictions from this work are in general agreement with the predictions from Kotera et al. But for energies above $10^{19}\,\mathrm{eV}$ and below $10^{17}\,\mathrm{eV}$ the flux from Kotera et al. significantly overshoots the flux obtained in this work. This is due to a different choice of the parameters in particular the source spectrum and maximum rigidity. In Kotera et al. $R_{\mathrm{max}} = 10^{20.5}\,\mathrm{eV}$ is fixed and the spectral index is fitted to the energy spectrum from the Pierre Auger Observatory published in 2010 [110]. The wide band from Kotera et al. shows a variety of different assumptions

	α	$\lg(R_{\mathrm{max}}/\mathrm{eV})$	χ^2/ndf
Proton low (SFR)	-2.1	19.6	20.0 / 12
Proton high (quasars)	-1.7	19.5	50.1 / 12
Iron low (SFR)	-1.4	19.5	279.5 / 30
Iron high (quasars)	-1.3	19.8	447.1 / 30

Table 6.2: Spectral index α and maximum rigidity R_{max} from the fit to the energy spectrum and the X_{max} moments [95] for the individual neutrino scenarios as specified in the text.

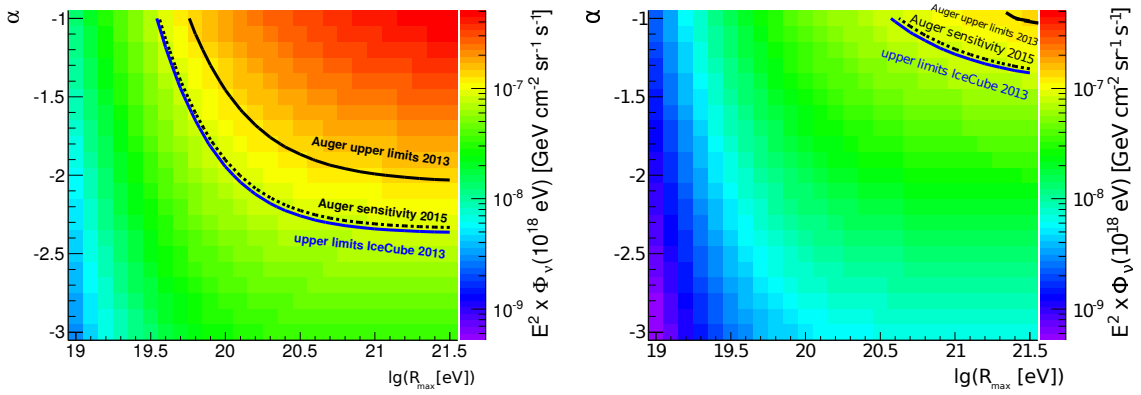

(a) *neutrino high* scenario

(b) *neutrino low* scenario

Figure 6.17: Differential neutrino flux at 10^{18} eV in dependence of α and $E_{\max}$ for the *neutrino high* **(a)** and the *neutrino low* **(b)** scenario assuming proton sources. Black lines show the current [193] and future sensitivities of the Pierre Auger Observatory and the blue lines corresponds to the upper limits from the IceCube experiment [194]. Parameter combinations predicting higher neutrino fluxes can be excluded by these limits.

for composition, galactic to extragalactic transition and source evolution excluding the quasars case. The optimistic prediction from Kotera et al. uses the quasars source evolution and a fix maximum energy of $10^{21.5}$ eV. Comparing the predictions from this work obtained with the same parameters as used in Kotera et al. shows a very good agreement for the energies above $\sim 10^{17}$ eV. For lower energies still a four times lower neutrino flux is obtained from our predictions. In Kotera et al. photon background estimation according to Stecker et al. [196] are used which are lower in the optical and ultra violate range than the estimation from Kneiske et al. used in this work and hence could be an explanation for the discrepancy at lower energies. In Kotera et al. the same qualitative difference to predictions using photon background by Stecker et al. is pointed out.

6.2.4 Constraints on Astrophysical Scenarios

In this section the constraints from the current and future upper limits on the neutrino flux are studied as already done in Sec. 6.1.4 for the photon flux and fraction. For this purpose the neutrino flux at 10^{18} eV was obtained for the range of spectral indices $\alpha \in [-3, -1]$ and maximum rigidity $R_{\max} \in [10^{19}, 10^{21.5}]$ eV. The energy of 10^{18} eV is chosen as this seems to be the best sensitivity of the Pierre Auger Observatory as well as the maximum of the neutrino flux as one can see in Fig. 6.15. The experimental data from the Pierre Auger Observatory as well as from the IceCube experiment are taken, as they are the most constraining for these energies. The *neutrino low* and the *neutrino high* scenarios assuming proton sources are considered here.

For the *neutrino high* scenario as shown in Fig. 6.17(a) the current upper limits

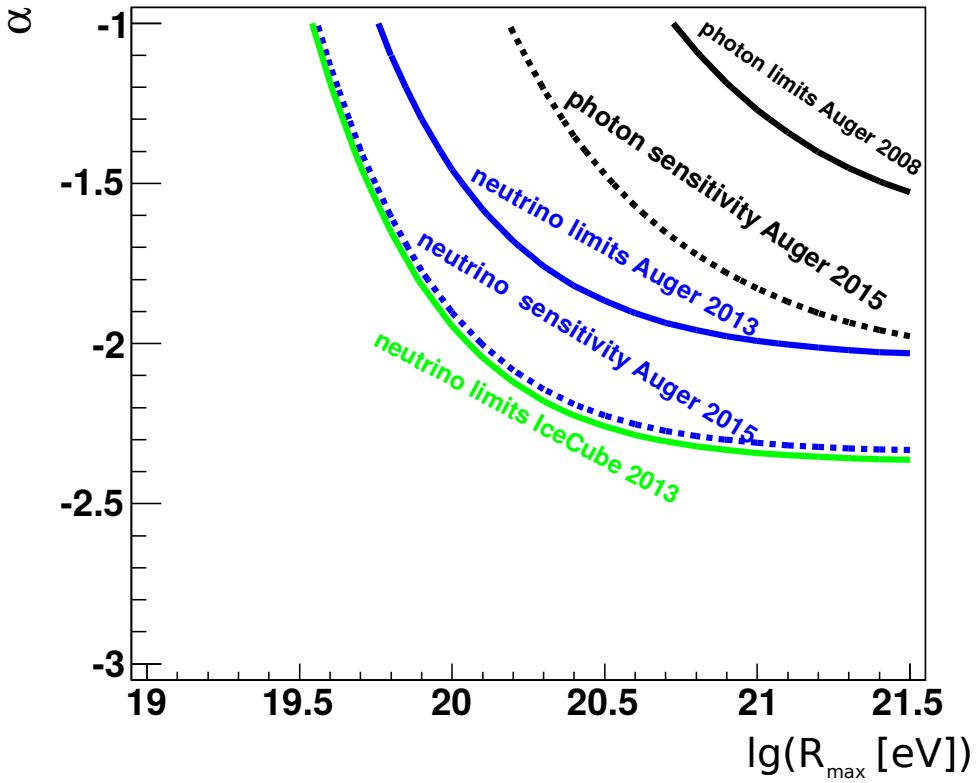

Figure 6.18: Comparison of exclusion power for source spectral index α and maximum rigidity R_{max} between photon and neutrinos flux as already individually displayed in Fig. 6.10 and Fig. 6.18.

from the Pierre Auger Observatory from 2013 [95] are exceeded by scenarios with hard spectral indices and high maximum rigidity leading to an exclusion of this parameter range for this scenario. Assuming an extrapolation of the upper limit from the Pierre Auger Observatory for the year 2015 enables a potential exclude of a wider parameter range. The extrapolation of the upper limits is done assuming no background and a full operation of the experiments. The current upper limits of the IceCube experiment [194] using data up to 2013 are similar to the sensitivity of the Pierre Auger Observatory in 2015 excluding roughly the same parameter range. In the low neutrino scenario the current upper limit from the Pierre Auger Collaboration can nearly put no constraints to the parameter range here regarded. Only the future sensitivity could put some constraints to high R_{max} and α regions as seen in Fig. 6.17(b).

6.3 Comparison of the Exclusion Power from UHE Photons and Neutrinos

In Fig. 6.18 the exclusion power of the neutrino limits is compared to the one from the limits and expected sensitivities on the integral photon flux for $E > 10^{19}\,\mathrm{eV}$.

The current neutrino flux limits from the Pierre Auger Observatory as well as those from the IceCube experiment exclude a wider range of the parameter space than the photon limit from the Pierre Auger Observatory. One should mention that the current upper limits for neutrinos were obtained by taking into account the data up to the year 2013 whereas photon upper limits shown here use only the data up to 2008. Previous neutrino upper limits from the Pierre Auger collaboration [197] as well as from the IceCube collaboration [198] that use a comparable data set to the one from the current photon limits have a worse discrimination power than the photon limits, excluding only parameter regions outside the range shown here. The better improvement of the exclusion power by neutrino limits is due to the lower decrease of the neutrino predictions with α and R_{max}. For the given parameter space the neutrino flux have a range of about two orders of magnitude whereas the photon flux ranges about five orders of magnitude as can be seen by comparing Fig. 6.10 and Fig. 6.18. This is due the fact that the neutrino flux is compared to the limits at 10^{18} eV and the photon flux above 10^{19} eV. As can be seen for example in Fig. 6.2 the photon flux at 10^{18} eV shows less variation but a worse upper limit at that energy would also lead to less exclusion at all. Regarding future sensitivities the neutrino limits from the Pierre Auger Observatory show a much better exclusion potential of the α–R_{max} space than of the photon sensitivities.

6.4 Summary

In this chapter predictions for the secondary UHE photon and neutrino fluxes are made for a range of astrophysical motivated scenarios. At first studies for the dependence of these secondary fluxes from relevant model parameters are done which are essential for choosing the following scenarios. Then, predictions for the photon flux, photon fraction and neutrino flux were made using the source spectra and maximum rigidity obtained from the combined fit to the cosmic ray energy spectrum and X_{max} moments as introduced in chapter 5. To take into account a reasonable range of other astrophysical model parameters a high and low flux scenario for pure proton and pure iron sources are considered. The photon fluxes as well as the neutrino fluxes from all of these scenarios are below the current upper limits and experimental sensitivities to be reached in the near future. The comparison of the photon flux from these scenarios resulting at GeV energies with the flux measured by the FERMI experiment show also no constraints. Additionally, the power to constrain the parameter space of the source spectral index and maximum rigidity at the sources only from the none observation of these secondary fluxes is shown. Photon flux and fraction can already constrain hard spectra and high rigidities for the optimistic parameter setting whereby it is shown that the flux is more constraining than the fraction. The future limits should constrain a more reasonable part of the parameter range. The current upper limits on the neutrino flux obtained by the Pierre Auger Observatory can constrain an even wider range of the α–R_{max} space than the current upper limits on the photon flux as well as the expected photon sensitivities for the year 2015. The current upper limits

of the IceCube experiment for the neutrino flux exclude even higher parameter ranges being at the order of the expected sensitivities of the Pierre Auger Observatory for the year 2015. A further result show that a strong over-density of very nearby sources at $\sim 10\,\mathrm{Mpc}$ could significantly increase the photon flux yielding even better constrains than from the neutrino case.

7 Arrival Directions of Cosmic Rays

To find the origin of the UHECR is one of the main goals of contemporary astroparticle physics. Extragalactic and galactic magnetic fields which are described in Sec. 2.2 and 2.3 prevent in general direct observation of sources for charged particles. As the rigidity of cosmic rays rises with energy, at least a fraction of the most energetic cosmic rays should point back to their sources. The arrival directions for these cosmic rays should be anisotropic, assuming a sufficient low source density. Many observables aiming at measuring such an anisotropy are tested using the UHE data. A summary of the most important analysis done by the Pierre Auger collaboration in this field is given in Sec. 3.3.5. In this chapter the correlation of the cosmic ray arrival directions with their source positions is used analog to the procedure used by the Pierre Auger Collaboration where measured arrival directions are compared with active galactic nuclei positions from the Véron-Cetty and Véron Catalog [122] (VCV) which is described in details in Sec. 3.3.5.

Simulations with different assumptions for source properties and extra galactic magnetic field models are studied in this context. At first it is checked whether a deviation from isotropy can be detected in the simulated scenarios. In a second step the fraction of correlated events from the different scenarios are directly compared with the one measured by the Pierre Auger Observatory to pose additional constraints to those given in chapter 5.

To compare the model predictions with data the simulation set up as well as the calculation of the correlation fraction are set according to the analysis of the Pierre Auger Observatory [123, 124, 125].

7.1 Data

As described in Sec. 3.3.5, the analysis of the data from the Pierre Auger Observatory [125] determines the fraction of cosmic ray events that show an angular deviation to the positions of AGN from the VCV catalog of less than 3.1°. For this analysis only AGN within 75 Mpc and events with energies E>55 EeV are used. This special selection of correlation angle, maximum source distance and minimum energy was optimized in order to maximize the correlation on a test data sample and had been fixed for later data sets. In an update of this analysis a correlation fraction of $P_{\mathrm{corr}} = 31^{+5}_{-4}\,\%$ [125] is measured from a total amount of 106 events. Two subset energy regions with $55\,EeV \leq E \leq 70\,EeV$ with 66 events and $E > 70\,EeV$ with 40 events give $P_{\mathrm{corr}} = 41^{+6}_{-6}\,\%$ and $P_{\mathrm{corr}} = 15^{+6}_{-5}\,\%$, respectively. The comparison with the isotropic expectation of $P^{iso}_{\mathrm{corr}} = 21\,\%$ shows for the lower energy range a deviation from the isotropic expectation at a 99.7 % confidence level.

7.2 Impact of the Expansion of the Universe

The simulation of deflection of cosmic rays in extragalactic magnetic fields with CRPropa 2.0 do not allow to consider effects associated with the expansion of the universe as already described in Sec. 4.1. Anyhow, since at the energies $E > 55\,\mathrm{EeV}$ where an indication of an anisotropy is observed in the data, the main contribution of cosmic rays should arise from the nearby universe and hence should not suffer strongly from cosmological effects. To give an idea of the quantitative impact of the expansion of the universe a simple test is performed. For this purpose one dimensional simulations with and without consideration of this effect as described in Sec. 2.4.4 are compared. The uniform four mass component source scenario with parameters fixed by the combined fit to the energy spectrum and X_{max} moments measured by the Pierre Auger Collaboration as used in Sec. 5.2.2 is considered. Figure 7.1 shows the ratio of the observed energy spectrum and the X_{max} moments from simulations with and without considering the effects of the expansion of the universe. As mentioned, an indication of a deviation from isotropy is seen in the data for $E \geq 55\,\mathrm{EeV}$. For these energies the effect of the expansion is below 20 % for the cosmic ray flux and below 10 % for $\langle X_{\mathrm{max}} \rangle$ and $\sigma(X_{\mathrm{max}})$ as can be seen in Fig. 7.1. A more accurate treatment of this comparison is done in [174] where three dimensional simulation considering extension of the cosmic ray path length due to deflections in extra galactic magnetic fields and effects from the expansion of the universe are compared with simulation only considering the effects from deflections in magnetic fields. These studies show a even smaller impact of the expansion of the universe at energies above 55 EeV which justifies to neglect of cosmological effects throughout this chapter.

7.3 Simulation

7.3.1 Assumption for Simulations

For the directional studies in this chapter the 'standard proton', the 'standard HHeNFe' and the 'HHeNFe + near proton' scenarios from chapter 5 are considered. The source properties spectral index, maximum rigidity and mass composition are chosen according to the results of the combined energy spectrum and $\langle X_{\mathrm{max}} \rangle$ fit performed in that chapter.

To obtain directional information, three dimensional tracking of the cosmic ray particle trajectories have to be considered in the simulation. This introduces additional model parameters for the astrophysical scenarios namely extragalactic (EGMF) and galactic magnetic fields (GMF), the density of point sources and the distribution of the sources relative to the observer and to the EGMF.

For extragalactic magnetic fields, especially in voids, only predictions from large scale structure simulations (LSS) exists as described in Sec. 2.2. Different contemporary models show several orders of magnitudes differences in the predicted magnetic field strength. To take these uncertainties into account, models with strong and weak

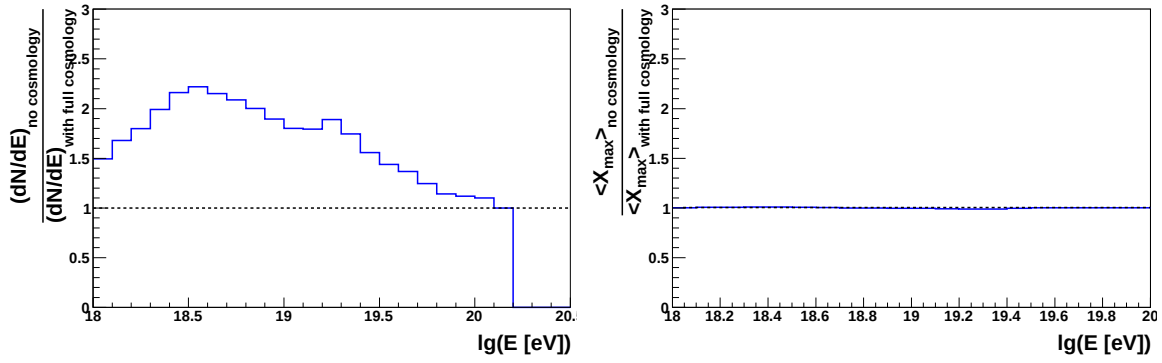

(a) energy spectrum

(b) $\langle X_{\max} \rangle$

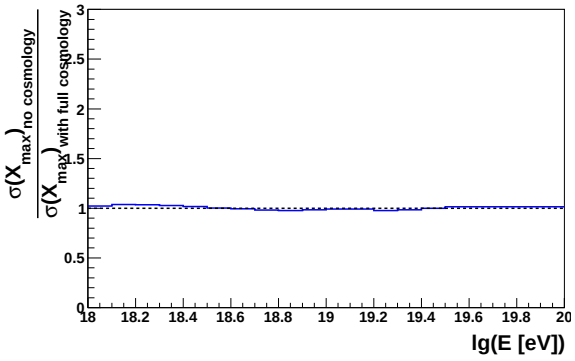

(c) $\sigma(X_{\max})$

Figure 7.1: Test of the effect of the expansion of the universe on the energy spectrum **(a)** and the first two $X_{\max}$ **(b,c)** moments. Shown are the ratios from a simulation without and with cosmological effects. The parameters of the simulation are chosen for the second minimum in the GCRSC simulation done in Sec. 5.2.2.

magnetic fields by Miniati et al. [84] and by Dolag et al. [81] are used in this work. From these two LSS simulations cubic magnetic field map with a side length of 75 Mpc and a resolution of 0.3 Mpc are used in the propagation simulation to calculate the deflection. This 75 Mpc cube pose the primary simulation volume and periodic boundary conditions enables to simulate the more distant universe as described in Sec. 4.1. Sec. 2.2 delivers more details about the EGMF, the models used in this work and the technical details for their implementation.

Both LSS simulations do not allow to use catalogues of real astrophysical objects. The mass distribution of Miniati et al. is by construction not aimed to mimic the real universe. Although Dolag et al. do follow roughly the observed matter distribution, the low accuracy prevents the observed mass distribution to coincide with the mass distribution from the LSS simulation to a reasonable degree. The distribution of the AGN from the the VCV catalog is also related to the nearby mass distribution in

the Universe. Hence, the source positions in the cosmic ray propagation simulations are randomly chosen according to the mass density distribution of the related LSS simulation. The source density used in the simulation is the same one given for the VCV within 75 Mpc with $\rho = 2.67 \cdot 10^{-4}\,\mathrm{Mpc}^{-3}$. This source density is well above the lower bounds of $10^{-6} - 10^{-5}\,\mathrm{Mpc}^{-3}$ found by Takami et al. [199] and also agrees with the lower bound of $(0.2 - 7) \cdot 10^{-4}\,\mathrm{Mpc}^{-3}$ given by Abreu et al. [200]. To realize this density, 112 sources are set in the first simulation volume. This results in 445 sources for the Miniati et al. density field and 475 sources for the Dolag et al. density field within 75 Mpc of the observer which leads to $\rho = 2.52 \cdot 10^{-4}\,\mathrm{Mpc}^{-3}$ and $\rho = 2.69 \cdot 10^{-4}\,\mathrm{Mpc}^{-3}$, respectively. On large scales, this construction leads to a uniform source distribution. In fact, it is more likely that only sub types of AGNs as for example radio loud AGN galaxies with a source density of $10^{-9} - 10^{-4}\,\mathrm{Mpc}^{-3}$ [101] could be the sources of cosmic rays. For these scenarios further studies should be done which could for example consider only a sub catalog of the VCV catalog. For this purpose the correlation fraction with data could be taken from an analysis like done in [141]. In case of the magnetic field model from Miniati et al. the observer is positioned at an area with low magnetic field strength as found near the Milky Way. In case of the EGMF by Dolag et al. the Earth has a predetermined position at the centre of the simulation volume.

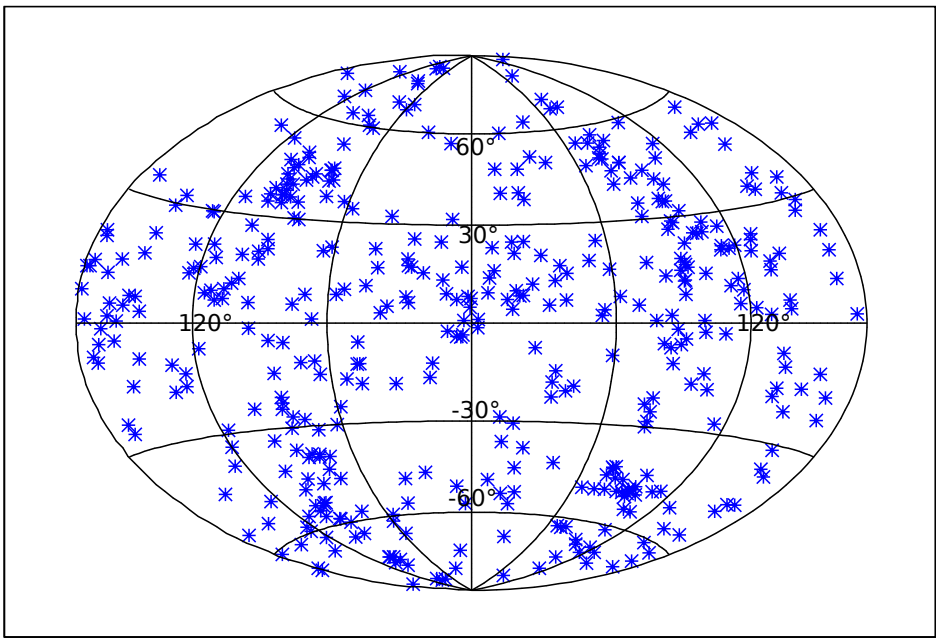

Figure 7.2: Sources positions in the simulation chosen according to the mass density from the LSS simulation by Miniati et al. [84] displayed in an Aitoff-Hammer projection in galactic coordinates.

As an example, the directions of the sources used for the Miniati magnetic field is shown in Fig. 7.2.

The deflection in the galactic magnetic field is taken into account by applying the

magnetic field lenses after the propagation simulation. This procedure is described in detail in Sec. 2.3. Throughout this work the GMF model derived by Jansson et al. [87, 88] is used as it shows a very good agreement with rotation measurements of the galactic magnetic field.

7.3.2 Directional exposure

The exposure in general gives the time integrated effective collecting area for a flux from each sky position for a cosmic ray observatory. It is usually given in units of $\mathrm{km}^2 \cdot \mathrm{year}$. From geometric considerations the exposure depends on the declination δ of the cosmic ray direction. In [201] the dimensionless relative exposure ω is given by the exposure from any point in the sky divided through the largest exposure on the sky. It has the following declination dependence

$$\omega(\delta) \propto \cos(a_0)\cos(\delta)\sin(\alpha_\mathrm{m}) + \alpha_\mathrm{m}\sin(a_0\sin(\delta)),$$

with

$$\alpha_\mathrm{m} = \begin{cases} 0 & \text{if } \xi > 1, \\ \pi & \text{if } \xi < -1 \\ \cos^{-1}(\xi) & \text{otherwise} \end{cases}$$

and

$$\xi = \frac{\cos(\Theta_\mathrm{m}) - \sin(a_0)\sin(\delta)}{\cos(a_0)\cos(\delta)}.$$

$\theta_\mathrm{m} = 60^\circ$ is the maximum zenith angle that ensure full efficiency and $a_0 = -35^\circ$ is the latitude of the Pierre Auger Observatory. This exposure is applied to the simulated events after considering the deflection of the GMF.

7.3.3 Reweighting Procedure

Performing three dimensional propagation simulation increases strongly the required CPU-time as only a small part of the cosmic rays emitted by the sources are observed by the detecting mechanism described in Sec. 4.1. To reduce the CPU-time, different optimizations are applied.

Since the main interest of the directional studies in this work is in the highest energetic cosmic rays, three dimensional simulations are performed only for cosmic rays source energies $E_\mathrm{src} > 40\,\mathrm{EeV}$. As already seen in Fig. 5.1, the horizon for cosmic rays decreases with increasing energies. A three dimensional simulation with a maximum propagation time of 2600 Mpc, a mixed HHeNFe composition and the extragalactic magnetic field by Miniati et al. shows no cosmic rays with propagation time above 1000 Mpc as seen in Fig. 7.3 for observed energies $E_\mathrm{obs} > 40\,\mathrm{EeV}$. Hence, the maximum propagation time for the simulations in this chapter is reduced to 1000 Mpc.

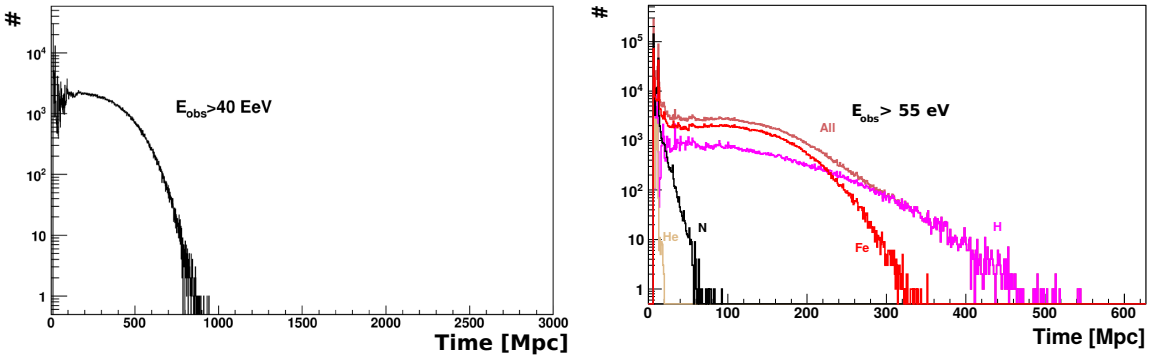

Figure 7.3: **Left:** Distribution of the propagation time of cosmic rays in a 3d simulation assuming the HHeNFe composition and the Miniati et al. EGMF [84] for a observed energy of $E_{\mathrm{obs}} > 40\,\mathrm{eV}$. **Right:** Same as in the left plot but for a minimum observed energy of $E_{\mathrm{obs}} > 55\,\mathrm{eV}$ and separated by nuclei at the source.

As described in Sec. 4.1 the detection mechanism of 3d simulations in CRPropa is realized by an observer sphere. For this sphere a compromise between collection efficiency and angular resolution has to be found. Here, an adaptive size of the observer is chosen for the simulation of each source that ensure an angular resolution of 1° corresponding to the resolution of the surface array of the Pierre Auger Observatory [124]. This allows to benefit from high observer sizes for more distant sources resulting in a higher detecting efficiency. As a rigidity dependent cut off is applied to the simulated events the maximum simulated energy is scaled with the atomic number.

As in the previous chapters, a reweighting of the simulated data considering the source energy and charge is used to reduce the simulation effort. The directional exposure of the the Pierre Auger Observatory which depends on the declination has to be applied for directional studies. For this purpose a reweighting in bins of declination was tested. Unfortunately, the statistic for such a procedure is not sufficient to avoid artefacts from the reweighting procedure. Instead the exposure is taken into account by rejecting cosmic rays with a probability proportional to the inverse of the exposure.

7.3.4 Calculation of Correlation Fraction

The fraction of arrival directions correlated with the simulated source positions within 3.1° is calculated for energies $E \geq 55\,EeV$ and for two subsequent intervals $55\,EeV \leq E \leq 70\,EeV$ and $E > 70\,EeV$. For each of these intervals the same amount of simulated events is used as found in the data. Although the same source density as in the VCV catalog is used in the simulations a deviating angular distribution of the sources leads to a slightly higher isotropic expectation of ${}^{\mathrm{sim}}P^{\mathrm{iso}}_{\mathrm{corr}} = 24\,\%$ in the case of Miniati et al. whereas for the Dolag et al. scenarios ${}^{\mathrm{sim}}P^{\mathrm{iso}}_{\mathrm{corr}} = 21\,\%$ is given as found for the VCV catalog.

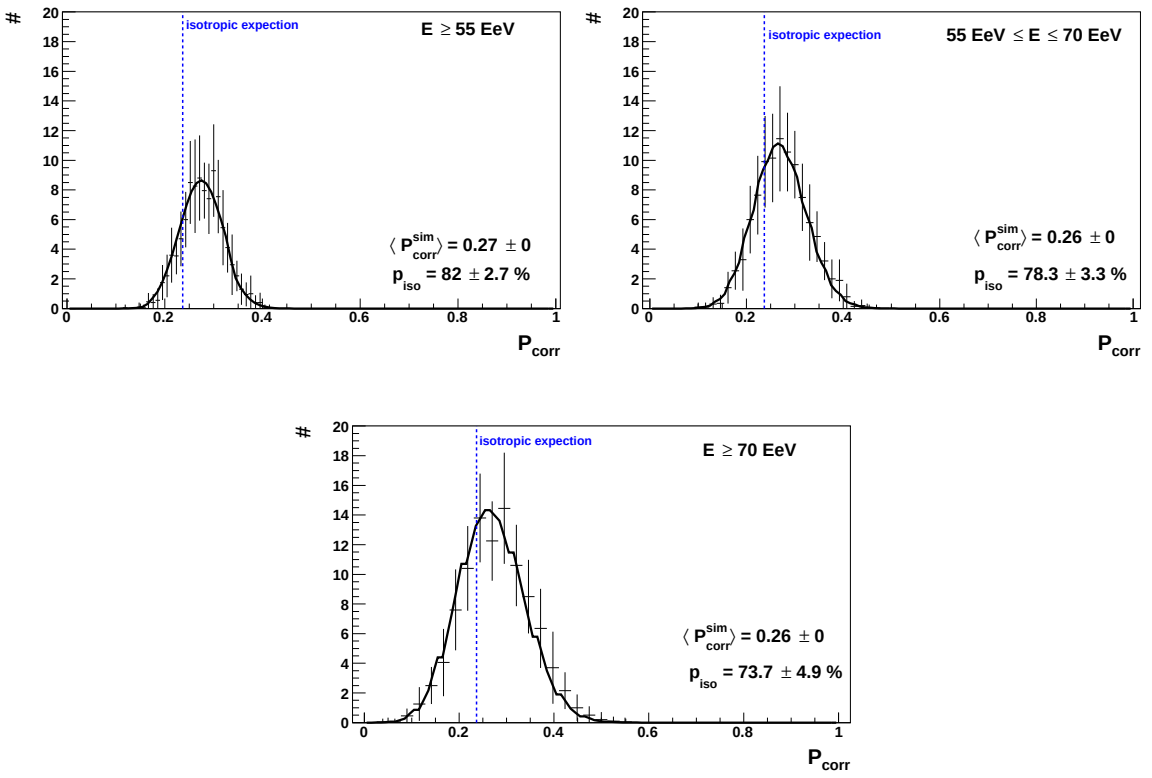

Figure 7.4: Distribution of the correlation fraction from 100 simulations where the points displaying the average and RMS for bins in the correlation fraction from a shuffling procedure as described in the text. The solid line shows the fit of a binomial distribution to the points to obtain the $\langle P_{\mathrm{corr}}^{\mathrm{sim}} \rangle$. The vertical blue dotted line indicates the isotropic expectation for the simulation. The results for the $\langle P_{\mathrm{corr}}^{\mathrm{sim}} \rangle$ and the p_{iso} as described in the text are given in the plot. The plot is shown for the three ranges in the observed energy $E \geq 55\,\mathrm{EeV}$ (**top left**), $55\,\mathrm{EeV} \leq E \leq 70\,\mathrm{EeV}$ (**top right**) and $E \geq 70\,\mathrm{EeV}$ (**bottom**). Pure proton sources and the EGMF by Miniati et al. [84] are used in the simulations. The source parameters are obtained from a combined fit as described in the text.

For each scenario this simulation is repeated 100 times with the same set of assumptions to take statistical fluctuations into account. This introduces a distribution of $P_{\mathrm{corr}}^{\mathrm{sim}}$. The comparison with isotropy is done calculating the proportion of realizations p_{iso} with $P_{\mathrm{corr}}^{\mathrm{sim}} >^{\mathrm{sim}} P_{\mathrm{corr}}^{\mathrm{iso}}$.

A direct comparison with data is only done for the simulation from Dolag et al., as only in this case the fraction of the sky covered by the catalog is the same as in data. For the comparison the proportion of realizations p_{data} with $P_{\mathrm{corr}}^{\mathrm{sim}} > P_{\mathrm{corr}}^{\mathrm{data}}$ is calculated.

To estimate the uncertainty due to a limited number of simulated realizations the

distribution of $P_{\mathrm{corr}}^{\mathrm{sim}}$ is recalculated with the simulated events shuffled 20 times. This gives the average and the standard deviation for each bin in $P_{\mathrm{corr}}^{\mathrm{sim}}$. This procedure is chosen as the simulation of a sufficient amount of events would not be possible in a reasonable amount of time.

$\langle P_{\mathrm{corr}}^{\mathrm{sim}} \rangle$ is derived by a fit of a binomial distribution to the distribution of the average $P_{\mathrm{corr}}^{\mathrm{sim}}$ with the standard deviation as uncertainty for each bin. For p_{iso} and p_{data} the mean and standard deviation are calculated from the 20 values of the shuffling procedure. We will rate a deviation as significant, when 95 % of the realizations are above the according $P_{\mathrm{corr}}^{\mathrm{iso}}$ or $P_{\mathrm{corr}}^{\mathrm{data}}$ values taking the uncertainties into account.

7.4 Results

At first, a scenario with the pure proton and HHeNFe sources as discussed in Sec. 5.2.2 is used for the predictions of the correlation fraction. The results are shown for a strong EGMF by Miniati et al. and then for the weaker EGMF by Dolag et al. Finally, the degree of anisotropy for the scenario with a near proton source in addition to the mixed HHeNFe sources is examined assuming again the strong EGMF. The source parameter spectral index, the maximum rigidity and the mass composition derived from the fit in chapter 5 are given in Tab. 7.1. The resulting correlation fraction, proportions of realizations above isotropy and below data are given in the tables Tab. 7.2–7.4.

We already mentioned that the VCV catalog can not be taken as a complete list of AGNs in contrast to the complete catalog of source positions from the simulation. Consequently the real $P_{\mathrm{corr}}^{\mathrm{data}}$ could be stronger than the measured ones. Due to this fact a significant higher $P_{\mathrm{corr}}^{\mathrm{sim}}$ in comparison to the according $P_{\mathrm{corr}}^{\mathrm{data}}$ can not directly be related to an exclusion of this scenario. On the other hand a scenario, which is too isotropic compared to data can be excluded.

In Sec. 5.2.2 and Sec. 5.2.7 two possible configurations of spectral index and maximum rigidity were found. The ability to discriminate between these two results by the correlation fraction is also tested.

EGMF by Miniati et al. Assuming pure proton sources, the correlation fraction of $P_{\mathrm{corr}}^{\mathrm{sim}} = 26$–$27\,\%$ is for all the three energy ranges is higher than the isotropic value of ${}^{\mathrm{sim}}P_{\mathrm{corr}}^{\mathrm{iso}} = 24\,\%$. But no significant excess from isotropy is seen in any energy range with a maximum of 82.6 % of the simulations being above the isotropic value for $E > 55\,\mathrm{EeV}$ as can be read from Fig. 7.4 and Tab. 7.2.

For the HHeNFe scenario no positive excess of correlated events from the isotropic expectation can be seen even for the highest energetic interval of $E > 70\,\mathrm{EeV}$. For the energy ranges $E > 55\,\mathrm{EeV}$ and $55\,\mathrm{EeV} < E < 70\,\mathrm{EeV}$ only $< 10.1\,\%$ of the events are above the isotropic expectation which seem to be an negative deviation from isotropy due to the magnetic fields itself as can be seen in Fig. 7.5. Both α–R_{max} combinations from the combined fit show nearly the same behavior yielding no discrimination due to the correlation fraction.

EGMF by Dolag et al. Assuming the EGMF by Dolag et al., a direct comparison to data is possible in addition to the comparison with the isotropic expectation. Figure 7.6 shows that in the proton source scenario a significant deviation from isotropy appears for all energy intervals. The comparison with data shows a lower correlation

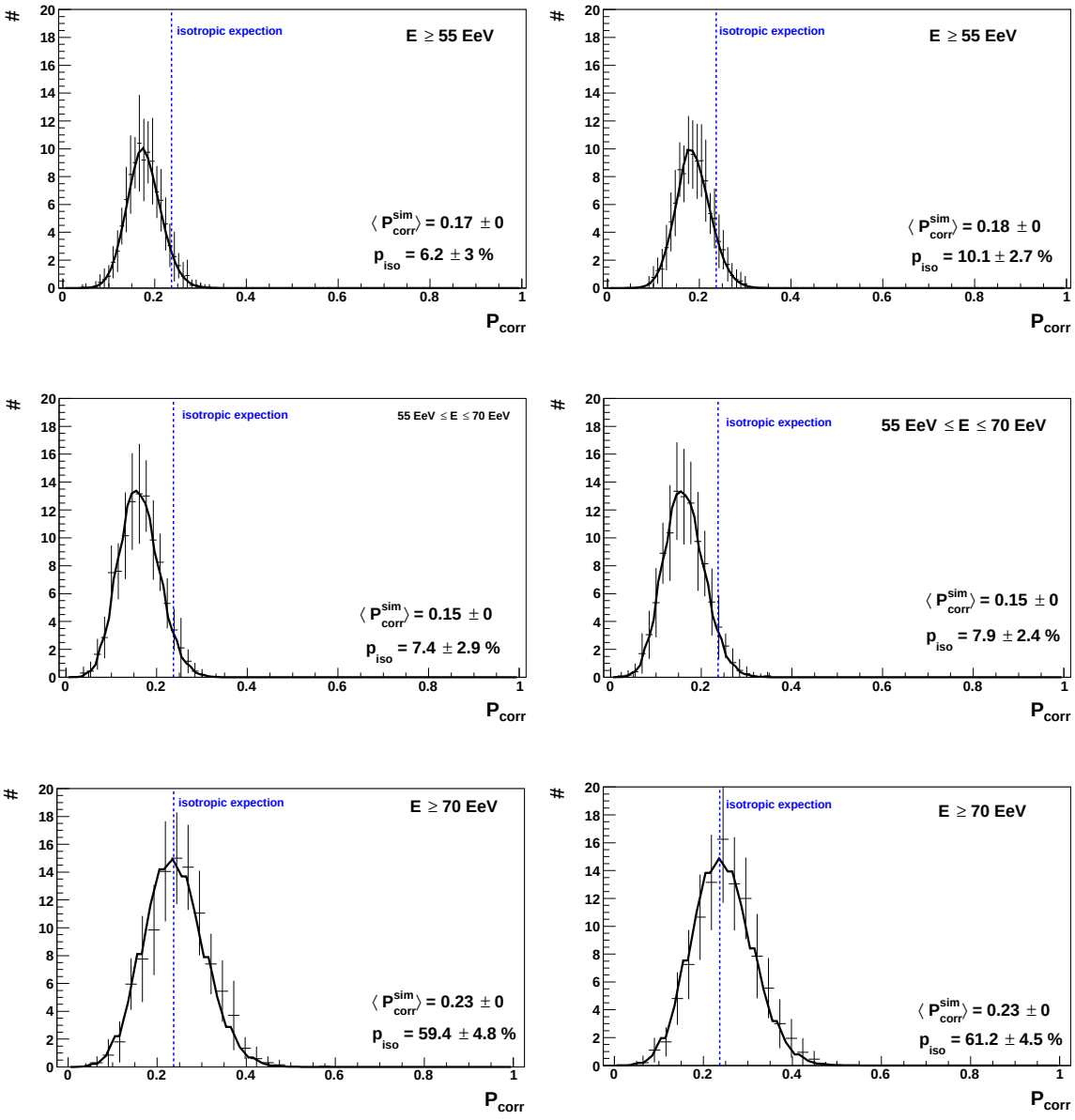

Figure 7.5: Same as Fig. 7.4 but using the HHeNFe composition with the parameters from the first minimum **(left column)** and second minimum **(right column)** of the combined fit as described in the text. The plot is shown for the three ranges in the observed energy $E \geq 55\,\mathrm{EeV}$, $55\,\mathrm{EeV} \leq E \leq 70\,\mathrm{EeV}$ and $E \geq 70\,\mathrm{EeV}$ (**from top to bottom**).

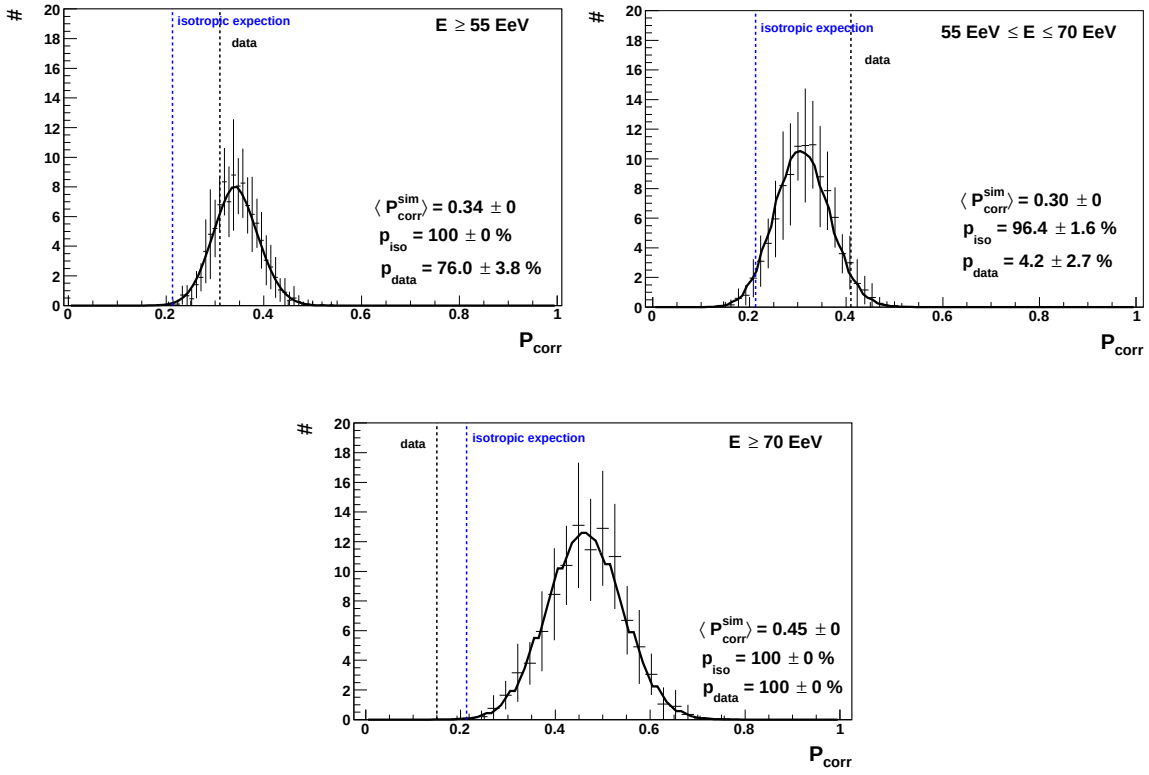

Figure 7.6: Same as Fig. 7.4 but with an additional vertical dotted black line that displays the correlation fraction obtained from data of the Pierre Auger Observatory [174]. Pure proton sources and the EGMF by Dolag et al. [81] are used in the simulation. Here, in addition the results for the p_{data} as described in the text are given.

for $55\,\mathrm{EeV} < E < 70\,\mathrm{EeV}$ and a significant higher for $E > 70\,\mathrm{EeV}$. As mentioned before, due to the incompleteness of the VCV catalog the upward excess can not be seen as an hard exclusion.

The four component source composition scenario shows no deviation from isotropy in all energy ranges as can be seen in Fig. 7.7.

Compared to data, the HHeNFe scenario shows significantly less correlation with the catalog for the intervals $E > 55\,\mathrm{EeV}$ and $55\,\mathrm{EeV} < E < 70\,\mathrm{EeV}$ and has a too large P_{corr} for $E > 70\,\mathrm{EeV}$. Again, no discrimination of the two minima can be made on bases of the correlation fraction.

Influence of an additional near proton source The scenario with a proton source at 4 Mpc distance in addition to the four component mixed source composition showed an improved description of the energy spectrum and the X_{max} moments in Sec. 5.2.7. This scenario has also the capability to show the correlation behavior seen in the data, having the near proton source responsible for the excess from anisotropy below 70 EeV

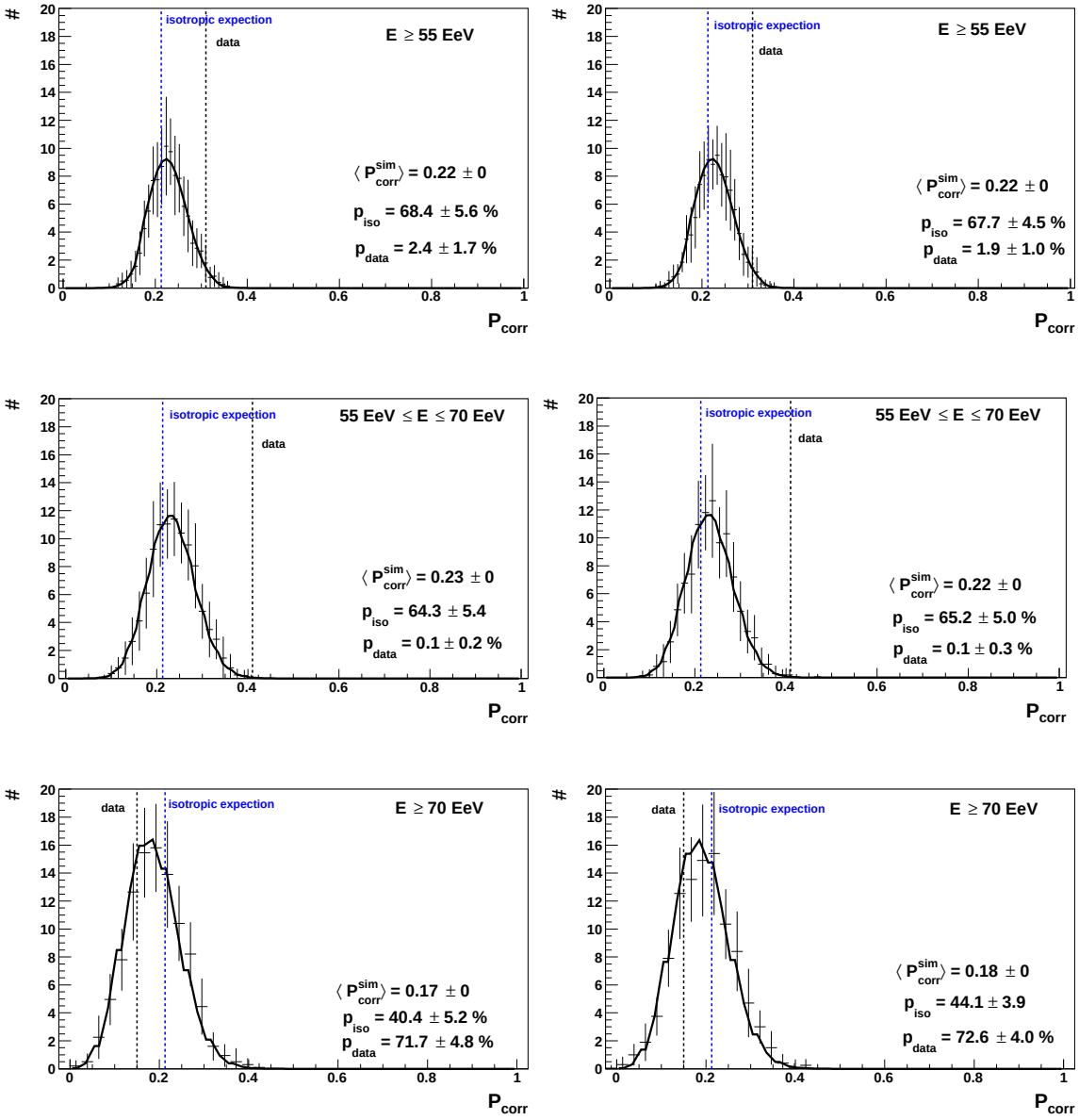

Figure 7.7: Same as Fig. 7.6 but using the HHeNFe composition with the source parameters obtained for the first minimum **(left column)** and the second minimum **(right column)** of the combined fit as described in the text. The plot is shown for the three ranges in the observed energy $E \geq 55\,\mathrm{EeV}$, $55\,\mathrm{EeV} \leq E \leq 70\,\mathrm{EeV}$ and $E \geq 70\,\mathrm{EeV}$ (**from top to bottom**).

and the heavier elements from the uniform mixed composition sources prohibiting the highest energetic events from correlating with the source positions. For this composition scenario the EGMF by Miniati et al. is used. Although in all energy intervals an increase of the correlation fraction is seen compared to the scenario without the near

proton source no significant excess from isotropy is seen in this scenario as displayed in Fig. 7.8. Especially the events with $55\,\mathrm{EeV} < E < 70\,\mathrm{EeV}$ which suggest a deviation from isotropy in data are in good agreement with isotropy in the simulation. The

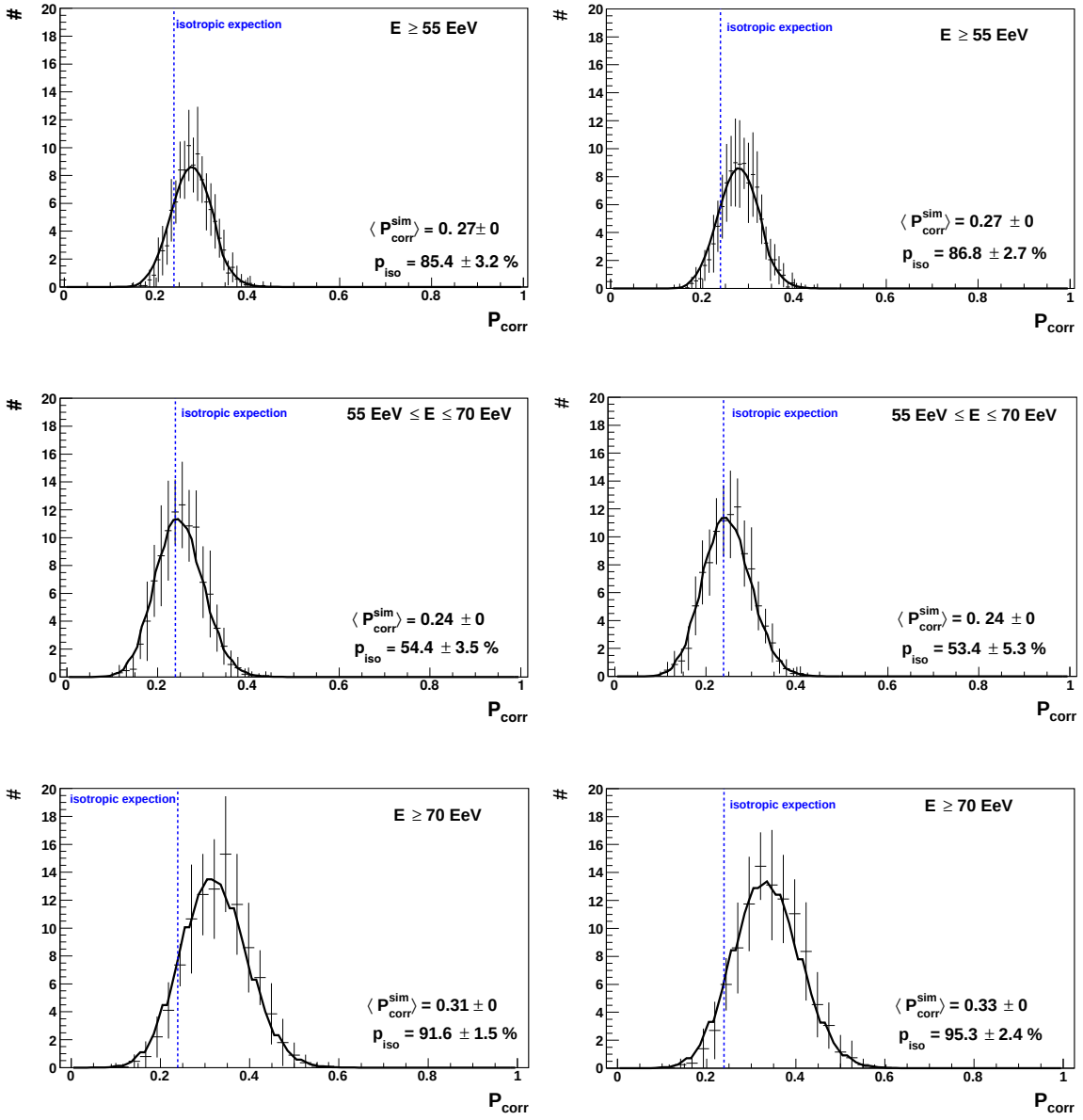

Figure 7.8: Same as Fig. 7.4 but using the HHeNFe composition and one proton source in the Cen A position with the parameters from the minimum **(left column)** and the second minimum **(right column)** of the combined fit as described in the text. The plot is shown for the three ranges in the observed energy $E \geq 55\,\mathrm{EeV}$, $55\,\mathrm{EeV} \leq E \leq 70\,\mathrm{EeV}$ and $E \geq 70\,\mathrm{EeV}$ (**from top to bottom**).

most energetic events on the other side still show an increase in p_{iso} which is also not compatible with the trend seen in data. This behavior can be explained by the near proton source that has a stronger contribution at the highest energies due to the small energy losses.

No discrimination between the two results form the combined fit is possible.

7.5 Summary and Conclusion

In this chapter the possibility to observe an anisotropy in the arrival direction of UHECR and the constrain of their source scenarios is studied with 3d simulations assuming individual astrophysical scenarios. For this purpose the correlation of the cosmic ray source directions with the source coordinates is studied analogue to the analysis done by the Pierre Auger Collaboration when comparing the measured UHECR arrival directions with the Véron-Cetty and Véron Catalog positions. In the simulations deflections are considered in galactic magnetic fields as well as in two scenarios of extragalactic magnetic fields derived from LSS simulations with a strong version by Minati et al. and a weak version by Dolag et al. where the source distribution from these LSS are also used for determining the source distributions. For each EGMF scenario the standard proton and HHeNFe scenario from Sec. 5.2.2 is chosen whereas for the Miniati et al. field also the scenario of a uniform HHeNFe distribution with a nearby proton source is discussed in addition. In every scenario the energy range $E > 55\,\mathrm{EeV}$ and the two subsequent ranges $55\,\mathrm{EeV} < E < 70\,\mathrm{EeV}$ and $E > 70\,\mathrm{EeV}$ are reviewed as done for the data.

The results for the strong EGMF by Miniati et al. show no significant deviation from isotropy in all scenarios, even not for pure proton sources for which the weakest deflections are expected. The weak EGMF derived by Dolag et al. leads to high deviations from isotropy in case of pure proton sources at the highest energies of $E > 70\,\mathrm{EeV}$ and for the whole energy range $E > 55\,\mathrm{EeV}$. Comparing directly with the data shows a clear overshot for the energy range $E > 70\,\mathrm{EeV}$. As the catalog used for the comparison to the data can not be seen as complete this behavior can not be regarded as significant. The mixed composition scenario along with the weak EGMF show good agreement with isotropy. Comparing with the data leads to an exclusion in the lower energy range of $55\,\mathrm{EeV} < E < 70\,\mathrm{EeV}$ and in the range $E > 55\,\mathrm{EeV}$ where in both energy ranges the simulation have a significant lower correlation fraction as the data.

Assuming an additional nearby proton source at 4 Mpc to the mixed HHeNFe scenario with the Miniati et al. EGMF show also no departure from isotropy.

Conclusively, only pure proton sources in combination with weak EGMFs exhibit deviations from isotropy assuming a realistic propagation simulation. The results show in no scenario an excess from isotropy for the energy range $55\,EeV \leq E \leq 70\,EeV$ in combination of an isotropic behavior for $E > 70\,\mathrm{EeV}$ as seen in Data. Direct comparison with data in case of the weak EGMF exclude the mixed HHeNFe source composition scenario.

	α	$\lg(R_{\max}/eV)$	χ^2/ndf
1)	-2.2	19.6	16.7 / 12

	α	$\lg(R_{\max}/eV)$	H	He	N	Fe	χ^2/ndf
2.1)	-0.0	18.4	76.9	3.6	19.4	0.1	137.3 / 27
2.1)	-1.9	19.7	0.0	0.0	74.5	25.5	193.9 / 27

	α	$\lg(R_{\max}/eV)$	H	He	N	Fe	$\alpha_{\text{near}}^{\text{proton}}$	$\lg({}^{\text{proton}}R_{\max}^{\text{near}}/eV)$	$s_{\text{near}}^{\text{proton}}$	χ^2/ndf
3.1)	-0.2	18.2	52.4	37.1	10.2	5.1	-2.3	19.3	83.0	51.3 / 24
3.2)	-1.2	18.5	1.8	28.4	62.3	7.5	-2.4	19.3	99.8	71.5 / 24

Table 7.1: Repetition of the source parameters as derived in Sec. 5.2.1, 5.2.2 and 5.2.7 for uniform proton sources **(1)**, for HHeNFe sources **(2)** and for HHeNFe sources with additional near proton population **(3)**, respectively.

scenario	$P_{\mathrm{corr}}^{\mathrm{iso}}$	$E > 55\,\mathrm{eV}$		$55\,\mathrm{eV} < E < 70\,\mathrm{eV}$		$E > 70\,\mathrm{eV}$	
		$p_{\mathrm{iso}}\,[\%]$	$P_{\mathrm{corr}}^{\mathrm{sim}}$	$p_{\mathrm{iso}}\,[\%]$	$P_{\mathrm{corr}}^{\mathrm{sim}}$	$p_{\mathrm{iso}}\,[\%]$	$P_{\mathrm{corr}}^{\mathrm{sim}}$
Proton	0.24	82.6 ± 2.7	0.27 ± 0	78.3 ± 3.3	0.26 ± 0	73.7 ± 4.9	0.26 ± 0
HHeNFe 1.min	0.24	6.2 ± 3	0.17 ± 0	7.4 ± 2.9	0.15 ± 0	59.4 ± 4.8	0.23 ± 0
HHeNFe 2.min	0.24	10.1 ± 2.7	0.18 ± 0	7.9 ± 2.4	0.15 ± 0	61.2 ± 4.5	0.23 ± 0

Table 7.2: Correlation fraction $P_{\mathrm{corr}}^{\mathrm{sim}}$, percentage of simulations sets above the isotropic expectation p_{iso} and percentage of simulations sets above the value from the data p_{data} for the three energy ranges and different composition scenarios. A strong EGMF from Miniati et al. is assumed.

scenario	$P_{\mathrm{corr}}^{\mathrm{iso}}$	$E > 55\,\mathrm{eV}$			$55\,\mathrm{eV} < E < 70\,\mathrm{eV}$			$E > 70\,\mathrm{eV}$		
		$p_{\mathrm{iso}}\,[\%]$	$p_{\mathrm{data}}\,[\%]$	$P_{\mathrm{corr}}^{\mathrm{sim}}$	$p_{\mathrm{iso}}\,[\%]$	$p_{\mathrm{data}}\,[\%]$	$P_{\mathrm{corr}}^{\mathrm{sim}}$	$p_{\mathrm{iso}}\,[\%]$	$p_{\mathrm{data}}\,[\%]$	$P_{\mathrm{corr}}^{\mathrm{sim}}$
Proton	0.21	100 ± 0	76 ± 3.8	0.34 ± 0	96.4 ± 1.6	4.2 ± 2.7	0.30 ± 0	100 ± 0	100 ± 0	0.45 ± 0
HHeNFe 1.min	0.21	68.4 ± 5.6	2.4 ± 1.7	0.22 ± 0	64.3 ± 5.4	0.1 ± 0.2	0.23 ± 0	40.4 ± 5.2	71.7 ± 4.8	0.17 ± 0
HHeNFe 2.min	0.21	67.7 ± 4.5	1.9 ± 1.0	0.22 ± 0	65.2 ± 5.0	0.1 ± 0.3	0.22 ± 0	44.1 ± 3.9	72.6 ± 4.0	0.18 ± 0

Table 7.3: Same as Fig. 7.2 but assuming a weak EGMF from Dolag et al.

scenario	$P_{\mathrm{corr}}^{\mathrm{iso}}$	$E > 55\,\mathrm{eV}$		$55\,\mathrm{eV} < E < 70\,\mathrm{eV}$		$E > 70\,\mathrm{eV}$	
		$p_{\mathrm{iso}}\,[\%]$	$P_{\mathrm{corr}}^{\mathrm{sim}}$	$p_{\mathrm{iso}}\,[\%]$	$P_{\mathrm{corr}}^{\mathrm{sim}}$	$p_{\mathrm{iso}}\,[\%]$	$P_{\mathrm{corr}}^{\mathrm{sim}}$
Cen A Proton plus HHeNFe bg 1.min	0.24	85.4 ± 3.2	0.27 ± 0	54.4 ± 3.5	0.24 ± 0	91.6 ± 1.5	0.31 ± 0
Cen A Proton plus HHeNFe bg 2.min	0.24	86.8 ± 2.7	0.27 ± 0	53.4 ± 5.3	0.24 ± 0	95.3 ± 2.4	0.33 ± 0

Table 7.4: Same as Fig. 7.2 but assuming a mixed HHeNFe scenario with a nearby proton source at 4 Mpc.

In addition, no discrimination is possible by the results in this chapter between the two minima in the α–E_{max} space of the combined fit from Sec. 5.2.2 for the mixed HHeNFe scenario and the HHENFe scenario with an additional nearby proton source.

8 Summary and Conclusion

The main question of this thesis is to which degree we can constrain astrophysical scenarios for the production and propagation of ultra high energetic cosmic rays taking into account a comprehensive collection of contemporary measurements in this field. The simulation code CRPropa is used for the propagation of cosmic rays from the sources as given by individual astrophysical scenarios to the observer on Earth to obtain observables to compare to the experimental measurements by the Pierre Auger Observatory.

First, one dimensional simulations are used to predict the energy spectrum, the $\langle X_{\mathrm{max}} \rangle$ and the $\sigma(X_{\mathrm{max}})$ for a simple standard astrophysical configuration with three different mass scenarios including pure proton sources, sources with four mass components (HHeNFe) and the galactic cosmic ray source composition (GCRSC) (chapter 5). A fit of the energy spectrum to the data above the ankle of the cosmic ray spectrum at $E > 10^{18.7}\,\mathrm{eV}$ yields a good agreement for all three source compositions. A galactic to extragalactic transition below $10^{18}\,\mathrm{eV}$ as predicted for proton sources is disfavoured by the fit. A combined fit of all three observables prefers a mixed mass composition at the cosmic rays sources. Assuming the energy spectrum at the source to follow a power-law, the spectral index of the power-law, the maximal rigidity and the mass composition at the sources are constrained by this fit. This results in two possible configurations. The first one has a very hard spectral index at $\alpha \in [-1, 0]$, a low maximum rigidity of $R_{\mathrm{max}} = 10^{18.4}\,\mathrm{eV}$ and a light mass composition. Although, acceleration for instance in pulsars predict a hard spectral index of $\alpha = -1$ even harder spectral indices are not predicted by any model. The second preferred combination is $\alpha = -1.9$, $R_{\mathrm{max}} = 10^{19.7}\,\mathrm{eV}$ and a heavy mass composition where the spectral index is in agreement with predictions from stochastic acceleration processes in the sources. A further result is that the high energy suppression of the cosmic ray flux as seen in the data of the Pierre Auger Observatory can not only be explained by the GZK effect. A positive evolution of the source density with redshift according to the one expected for a number of cosmic ray source candidates shows in nearly all cases a decrease of the fit quality compared to a uniform distribution. Subsequently, it is shown that considering effects from deflection in extragalactic magnetic fields during the propagation of cosmic rays improves the combined fit to the energy spectrum and the X_{max} moments. However, magnetic fields are only considered by an analytic approximation, which is valid for low energies and a more realistic study with 3d simulations considering also the expansion of the universe should be employed to confirm this results. An improved description of the data is achieved by introducing an additional source population to the standard HHeNFe scenario in particular at a distance of about 4 Mpc. In case of an additional nearby HHeNFe source the result with the hard spectral index can be

avoided as found in all other mixed scenarios.

Furthermore, 1d simulations are used to make predictions of the not yet observed ultra high energetic secondary photon and neutrino fluxes for a range of astrophysical scenarios with proton and iron sources where the combined fit of the energy spectrum and the $X_{\max}$ moments is used to determine the energy spectrum and maximum rigidity at the sources (chapter 6). The resulting predictions of both secondary fluxes are well below the current experimental upper limits and the expected sensitivities in the near future. Also the photon flux at GeV energies from these scenarios is below the flux measured by the Fermi experiment. Even though, only considering the current and future upper limits in the UHE range enables an independent constrain of the α and $R_{\max}$ range. Therefore, a comparison of the exclusion power of the photon and neutrino limits is done that show a clear advantage of the neutrino limit especially for the future. As photon and neutrino fluxes are sensitive to different distance ranges in the future they could constrain complementary source distributions. Recalculating the constraining power from photon fluxes for a scenario with only a nearby source population show an improved exclusion of α–$R_{\max}$ combinations which is due to the low energy loss length of UHE photons. Although it is not possible to put already additional constraints to the results of the combined fit, future upper limits could allow to put harder constraints for scenarios dominated by nearby sources. This is in particular interesting as an additional nearby source population is preferred by the combined fit. As the neutrino flux shows a high sensitivity for the distant universe this could be used in the future to distinguish between different source evolution models that show a higher deviation from each other in the neutrino flux for high redshift.

In the final part, 3d simulations are performed to study the directional behavior of UHECR (chapter 7). Therefore, the fraction of observed UHECR directions correlated with the original source positions are used as done for the measured data by the Pierre Auger Collaboration [202, 125] where coincidences with a catalogue of AGNs were suggested for the energies $E > 55\,\mathrm{EeV}$ and $55\,\mathrm{EeV} < E < 70\,\mathrm{EeV}$ and an isotropic signal for $E > 70\,\mathrm{EeV}$. In a first step, the possibility to detect an anisotropic signal for an astrophysical scenario taking into account galactic and extragalactic magnetic fields as well as source positions according to LSS is studied. In a second step also a comparison with the analysis which is done with measured data is carried out. The standard proton and HHeNFe scenario as well as the HHeNFe scenario with an additional nearby proton source are used with the associated parameters for the source properties resulting from the individual combined fits. Assuming a strong EGMF the results show no significant positive deviation from isotropy for all studied mass scenarios. For a weak EGMF and proton sources a significant deviation from isotropy is shown that increases with energy and is also stronger as seen in the data. The mixed source composition with the weak EGMF show no deviation from isotropy for all energy ranges. The results from the direct comparison to the data which is done for the scenarios with the weak EGMF shows for the HHeNFe sources a significant lower correlation for low energies and the whole energy range which leads to an exclusion of this scenario whereas proton sources can not be excluded. To summarise, a deviation from isotropy is seen only for pure proton sources in case of weak EGMF and none of

the studied scenarios can reproduce the behaviour seen in data whereby this leads to an significant exclusion for the scenario with HHeNFe sources and the weak EGMF.

Regarding the issue of the two minima found in the combined fit of the energy spectrum and the X_{max} moments for the HHeNFe scenarios, photon predictions as well as neutrino predictions do not allow to distinguish between these two results at the current status of the experimental upper limits. In particular, further improvements of the neutrino limits could provide additional insights. Also the estimation of the correlation of the arrival directions with the source positions for this scenario shows no preference for one of the two minima of the combined fit.

Conclusively, a sophisticated simulation of astrophysical scenarios combined with a high data volume gathered by current experiments like the Pierre Auger Observatory allow to thin out the mists that obscures the sources of UHECR. But still the combination of the individual observables contains challenges as for example the energy spectrum and the X_{max} moments prefer mixed sources especially with an additional nearby population but the absence of an anisotropy for this scenarios disfavours them in the directional studies. Future studies with more advance simulation possibilities and more complex astrophysical scenarios will perhaps also solve this last obstacles.

Bibliography

[1] V. Hess and W. Kolhoerster, "Über die Beobachtung der durchdringenden Strahlung bei sieben Freiballonfahreten," *Physikalische Zeitschrift*, vol. 13, p. 1084, 1912.

[2] K.-H. Kampert *et al.*, "CRPropa 2.0 – a Public Framework for Propagating High Energy Nuclei, Secondary Gamma Rays and Neutrinos," *Astroparticle Physics*, vol. 42, pp. 41–51, 2013.

[3] T. Wulf *Physikalische Zeitschrift*, vol. 10, p. 997, 1909.

[4] J. Clay *Amsterdam Proceedings*, vol. 33, p. 711, 1930.

[5] W. Bothe and W. Kolhörster, "Das Wesen der Höhenstrahlung," *Zeitschrift für Physik*, vol. 56, no. 11-12, pp. 751–777, 1929.

[6] W. Kolhörster *et al. Naturwissenschaften*, vol. 26, p. 576, 1938.

[7] P. Auger and R. Maze, "Les grandes gerbes cosmiques de l'atmosphère," *Comptes rendus hebdomadaires des séances de l'Académie des sciences*, vol. 207, pp. 228–230, 1938.

[8] H. L. Bradt and B. Peters, "Investigation of the Primary Cosmic Radiation with Nuclear Photographic Emulsions," *Physical Review*, vol. 74, pp. 1828–1837, Dec 1948.

[9] M. Schein, W. P. Jesse, and E. O. Wollan, "The Nature of the Primary Cosmic Radiation and the Origin of the Mesotron," *Physical Review*, vol. 59, pp. 615–615, Apr 1941.

[10] G. Kulikov and G. Khristiansen *Journal of Experimental and Theoretical Physics*, vol. 35, p. 635, 1958.

[11] J. Linsley, "Evidence for a Primary Cosmic-Ray Particle with Energy 10^{20} eV," *Physical Review Letters*, vol. 10, pp. 146–148, Feb 1963.

[12] C. J. Bell *et al. Journal of Physics A*, vol. 12, p. 990, 1974.

[13] D. M. Edge, A. C. Evans, and H. J. Garmston *Journal of Physics A*, vol. 6, p. 1612, 1973.

[14] B. N. Afanasiev *et al. Proceedings of the Tokyo Workshop on Techniques for the Study of Extremly High Energy Cosmic Rays*, p. 353, 2003.

[15] N. Chiba *et al.*, "Akeno Giant Air Shower Array (AGASA) covering 100 km2 area," *Nuclear Instruments and Methods in Physics Research Section A: Accelerators, Spectrometers, Detectors and Associated Equipment*, vol. 311, no. 1–2, pp. 338–349, 1992.

[16] R. Baltrusaitis *et al.*, "The Utah Fly's Eye detector," *Nuclear Instruments and Methods in Physics Research Section A: Accelerators, Spectrometers, Detectors and Associated Equipment*, vol. 240, no. 2, pp. 410–428, 1985.

[17] C. D. Anderson, "The Positive Electron," *Physical Review*, vol. 43, pp. 491–494, Mar 1933.

[18] S. H. Neddermeyer and C. D. Anderson, "Note on the Nature of Cosmic-Ray Particles," *Physical Review*, vol. 51, pp. 884–886, May 1937.

[19] C. Lattes, G. Occhialini, and C. Powell, "Observations on the Tracks of Slow Mesons in Photographic Emulsions. 1," *Nature*, vol. 160, pp. 453–456, 1947.

[20] J. Bluemer, R. Engel, and J. R. Hoerandel, "Cosmic Rays from the Knee to the Highest Energies," *Progress in Particle and Nuclear Physics*, vol. 63, pp. 293–338, 2009.

[21] W. D. Apel *et al.*, "Kneelike Structure in the Spectrum of the Heavy Component of Cosmic Rays Observed with KASCADE-Grande," *Physical Review Letters*, vol. 107, p. 171104, Oct 2011.

[22] B. Peters, "Primary cosmic radiation and extensive air showers," *Il Nuovo Cimento*, vol. 22, no. 4, pp. 800–819, 1961.

[23] K. Greisen, "End to the cosmic ray spectrum?," *Physical Review Letters*, vol. 16, pp. 748–750, 1966.

[24] G. Zatsepin and V. Kuzmin, "Upper limit of the spectrum of cosmic rays," *Journal of Experimental and Theoretical Physics Letters*, vol. 4, pp. 78–80, 1966.

[25] D. Allard, E. Parizot, and A. Olinto, "On the transition from galactic to extragalactic cosmic-rays: spectral and composition features from two opposite scenarios," *Astroparticle Physics*, vol. 27, pp. 61–75, 2007.

[26] T. Wibig and A. W. Wolfendale, "At what particle energy do extragalactic cosmic rays start to predominate?," *Journal of Physics*, vol. G31, pp. 255–264, 2005.

[27] V. Berezinsky, A. Gazizov, and S. Grigorieva, "On astrophysical solution to ultrahigh energy cosmic rays," *Physical Review D*, vol. 74, p. 043005, Aug 2006.

[28] W. Apel *et al.*, "The KASCADE-Grande experiment," *Nuclear Instruments and Methods in Physics Research Section A: Accelerators, Spectrometers, Detectors and Associated Equipment*, vol. 620, no. 2–3, pp. 202–216, 2010.

[29] Abbasi *et al.*, "Indications of Proton-Dominated Cosmic-Ray Composition above 1.6 EeV," *Physical Review Letters*, vol. 104, p. 161101, Apr 2010.

[30] K.-H. Kampert and M. Unger, "Measurements of the Cosmic Ray Composition with Air Shower Experiments," *Astroparticle Physics*, vol. 35, pp. 660–678, 2012.

[31] Amenomori *et al.*, "Anisotropy and Corotation of Galactic Cosmic Rays," *Science*, vol. 314, no. 5798, pp. 439–443, 2006.

[32] Abdo *et al.*, "Discovery of Localized Regions of Excess 10-TeV Cosmic Rays," *Physical Review Letters*, vol. 101, p. 221101, Nov 2008.

[33] R. Abbasi *et al.*, "Measurement of the Anisotropy of Cosmic Ray Arrival Directions with IceCube," *The Astrophysical Journal*, vol. 718, p. L194, 2010.

[34] R. Abbasi *et al.*, "Observation of an Anisotropy in the Galactic Cosmic Ray arrival direction at 400 TeV with IceCube," *The Astrophysical Journal*, vol. 746, p. 33, 2012.

[35] P. Abreu *et al.*, "A Search for Point Sources of EeV Neutrons," *The Astrophysical Journal*, vol. 760, p. 148, 2012.

[36] B. W. Carroll and D. A. Ostlie, *An Introduction to Modern Astrophysics*. Addison-Wesley, 1996.

[37] C. T. Hill, "Monopolonium," *Nuclear Physics B*, vol. 224, no. 3, pp. 469–490, 1983.

[38] M. Hindmarsh and T. Kibble, "Cosmic strings," *Reports on Progress in Physics*, vol. 58, pp. 477–562, 1995.

[39] V. Berezinsky, M. Kachelriess, and A. Vilenkin, "Ultrahigh-energy cosmic rays without GZK cutoff," *Physical Review Letters*, vol. 79, pp. 4302–4305, 1997.

[40] M. Birkel and S. Sarkar, "Extremely high-energy cosmic rays from relic particle decays," *Astroparticle Physics*, vol. 9, no. 4, pp. 297–309, 1998.

[41] T. J. Weiler, "Cosmic ray neutrino annihilation on relic neutrinos revisited: A Mechanism for generating air showers above the Greisen-Zatsepin-Kuzmin cutoff," *Astroparticle Physics*, vol. 11, pp. 303–316, 1999.

[42] D. Fargion, B. Mele, and A. Salis, "Ultrahigh-energy neutrino scattering onto relic light neutrinos in galactic halo as a possible source of highest energy extragalactic cosmic rays," *The Astrophysical Journal*, vol. 517, pp. 725–733, 1999.

[43] Abraham *et al.*, "Upper limit on the cosmic-ray photon flux above 10^{19} eV using the surface detector of the Pierre Auger Observatory," *Astroparticle Physics*, vol. 29, no. 4, pp. 243–256, 2008.

[44] M. S. (for the Pierre Auger Collaboration), "An up-date on a search for ultra-high energy photons using the Pierre Auger Observatory," *Proceedings* 32^{nd} *ICRC (Bejing), 2011*, 2011.

[45] W. F. G. Swann, "A Mechanism of Acquirement of Cosmic-Ray Energies by Electrons," *Physical Review*, vol. 43, pp. 217–220, Feb 1933.

[46] T. K. Gaisser, *Cosmic rays and particle physics*. Cambridge University Press, 1990.

[47] E. Fermi, "On the Origin of the Cosmic Radiation," *Physical Review*, vol. 75, pp. 1169–1174, 1949.

[48] R. Blandford and J. Ostriker, "Particle Acceleration by Astrophysical Shocks," *The Astrophysical Journal*, vol. 221, pp. L29–L32, 1978.

[49] P. Sokolsky, *Introduction ro ultrahigh-energetic Cosmic Ray physics*. Addison-Wesley, 1989.

[50] K. Kotera and A. V. Olinto, "The Astrophysics of Ultrahigh Energy Cosmic Rays," *Annual Review of Astronomy and Astrophysics*, vol. 49, pp. 119–153, 2011.

[51] A. Hillas, "The Origin of Ultrahigh-Energy Cosmic Rays," *Annual Review of Astronomy and Astrophysics*, vol. 22, pp. 425–444, 1984.

[52] K. V. Ptitsyna and S. V. Troitsky, "Physical conditions in potential sources of ultra-high-energy cosmic rays. I. Updated Hillas plot and radiation-loss constraints," *Physics-Uspekhi*, vol. 53, pp. 691–701, 2010.

[53] M. Ackermann, *Searches for signals from cosmic point-like sources of high energy neutrinos in 5 years of AMANDA-II data* . PhD thesis, 2006.

[54] C. M. Urry and P. Padovani, "Unified Schemes for Radio-Loud Active Galactic Nuclei," *Publications of the Astronomical Society of the Pacific*, vol. 107, no. 715, pp. pp. 803–845, 1995.

[55] B. L. Fanaroff and J. M. Riley, "The Morphology of Extragalactic Radio Sources of High and Low Luminosity," *Monthly Notices of the Royal Astronomical Society*, vol. 167, no. 1, pp. 31P–36P, 1974.

[56] P. Bhattacharjee and G. Sigl, "Origin and propagation of extremely high-energy cosmic rays," *Physics Reports*, vol. 327, pp. 109–247, 2000.

[57] D. F. Torres and L. A. Anchordoqui, "Astrophysical origins of ultrahigh energy cosmic rays," *Reports on Progress in Physics*, vol. 67, pp. 1663–1730, 2004.

[58] J. Lattimer and M. Prakash, "The physics of neutron stars," *Science*, vol. 304, pp. 536–542, 2004.

[59] J. Arons, "Magnetars in the metagalaxy: an origin for ultrahigh-energy cosmic rays in the nearby universe," *The Astrophysical Journal*, vol. 589, pp. 871–892, 2003.

[60] E. Waxman, "Cosmological Gamma-Ray Bursts and the Highest Energy Cosmic Rays," *Physical Review Letters*, vol. 75, pp. 386–389, Jul 1995.

[61] M. Vietri, "Coronal gamma-ray bursts as the sources of ultrahigh-energy cosmic rays?," *Monthly Notices of the Royal Astronomical Society*, vol. 278, p. L1, 1996.

[62] R. J. van Weeren *et al.*, "Particle Acceleration on Megaparsec Scales in a Merging Galaxy Cluster," *Science*, vol. 330, no. 6002, pp. 347–349, 2010.

[63] V. Wild *et al.*, "Post-starburst galaxies: more than just an interesting curiosity," *Monthly Notices of the Royal Astronomical Society*, vol. 395, no. 1, pp. 144–159, 2009.

[64] L. A. Anchordoqui, G. E. Romero, and J. A. Combi, "Heavy nuclei at the end of the cosmic ray spectrum?," *Physical Review*, vol. D60, p. 103001, 1999.

[65] K. Kotera, D. Allard, and A. Olinto, "Cosmogenic Neutrinos: parameter space and detectabilty from PeV to ZeV," *Journal of Cosmology and Astroparticle Physics*, vol. 1010, p. 013, 2010.

[66] A. M. Hopkins and J. F. Beacom, "On the Normalization of the Cosmic Star Formation History," *The Astrophysical Journal*, vol. 651, no. 1, p. 142, 2006.

[67] H. Yuksel *et al.*, "Revealing the High-Redshift Star Formation Rate with Gamma-Ray Bursts," *The Astrophysical Journal Letters*, vol. 683, no. 1, p. L5, 2008.

[68] T. Le and C. D. Dermer, "Gamma Ray Bursts in the Swift and GLAST Era," *AIP Conference Proceedings*, vol. 921, pp. 462–463, 2007.

[69] J. V. Wall *et al.*, "The Parkes quarter-Jansky flat-spectrum sample," *Astronomy and Astrophysics*, vol. 434, no. 1, pp. 133–148, 2005.

[70] M. Ahlers, L. A. Anchordoqui, and S. Sarkar, "Neutrino diagnostics of ultrahigh energy cosmic ray protons," *Physical Review D*, vol. 79, p. 083009, Apr 2009.

[71] D. Coward, R. Burman, and D. Blair, "Statistical characteristics of a stochastic background of gravitational waves from neutron star formation," *Classical and Quantum Gravity*, vol. 19, no. 7, p. 1303, 2002.

[72] F. Daigne, E. M. Rossi, and R. Mochkovitch, "The Redshift distribution of long Gamma-Ray Bursts," *AIP Conference Proceedings*, vol. 836, pp. 546–551, 2006.

[73] T. Piran, D. Guetta, and M. Rodriguez Martinez, "Gamma-ray bursts and new physics," *Progress of Theoretical Physics Supplement*, vol. 163, pp. 23–37, 2006.

[74] F. Y. Wang and Z. G. Dai, "High-redshift star formation rate up to z 8.3 derived from gamma-ray bursts and influence of background cosmology," *Monthly Notices of the Royal Astronomical Society: Letters*, vol. 400, no. 1, pp. L10–L14, 2009.

[75] V. Beckmann *et al.*, "The HRX-BL Lac sample – Evolution of BL Lac objects," *Astronomy and Astrophysics*, vol. 401, no. 3, pp. 927–938, 2003.

[76] T. E. Clarke, "Faraday Rotation Observations of Magnetic Fields in galaxy Clusters," *Journal of the Korean Astronomical Society*, vol. 37, pp. 337–342, 2004.

[77] Y. Xu *et al.*, "A Faraday Rotation Search for Magnetic Fields in Large Scale Structure," *The Astrophysical Journal*, vol. 637, pp. 19–26, 2006.

[78] L. Biermann, "," *Zeitschrift für Naturforschung*, vol. A5, p. 65, 1950.

[79] G. Sigl, F. Miniati, and T. A. Ensslin, "Ultrahigh energy cosmic ray probes of large scale structure and magnetic fields," *Physical Review*, vol. D70, p. 043007, 2004.

[80] G. Sigl, F. Miniati, and T. Ensslin, "Cosmic magnetic fields and their influence on ultra-high energy cosmic ray propagation," *Nuclear Physics B: Proceedings Supplements*, vol. 136, pp. 224–233, 2004. [,224(2004)].

[81] K. Dolag *et al.*, "Constrained simulations of the magnetic field in the local Universe and the propagation of UHECRs," *Journal of Cosmology and Astroparticle Physics*, vol. 0501, p. 009, 2005.

[82] J. Donnert *et al.*, "Cluster Magnetic Fields from Galactic Outflows," *Monthly Notices of the Royal Astronomical Society*, vol. 392, pp. 1008–1021, 2009.

[83] D. Ryu, S. Das, and H. Kang, "Intergalactic Magnetic Field and Arrival Direction of Ultra-High-Energy Protons," *The Astrophysical Journal*, vol. 710, pp. 1422–1431, 2010.

[84] F. Miniati, "Inter-Galactic shock acceleration and the cosmic gamma-ray background," *Monthly Notices of the Royal Astronomical Society*, vol. 337, p. 199, 2002.

[85] D. Ryu *et al. The Astrophysical Journal*, vol. 414, pp. 1008–1021, 1993.

[86] R. Beck, "Magnetic fields in nearby galaxies: prospects with future radio telescopes," 2009.

[87] R. Jansson and G. R. Farrar, "A New Model of the Galactic Magnetic Field," *The Astrophysical Journal*, vol. 757, p. 14, 2012.

[88] R. Jansson and G. R. Farrar, "The Galactic Magnetic Field," *The Astrophysical Journal Letters*, vol. 761, no. 1, p. L11, 2012.

[89] X. H. Sun, "Radio observational constraints on Galactic 3D-emission models," *Astronomy and Astrophysics*, vol. 477, no. 2, pp. 573–592, 2008.

[90] T. Stanev, "Ultra-high-energy Cosmic Rays and the Large-scale Structure of the Galactic Magnetic Field," *The Astrophysical Journal*, vol. 479, no. 1, p. 290, 1997.

[91] D. Harari, S. Mollerach, and E. Roulet, "The Toes of the ultrahigh-energy cosmic ray spectrum," *Journal of High Energy Physics*, vol. 9908, p. 022, 1999.

[92] H.-P. Bretz *et al.*, "PARSEC: A Parametrized Simulation Engine for Ultra-High Energy Cosmic Ray Protons," *Astroparticle Physics*, vol. 54, pp. 110–117, 2014.

[93] D. Allard, "Extragalactic propagation of ultrahigh energy cosmic-rays," *Astroparticle Physics*, vol. 39-40, pp. 33–43, 2012.

[94] R. Abbasi *et al.*, "First observation of the Greisen-Zatsepin-Kuzmin suppression," *Physical Review Letters*, vol. 100, p. 101101, 2008.

[95] A. Aab *et al.*, "The Pierre Auger Observatory: Contributions to the 33rd International Cosmic Ray Conference (ICRC 2013)," 2013.

[96] M. Risse and P. Homola, "Search for ultra-high energy photons using air showers," *Modern Physics Letters*, vol. A22, pp. 749–766, 2007.

[97] T. C. Weekes, "Revealing the Dark TeV Sky: The Atmospheric Cherenkov Imaging Technique for Very High Energy Gamma-ray Astronomy," in *Energy budget in the high energy universe, proceedings of the International Workshop, Kashiwa, Japan, 22-24 February 2006*, pp. 282–302, 2006.

[98] H. Kolanoski, "Einführung in die Astroteilchenphysik." 2009.

[99] J. K. Becker, "High-energy neutrinos in the context of multimessenger physics," *Physics Reports*, vol. 458, pp. 173–246, 2008.

[100] D. N. Spergel *et al.*, "First-Year Wilkinson Microwave Anisotropy Probe (WMAP) Observations: Determination of Cosmological Parameters," *The Astrophysical Journal Supplement Series*, vol. 148, no. 1, p. 175, 2003.

[101] T. Winchen, *The Principal Axes of the Directional Energy Distribution of Cosmic Ray Measured with the Pierre Auger Observatory.* PhD thesis, 2013.

[102] B. G. Keilhauer, *Investigation of atmospheric effects on the development of extensive air showers and their detection with the Pierre Auger Observatory.* PhD thesis, Karlsruhe, Forschungszentrum, 2004.

[103] A. Letessier-Selvon and T. Stanev, "Ultrahigh energy cosmic rays," *Reviews of Modern Physics*, vol. 83, pp. 907–942, Sep 2011.

[104] W. Heitler, *Quantum Theory of Radiation.* Oxford University Press, 1944.

[105] P. Abreu *et al.*, "Interpretation of the Depths of Maximum of Extensive Air Showers Measured by the Pierre Auger Observatory," *Journal of Cosmology and Astroparticle Physics*, vol. 1302, p. 026, 2013.

[106] J. Matthews, "A Heitler model of extensive air showers," *Astroparticle Physics*, vol. 22, no. 5–6, pp. 387–397, 2005.

[107] T. Pierog *et al.*, "First results of fast one-dimensional hybrid simulation of EAS using CONEX," *Nuclear Physics B: Proceedings Supplements*, vol. 151, pp. 159–162, 2006.

[108] D. Kuempel, *Multivariate Search for a Directional Excess of EeV Photons with the Pierre Auger Observatory* . PhD thesis, 2010.

[109] "The Pierre Auger Project Design Report," 1996.

[110] J. Abraham *et al.*, "Measurement of the energy spectrum of cosmic rays above 1018 eV using the Pierre Auger Observatory," *Physics Letters B*, vol. 685, no. 4–5, pp. 239–246, 2010.

[111] J. Hersil *et al.*, "Observations of Extensive Air Showers near the Maximum of Their Longitudinal Development," *Physical Review Letters*, vol. 6, pp. 22–23, Jan 1961.

[112] A. Aab *et al.*, "The Pierre Auger Cosmic Ray Observatory," *Nuclear Instruments and Methods in Physics Research Section A: Accelerators, Spectrometers, Detectors and Associated Equipment*, 2015.

[113] D. Kuempel, K. H. Kampert, and M. Risse, "Geometry reconstruction of fluorescence detectors revisited," *Astroparticle Physics*, vol. 30, pp. 167–174, 2008.

[114] T. Gaisser and A. M. Hillas, "Reliability of the method of constant intensity cuts for reconstructing the average development of vertical showers," *Proceedings of the 15 th ICRC Plovdiv, Bulgaria*, vol. 80, p. 353, 1977.

[115] L. Landau and I. Pomeranchuk, "Limits of applicability of the theory of bremsstrahlung electrons and pair production at high-energies," *Doklady Akademii Nauk*, vol. 92, pp. 535–536, 1953.

[116] L. Landau and I. Pomeranchuk, "Electron cascade process at very high-energies," *Doklady Akademii Nauk*, vol. 92, pp. 735–738, 1953.

[117] A. B. Migdal, "Bremsstrahlung and pair production in condensed media at high-energies," *Physical Review*, vol. 103, pp. 1811–1820, 1956.

[118] A. S. Chou *et al. Proc.* 29^{th} *Intern. Cosmic Ray Conf.*, vol. 718, p. 319, 2005.

[119] Abraham *et al.*, "Upper limit on the cosmic-ray photon fraction at EeV energies from the Pierre Auger Observatory," *Astroparticle Physics*, vol. 31, no. 6, pp. 399–406, 2009.

[120] J. Conrad *et al.*, "Including systematic uncertainties in confidence interval construction for Poisson statistics," *Physical Review D*, vol. 67, p. 012002, Jan 2003.

[121] G. J. Feldman and R. D. Cousins, "Unified approach to the classical statistical analysis of small signals," *Physical Review D*, vol. 57, pp. 3873–3889, Apr 1998.

[122] M.-P. Veron-Cetty and P. Veron, "A catalogue of quasars and active nuclei: 12th edition," *Astronomy and Astrophysics*, vol. 455, pp. 773–777, 2006.

[123] T. P. A. Collaboration, "Correlation of the Highest-Energy Cosmic Rays with Nearby Extragalactic Objects," *Science*, vol. 318, no. 5852, pp. 938–943, 2007.

[124] P. Abreu, "Update on the correlation of the highest energy cosmic rays with nearby extragalactic matter," *Astroparticle Physics*, vol. 34, no. 5, pp. 314–326, 2010.

[125] D. Wittkowski and K. H. Kampert, "Anisotropy of ultra-high-energy cosmic rays," *Internal Auger GAP-note*, GAP-2013-038.

[126] A. Wald, "Sequential Tests of Statistical Hypotheses," *Annals of Mathematical Statistics*, vol. 16, pp. 117–186, 06 1945.

[127] D. O. Price, "Sequential Analysis," *Social Forces*, vol. 27, no. 2, pp. 170–171, 1948.

[128] T. H. Jarrett *et al.*, "2MASS Extended Source Catalog: Overview and Algorithms," *The Astronomical Journal*, vol. 119, no. 5, p. 2498, 2000.

[129] Tueller *et al.*, "The 22 Month Swift-BAT All-Sky Hard X-ray Survey," *The Astrophysical Journal Supplement Series*, vol. 186, no. 2, p. 378, 2010.

[130] P. Abreu *et al.*, "A search for anisotropy in the arrival directions of ultra high energy cosmic rays recorded at the Pierre Auger Observatory," *Journal of Cosmology and Astroparticle Physics*, vol. 1204, p. 040, 2012.

[131] P. Abreu *et al.*, "Search for signatures of magnetically-induced alignment in the arrival directions measured by the Pierre Auger Observatory," *Astroparticle Physics*, vol. 35, pp. 354–361, 2012.

[132] A. Aab *et al.*, "Search for patterns by combining cosmic-ray energy and arrival directions at the Pierre Auger Observatory," *The European Physical Journal C*, vol. 75, no. 6, 2015.

[133] P. Abreu *et al.*, "Constraints on the origin of cosmic rays above 10^{18} eV from large scale anisotropy searches in data of the Pierre Auger Observatory," *The Astrophysical Journal*, vol. 762, p. L13, 2012.

[134] A. Aab *et al.*, "Large Scale Distribution of Ultra High Energy Cosmic Rays Detected at the Pierre Auger Observatory with Zenith Angles up to 80°," *The Astrophysical Journal*, vol. 802, no. 2, p. 111, 2015.

[135] E. Armengaud, "CRPropa: A numerical tool for the propagation of UHE cosmic rays, gamma-rays and neutrinos," *Astroparticle Physics*, vol. 28, pp. 463–471, 2007.

[136] J. L. Puget, F. W. Stecker, and J. H. Bredekamp, "Photonuclear Interactions of Ultrahigh-Energy Cosmic Rays and their Astrophysical Consequences," *The Astrophysical Journal*, vol. 205, pp. 638–654, 1976.

[137] G. R. Blumenthal, "Energy loss of high-energy cosmic rays in pair-producing collisions with ambient photons," *Physical Review*, vol. D1, pp. 1596–1602, 1970.

[138] S. R. Kelner and F. A. Aharonian, "Energy spectra of gamma rays, electrons, and neutrinos produced at interactions of relativistic protons with low energy radiation," *Physical Review D*, vol. 78, p. 034013, Aug 2008.

[139] A. Mucke *et al.*, "SOPHIA: Monte Carlo simulations of photohadronic processes in astrophysics," *Computer Physics Communications*, vol. 124, pp. 290–314, 2000.

[140] A. J. Koning, S. Hilaire, and M. C. Duijvestijn, "TALYS-1.0," *Proceedings of the International Conference on Nuclear Data for Science and Technology*, pp. 211–214, 2008.

[141] N. Nierstenhoefer, *On the Origin and Propagation of Ultra-High Energy Cosmic Rays*. PhD thesis, 2011.

[142] S. Lee, "On the propagation of extragalactic high-energy cosmic and gamma-rays," *Physical Review*, vol. D58, p. 043004, 1998.

[143] E. Armengaud and T. Beau, "The CRPropa framework: A numerical tool to study propagation effects on UHECRs and their secondaries in the Local Universe," 2007.

[144] O. Buss *et al.*, "Transport-theoretical description of nuclear reactions," *Physics Reports*, vol. 512, no. 1–2, pp. 1–124, 2012. Transport-theoretical Description of Nuclear Reactions.

[145] B. Krusche, "Photoproduction of mesons of nuclei: The photonuclear programs at ELSA and MAMI," *Journal of Physics: Conference Series*, vol. 349, p. 012003, 2012.

[146] M. Anghinolfi *et al.*, "Behavior of the Be and C total photonuclear cross section in the nucleon resonance region," *Physical Review C*, vol. 47, pp. R922–R925, Mar 1993.

[147] N. Bianchi *et al.*, "Absolute total photoabsorption cross sections on nuclei in the nucleon resonance region," *Physics Letters B*, vol. 325, no. 3–4, pp. 333–336, 1994.

[148] M. MacCormick *et al.*, "Total photoabsorption cross-sections for H-1, H-2 and He-3 from 200-MeV to 800-MeV," *Physical Review*, vol. C53, pp. 41–49, 1996.

[149] J. Ahrens, "The Total Absorption of Photons by Nuclei," *Nuclear Physics*, vol. A446, pp. 229C–239C, 1985.

[150] N. Bianchi *et al.*, "Total hadronic photoabsorption cross-section on nuclei in the nucleon resonance region," *Physical Review*, vol. C54, pp. 1688–1699, 1996.

[151] G. L. Harris, M. Rejkuba, and W. E. Harris, "The Distance to NGC 5128 (Centaurus A)," *Publications of the Astronomical Society of Australia*, vol. 27, pp. 457–462, 2010.

[152] D. Hooper and A. M. Taylor, "On The Heavy Chemical Composition of the Ultra-High Energy Cosmic Rays," *Astroparticle Physics*, vol. 33, pp. 151–159, 2010.

[153] D. Boncioli *et al.*, "Combined spectrum-composition fit," *Internal Auger GAP-note*, GAP-2012-129.

[154] D. Boncioli, "Fitting the spectrum and composition data with SimProp," *Internal Auger GAP-note*, GAP-2014-11.

[155] D. Walz and M. Erdmann, "Constraining UHECR source scenario with spectrum and Xmax distribution," *Internal Auger GAP-note*, GAP-2014-034.

[156] S. Riggi, D. Allard, and M. Unger, "Combined spectrum-$X_{\max}$ fit with a likelihood approach," *Internal Auger GAP-note*, GAP-2011-101.

[157] M. DuVernois and M. R. Thayer, "The elemental composition of the galactic cosmic-ray source: Ulysses high-energy telescope results," *The Astrophysical Journal*, vol. 465, pp. 982–984, 1996.

[158] M. Erdmann *et al.*, "A Benchmark Scenario for UHECR Propagation," *Internal Auger GAP-note*, GAP-2012-138.

[159] F. James and M. Roos, "Minuit: A System for Function Minimization and Analysis of the Parameter Errors and Correlations," *Computer Physics Communications*, vol. 10, pp. 343–367, 1975.

[160] R. Brun and F. Rademakers, "ROOT: An object oriented data analysis framework," *Nuclear Instruments and Methods in Physics Research*, vol. A389, pp. 81–86, 1997.

[161] R. Fletcher, "A New Approach to Variable Metric Algorithms.," *The Computer Journal*, vol. 13, no. 3, pp. 317–322, 1970.

[162] T. Pierog *et al.*, "EPOS LHC : test of collective hadronization with LHC data," 2013.

[163] J. Abraham *et al.*, "The Cosmic Ray Energy Spectrum and Related Measurements with the Pierre Auger Observatory," 2009.

[164] J. Abraham *et al.*, "Measurement of the Depth of Maximum of Extensive Air Showers above 10^{18} eV," *Physical Review Letters*, vol. 104, p. 091101, 2010.

[165] A. M. Taylor, "UHECR Composition Models," *Astroparticle Physics*, vol. 54, pp. 48–53, 2014.

[166] D. Boncioli and A. di Matteo, "Effect of photodisintegration channel on propagation and fit," *Internal Auger GAP-note*, GAP-2015-017.

[167] D. Walz, "Impact of Photodisintegration Uncertainties on the Combined Fit," *Internal Talk*, 2015.

[168] S. Mollerach and E. Roulet, "Magnetic diffusion effects on the ultra-high energy cosmic ray spectrum and composition," *Journal of Cosmology and Astroparticle Physics*, vol. 1310, p. 013, 2013.

[169] D. d'Enterria *et al.*, "Constraints from the first LHC data on hadronic event generators for ultra-high energy cosmic-ray physics," *Astroparticle Physics*, vol. 35, pp. 98–113, 2011.

[170] S. Ostapchenko, "Air shower development: impact of the LHC data," *Proc. 32nd ICRC*, vol. 2, p. 71, 2011.

[171] T. Pierog and K. Werner, "Muon Production in Extended Air Shower Simulations," *Physical Review Letters*, vol. 101, p. 171101, 2008.

[172] E.-J. Ahn *et al.*, "Cosmic ray interaction event generator SIBYLL 2.1," *Physical Review D*, vol. 80, p. 094003, Nov 2009.

[173] S. Ostapchenko, "Nonlinear screening effects in high energy hadronic interactions," *Physical Review D*, vol. 74, p. 014026, Jul 2006.

[174] D. Wittkowski, *In Preparation.* PhD thesis.

[175] A. M. Taylor, M. Ahlers, and D. Hooper, "Indications of Negative Evolution for the Sources of the Highest Energy Cosmic Rays," 2015.

[176] M. Ajello *et al.*, "The Cosmic Evolution of Fermi BL Lacertae Objects," *The Astrophysical Journal*, vol. 780, no. 1, p. 73, 2014.

[177] R. J. Protheroe and P. L. Biermann, "A new estimate of the extragalactic radio background and implications for ultra-high-energy gamma ray propagation," *Astroparticle Physics*, vol. 6, pp. 45–54, 1996.

[178] J. Jackson, *Classical electrodynamics*. Wiley, 1975.

[179] J. Abraham *et al.*, "Upper limit on the cosmic-ray photon flux above 10^{19} eV using the surface detector of the Pierre Auger Observatory," *Astroparticle Physics*, vol. 29, pp. 243–256, 2008.

[180] K. Shinozaki *et al.*, "Upper Limit on Gamma-Ray Flux above 1019 eV Estimated by the Akeno Giant Air Shower Array Experiment," *The Astrophysical Journal Letters*, vol. 571, no. 2, p. L117, 2002.

[181] A. V. Glushkov *et al.*, "Constraints on the flux of primary cosmic-ray photons at energies $E > 10^{18}$ eV from Yakutsk muon data," *Physical Review D*, vol. 82, p. 041101, Aug 2010.

[182] T. Abu-Zayyad *et al.*, "Upper limit on the flux of photons with energies above 10^{19} eV using the Telescope Array surface detector," *Physical Review*, vol. D88, no. 11, p. 112005, 2013.

[183] G. Rubtsov *et al.*, "Upper limit on the ultrahigh-energy photon flux from agasa and yakutsk data," *Physical Review*, vol. D73, p. 063009, 2006.

[184] M. Risse *et al.*, "Upper Limit on the Photon Fraction in Highest-Energy Cosmic Rays from AGASA Data," *Physical Review Letters*, vol. 95, p. 171102, Oct 2005.

[185] M. Settimo, "Private comunication."

[186] G. Decerprit and D. Allard, "Constraints on the origin of ultrahigh energy cosmic rays from cosmogenic neutrinos and photons," *Astronomy and Astrophysics*, vol. 535, p. A66, 2011.

[187] G. B. Gelmini, O. E. Kalashev, and D. V. Semikoz, "GZK Photons Above 10-EeV," *Journal of Cosmology and Astroparticle Physics*, vol. 0711, p. 002, 2007.

[188] M. Takeda *et al.*, "Energy determination in the Akeno Giant Air Shower Array experiment," *Astroparticle Physics*, vol. 19, pp. 447–462, 2003.

[189] O. E. Kalashev, V. A. Kuzmin, and D. V. Semikoz 1999.

[190] A. Abdo *et al.*, "The Spectrum of the Isotropic Diffuse Gamma-Ray Emission Derived From First-Year Fermi Large Area Telescope Data," *Physical Review Letters*, vol. 104, p. 101101, 2010.

[191] W. Essey *et al.*, "Role of Line-of-sight Cosmic-ray Interactions in Forming the Spectra of Distant Blazars in TeV Gamma Rays and High-energy Neutrinos," *The Astrophysical Journal*, vol. 731, no. 1, p. 51, 2011.

[192] M. G. Aartsen *et al.*, "Observation of High-Energy Astrophysical Neutrinos in Three Years of IceCube Data," *Physical Review Letters*, vol. 113, p. 101101, Sep 2014.

[193] P. Abreu *et al.*, "Ultrahigh Energy Neutrinos at the Pierre Auger Observatory," *Advances in High Energy Physics*, vol. 2013, p. 708680, 2013.

[194] M. G. Aartsen *et al.*, "Probing the origin of cosmic rays with extremely high energy neutrinos using the IceCube Observatory," *Physical Review*, vol. D88, p. 112008, 2013.

[195] E. Roulet *et al.*, "PeV neutrinos from the propagation of ultra-high energy cosmic rays," *Journal of Cosmology and Astroparticle Physics*, vol. 1301, p. 028, 2013.

[196] F. W. Stecker, M. Malkan, and S. Scully, "Intergalactic photon spectra from the far ir to the uv lyman limit for $0 < Z < 6$ and the optical depth of the universe to high energy gamma-rays," *The Astrophysical Journal*, vol. 648, pp. 774–783, 2006.

[197] Abraham *et al.*, "Limit on the diffuse flux of ultrahigh energy tau neutrinos with the surface detector of the Pierre Auger Observatory," *Physical Review D*, vol. 79, p. 102001, May 2009.

[198] R. Abbasi *et al.*, "A Search for a Diffuse Flux of Astrophysical Muon Neutrinos with the IceCube 40-String Detector," *Physical Review*, vol. D84, p. 082001, 2011.

[199] H. Takami, S. Inoue, and T. Yamamoto, "Propagation of Ultra-High-Energy Cosmic Ray Nuclei in Cosmic Magnetic Fields and Implications for Anisotropy Measurements," *Astroparticle Physics*, vol. 35, pp. 767–780, 2012.

[200] P. Abreu *et al.*, "Bounds on the density of sources of ultra-high energy cosmic rays from the Pierre Auger Observatory," *Journal of Cosmology and Astroparticle Physics*, vol. 1305, no. 05, p. 009, 2013.

[201] P. Sommers, "Cosmic ray anisotropy analysis with a full-sky observatory," *Astroparticle Physics*, vol. 14, pp. 271–286, 2001.

[202] J. Abraham *et al.*, "Correlation of the highest-energy cosmic rays with the positions of nearby active galactic nuclei," *Astroparticle Physics*, vol. 29, pp. 188–204, 2008.

Acknowledgement

This work would not be possible without the help and advice of many people whom I debt great thanks.
My first gratitudes goes to Prof. Karl-Heinz Kampert for the opportunity to realize this thesis and for his helpful supervision. He always managed to find time to let me benefit from his profound and comprehensive knowledge in the field of astroparticle physics. He inspired and motivates me by his enthusiasm and the his pleasant way of leadership.

I want to thank the members of the Auger Cosmic Ray phenomenology task group in particular Prof. Günther Sigl, Prof. Silvia Mollerach and Prof. Sergio Petrera for many ideas, suggestions and discussion.

I am indebted to Dr. Julian Rautenberg and Dr. Tobias Winchen who never get tired answering my questions and for proof-reading this thesis. I appreciated to have Prof. Piotr Homola for proof-reading the part concerning photon and neutrino fluxes where I profited from his expertises. I am thankful to David Wittkowski for many helpful discussions and a fruitful co-working. I also want to point out the very kind and cooperative atmosphere in the Astroparticle Group at the University of Wuppertal and the Pierre Auger Collaboration. Thanks to all the colleagues in this groups for helping me with their experience and knowledge all along. I also want to thank Ingrid Schaarwächter for coordinating all administrative issues and being a permanent contact person.

Finally, I want to express my gratefulness to my parents, my relatives and close friends for their patience and support especially during stressful times.
I am deeply thankful to Kathrin without whom I barely could achieve this goal. Thank you for the love and the strong support all along.

Selbstständigkeitserklärung

Hiermit versichere ich, dass ich diese Arbeit nur unter Zuhilfenahme der angegebenen Quellen und Hilfsmittel selbstständig angefertigt habe.

Ort, Datum	Biswajit Sarkar